Searching for Beyond the Minimal Supersymmetric Standard Model at the Laboratory and in the Sky

Dissertation
zur
Erlangung des Doktorgrades (Dr. rer. nat.)
der
Mathematisch-Naturwissenschaftlichen Fakultät
der
Rheinischen Friedrich-Wilhelms-Universität Bonn

vorgelegt von
Ju Min, Kim
aus
Seoul

Bonn Mai, 2010

Angefertigt mit Genehmigung der Mathematisch-Naturwissenschaftlichen Fakultät der Rheinischen Friedrich-Wilhelms-Universität Bonn.

1. Gutachter: Prof. Dr. Manuel Drees
2. Gutachter: Priv. Doz. Dr. Stefan Förste
Tag der Promotion: 27.7.2010
Erscheinungsjahr: 2010

Abstract

We study the collider signals as well as Dark Matter candidates in supersymmetric models. We show that the collider signatures from a supersymmetric Grand Unification model based on the SO(10) gauge group can be distinguishable from those from the (constrained) minimal supersymmetric Standard Model, even though they share some common features. The $N = 2$ supersymmetry has the charateristically distinct phenomenology, due to the Dirac nature of gauginos, as well as the extra adjoint scalars. We compute the cold Dark Matter relic density including a class of one-loop corrections. Finally, we discuss the detectability of neutralino Dark Matter candidate of the SO(10) model by the direct and indirect Dark Matter search experiments.

First of all, I appreciate Manuel Drees for his patience during the whole period of my Ph. D. He indeed deserves to be called my 'Doktorvater'. I thank my collaborators; in particular, Peter Zerwas and Choi Seongyoul, from whom I learned so much while working together. I thank former and present group members of Manuel; among others, Mitsuru Kakizaki and Siba P. Das, for having never minded to answer my questions. I thank Andreas Wisskirchen, without whose help on the computer I might have needed a few more weeks until I finish. I thank Stefan Förste, Klaus Desch, and Uli Klein for being the committee members.

I am grateful to Tae-Won Ha for helping me so much to keep the mental health. I thank him also for having read this thesis carefully. Finally, very special thanks go to my parents for having constantly supported me.

Contents

1 Introduction

The Standard Model (SM) of particle physics, which is a renormalizable quantum field theory based on the gauge symmetry, has been highly successful in a sense that its predictions agree very well with the experimental data of, M_W, the τ lifetime, and the muon anomalous magnetic moment, to name but a few [5].

Nevertheless, there are reasons to expect that the Standard Model is not the final theory of Nature from the theoretical point of view: First, there is no room for gravity in Standard Model [1]. Also, the choice of the gauge groups and the particle representations are ad hoc. Finally, the Higgs sector, a crucial ingredient for the Standard Model to work, is not very well understood.

Let us discuss the final point a bit more in detail. The Higgs, introduced to break the Electroweak symmetry through the nonvanishing vacuum expectation value, as the Universe gets cooled down, is a fundamental scalar field, which receives quadratically divergent radiative corrections in the Quantum Field Theory. Since we need Higgs not heavier than a few hundred GeV for the perturbativity of the model, if we assume the Standard Model to be valid up to the Planck scale ($M_P \sim 10^{18}$GeV), we must cancel the bare and renormalized mass by fine tunning of $\mathcal{O}(10^{-30})$. This, often called "Gauge heirarchy problem", can be solved, if some New Physics appears at TeV scale, for the cut-off scale in the radiative corrections now is a (few) TeV instead of 10^{18}GeV.

On the other hand, perhaps more importantly, there are experimental evidences for the physics beyond the Standard Model: The neutrino oscialltion has been reported since the first discovery by SuperKamiokande [6], which can be explained by nonvanishing (albeit very tiny) neutrino masses. Also, the existence of non-baryonic cold Dark Matter (DM), which does not exist in the SM, is by now well established [7].

Amongst various candidates for the New Physics, supersymmetry (SUSY) is particularly interesting. First of all, it is a natural generalization of space-time symmetries of Quantum Field Theory. It has been shown that [8], under the basic assumptions of Field Theory, the most general continuous symmetry of the S-matrix is a direct product of the super-Poincaré group (supersymmetry, tanslations, rotations, boosts) and the internal symmetry group. Another important property is stability under the radiative corrections. One can show that there are no perturbative loop corrections to the superpotential, for instance, by using the fact that the superpotentials are holomorphic [9]. From the practical point of view, the standard concepts of Quantum Field Theory are valid in supersymmetry, together with its calculability, which is essential in doing physics.

The weakest point of supersymmetry is, however, that it must be broken to be the theory describing our world, where we have not yet observed any of the supersymmetric partners of the Standard Model particles. Even though there is not yet a model which convinced the community, the suggested models share a common feature of assuming a "hidden sector" whose dynamics breaks supersymmetry. The SUSY breaking is then transmitted to the observable sector by a messenger sector. Here we list two most studied supersymmetry breaking mediation mechanisms:

- *Gravity-mediated supersymmetry breaking* The effect of SUSY breaking is mediated by gravitational interactions. The models are based on the local supersymmetry, where the parameters are space-time dependent. The SUSY algebra shows that an invariance under local SUSY transformation implies an invariance under a local coordinate shift. Hence, the local supersymmetry is called supergravity (SUGRA). When SUSY is broken spontaneously in the hidden sector, the goldstino degrees of freedom are absorbed by the gravitino which obtains a mass, $m_{3/2}$. The energy scale in the SUSY breaking in the hidden sector can be written in terms of gravitino mass and the Planck scale (albeit model dependent), and the SUSY breaking masses and the couplings are generally set by $m_{3/2}$.
- *Gauge-mediated supersymmetry breaking* The effect of SUSY breaking is mediated by gauge interactions. SUSY is broken when a SM singlet superfield obtains the vacuum expectation value, and the (s)particles in the observable sector "feel" the SUSY breaking via their couplings to the messenger particles in loops. The sparticle masses are (loop-) suppressed by the messenger sector mass scale, while the gravitino mass, determined by the fundamental SUSY breaking, is suppressed by the Planck scale. Therefore, in this scenario, the gravitino may be the lightest supersymmetric particle (LSP).

Field	$SU(3)_C, SU(2)_L, U(1)_Y$
$L = \begin{pmatrix} \nu_{eL} \\ e_L \end{pmatrix}$	$(\mathbf{1},\ \mathbf{2},\ \text{-}1\ )$
$\bar{E}$	$(\mathbf{1},\ \mathbf{1},\ 2)$
$Q = \begin{pmatrix} u_L \\ d_L \end{pmatrix}$	$(\mathbf{3},\ \mathbf{2},\ \frac{1}{3}\ )$
$\bar{U}$	$(\bar{\mathbf{3}},\ \mathbf{1},\ \text{-}\frac{4}{3})$
$\bar{D}$	$(\bar{\mathbf{3}},\ \mathbf{1},\ \frac{2}{3})$
H_d	$(\mathbf{1},\ \bar{\mathbf{2}},\ \text{-}1)$
H_u	$(\mathbf{1},\ \mathbf{2},\ 1)$

Table 1: The matter and Higgs superfield content of the MSSM.

Minimal Supersymmetric Standard Model

Now let us turn to the model realizing the idea of supersymmetry. The simplest in this species is the Minimal Supersymmetric Standard Model (MSSM) [2, 3]. It is minimal, in a sense that,

- The gauge group is $SU(3)_C \times SU(2)_L \times U(1)_Y$.
- Only one fermionic generator ($N = 1$) for the supersymmetry transformation is assumed. This implies that the gauginos are, in general, Majorana fields, for they are Weyl spinors that belong to the vector supermultiplet.[1]
- The matter, gauge, and Higgs contents are inherited from the Standard Model, together with one additional Higgs, which is required to give masses to the up-type quarks as well as to cancel the gauge anomaly. The fields must be supersymmetrized, such that the matter/Higgs superfields (Table 1) include their scalar partners, and the gauge superfields their fermionic partners.
- R-parity conservation is assumed. This prevents the unwanted renormalizable interaction mediating proton decay. Furthermore, it has important phenomenological implications; only the pairwise productions of superparticles as well as the stability of the LSP.

In MSSM, the SUSY breaking mechanism is not specified; rather, it is parametrized, admitting our ignorance. It is done by writing down all possible SUSY breaking terms, only requiring that it must not receive quadratic divergences. This is called soft SUSY breaking:

$$\begin{aligned}
-\mathcal{L}_{soft} &= \big(\tilde{Q}_i^\dagger \mathbf{m^2_{Q_{ij}}} \tilde{Q}_j + \tilde{d}_{Ri}^\dagger \mathbf{m^2_{D_{ij}}} \tilde{d}_{Rj} + \tilde{u}_{Ri}^\dagger \mathbf{m^2_{U_{ij}}} \tilde{u}_{Rj} + \tilde{L}_i^\dagger \mathbf{m^2_{L_{ij}}} \tilde{L}_j + \tilde{e}_{Ri}^\dagger \mathbf{m^2_{E_{ij}}} \tilde{e}_{Rj} \\
&+ m^2_{H_u}|H_u|^2 + m^2_{H_d}|H_d|^2\big) \\
&+ \frac{1}{2}(M_1 \overline{\lambda}_0 P_L \lambda_0 + M_1^* \overline{\lambda}_0 P_R \lambda_0) + \frac{1}{2}(M_2 \overline{\lambda}^A P_L \lambda^A + M_2^* \overline{\lambda}_A P_R \lambda_A) \\
&+ \frac{1}{2}(M_3 \overline{\tilde{g}}^a P_L \tilde{g}^a + M_3^* \overline{\tilde{g}}^a P_R \tilde{g}^a) \\
&+ \big[(f_u A_u)_{ij} \epsilon_{AB} \tilde{Q}_i^A H_u^B \tilde{u}_{Rj}^\dagger + (f_d A_d)_{ij} \tilde{Q}_i^A H_d^B \tilde{d}_{Rj}^\dagger + (f_e A_e)_{ij} \tilde{L}_i^A H_d^B \tilde{e}_{Rj}^\dagger + h.c.\big] \\
&+ (B\mu H_u^A H_{dA} + h.c.), \qquad (1)
\end{aligned}$$

where i, j denotes the generation indices, A, B, SU(2) indices, respectively.

One interesting feature of the MSSM is that the Higgs sector is not arbitrary any longer. The spontaneous electroweak symmetry breaking (EWSB) occurs for the negative

---

[1] Charged winos in SU(2) sector, however, generate Dirac charginos in combination with the higgsinos through the electroweak symmetry breaking.

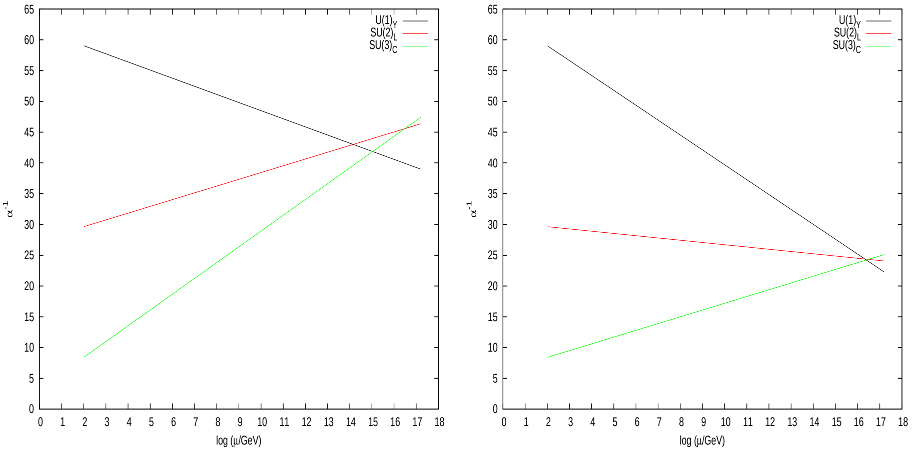

Figure 1: The running of inverse squared gauge coupling strengths in (a) SM, (b) MSSM.

eigenvalue in the Higgs mass matrix, which can be written in terms of soft breaking parameters and the Higgs(-ino) mass parameter in the superpotential at the tree-level.

Constrained Minimal Supersymmetric Standard Model

Even though it is "minimal", the MSSM has a huge number of free parameters, $\mathcal{O}(100)$. However, this is merely a consequence of parameterizing the SUSY breaking sector, meaning that once we understand it, the number of parameters will shrink sharply. In the meanwhile, we can make (well-motivated) assumptions on the soft breaking parameters to study the phenomenology. The models with these assumptions are called Constrained Minimal Supersymmetric Standard Model (CMSSM), and amongst them, the most-studied is the minimal supergravity (mSUGRA). It is summarized by the following universal conditions for the soft breaking terms in Eq. (1) at the Grand Unification scale (M_{GUT}) [2, 3]:

$$\begin{aligned} M_\alpha &= M_{1/2}, \quad \forall\alpha, \\ m_{ij}^2 &= m_0^2\delta_{ij}, \\ A_{ijk} &= A_0, \quad \forall i,j,k, \\ B_{ij} &= B_0, \quad \forall i,j, \end{aligned} \tag{2}$$

where α denotes the gauge group index and the i, j, the particle representations. The motivation comes from two directions. First, the gauge coupling unification at the high energy scale. In Fig. 1, we show the running of gauge couplings described by Renormalization Group Equations (RGEs) in the Standard Model and in the MSSM. Clearly, in the latter, they seem to "unify" at the scale, $M_{GUT} \sim 2 \times 10^{16}$GeV. On the other hand, one can show that the gaugino masses run in the same way as the squared gauge couplings do to the one loop order. This is because, in the language of the Feynmann diagrams, the one loop self energy diagrams for the gaugino masses can be obtained by supersymmetrizing the vacuum polarization diagrams for the gauge coupling strengths. To this end, it is reasonable to expect that the gaugino masses also meet at the M_{GUT}: The first of Eqs. (2). The rest of the Eqs. (2) come directly from assuming the gravity-mediated SUSY breaking mechanism, where all scalar fields obtain the same soft breaking masses at the tree level in the scalar potential derived from the supergravity Lagrangian.

As mentioned above, the EWSB is achieved by the interplay with the SUSY breaking. In mSUGRA, the $m^2_{H_u}$ becomes negative because of the large logarithmic loop corrections of the top Yukawa coupling from the GUT scale to the electroweak scale. Requiring that the M_Z receives the experimentally measured value determines the $|\mu|$ at the weak scale, as a function of the soft breaking parameters. Furthermore, using the consistency conditions for the Higgs potential to have a minimum, the parameters B_0 can be translated to the tanβ, the ratio between vacuum expectation values of the two Higgs fields in the MSSM. The mass spectra of sparticles in mSUGRA thus can be determined only with the following four continuous and one discrete parameters,

$$\text{sign}(\mu), \quad m_0, \quad M_{1/2}, \quad A_0, \quad \tan\beta. \tag{3}$$

The SUSY breaking (together with the EWSB) causes the mixing between gauginos and the higgsinos, such that they form charginos and neutralinos.

On the other hand, for the universal m_0, the (running) masses of sleptons and squarks at the weak scale differ due to the radiative corrections.[2] Since their masses obtain positive corrections from the gaugino loop contribution, in the large regions of parameter space, the lightest neutralino is often the LSP, which can be a good candidate for the DM.

Beyond the MSSM

The MSSM, or mSUGRA, which is the minimal constrained MSSM, is a simple framework wherein supersymmetry is realized. However, we are still left with the problems of the Standard Model we have addressed at the beginning: Absense of gravity and arbitrary choice of gauge group.

In fact, gravity plays a crucial role in mSUGRA (as its name implies), but how it works is still very different from the other interactions do. In order to achieve the true unification, we need to appeal to the Physics at the Planck scale (which is yet poorly understood), where the extended supersymmetry with $N > 1$ seems to be commonplace.

Phenomenologically, the $N = 2$ supersymmetry is interesting in several aspects: First, if we assume the D-term (of a hidden sector U(1)) SUSY breaking, then the radiative corrections to the SUSY breaking parameters are finite [10]. (Recall that they are logarithmically divergent in the MSSM, "softbreaking".) Second, the gauge supermultiplets

---

[2] The D-term contributions must be also included, but they are mostly subdominent.

are extended to the gauge hypermultiplet including a gaugino which, together with the original Majorana gaugino field, can form a Dirac field. Finally, there are several new fields which provides a rich phenomenology at the colliders, as we will see.

On the other hand, in the Grand Unified Theories (GUT) based on the SO(10) gauge group [32], all known matter fields, together with the right-handed neutrino which is needed to give neutrinos a mass (within R-parity conservation), reside in the **16** dimensional irreducible spinor representation. Furthermore, SO(10) contains the "Pati-Salam"[11] group $SU(4)_C \times SU(2)_L \times SU(2)_R$ as a subgroup, meaning that the parity is preserved at high energy and broken spontaneously.

How to Test the Models

Among others, we will focus on collider signals as well as informations on the Dark Matter to test the models.

Since the sparticles are expected to be not heavier than a few TeV, there is a good chance that we can test various supersymmetric models by examining their production and decay processes at the LHC, once it operates with its full center of mass energy.

The existence of Dark Matter is well established by direct and indirect astronomical observations. The recently released, best evidence comes from the studies of bullet cluster [12]: When the cluster collided with another cluster, the dissipationless stellar component, measured by gravitational lensing maps, passed through, while the plasma, measured from its X-ray emission, was decelerated.

Within a minimal ΛCDM model, and combining data on the cosmic microwave background (CMB) anisotropies with observations of supernovae of type 1a and with analyses of baryon acoustic oscillations, one finds [13]:

$$\Omega_{\rm CDM} h^2 = 0.1131 \pm 0.0034\,. \tag{4}$$

Here $\Omega_{\rm CDM}$ is the energy density of cold Dark Matter in units of the critical density, and h is the scaled Hubble parameter such that $H_0 = 100\, h\, \mathrm{km\, sec^{-1}\, Mpc^{-1}}$ where H_0 is the current Hubble parameter. This is the tightest constraint we currently have for the New Physics. Moreover, quite soon data from the Planck satellite are expected to reduce the error on $\Omega_{\rm CDM} h^2$ to the level of 1.5% using CMB measurements alone [15].

From the particle physics point of view, Weakly Interacting Massive Particles (WIMPs) are among the most attractive Dark Matter candidates. In standard cosmology their thermal relic density is naturally of the right order of magnitude. Owing to their weak interactions, they can be probed through both direct and indirect detection experiments [16]. Stating it in another way, the negative events in these experiments can also set constraints for the particle physics model which provides the WIMP, as we will see.

1.1 Outline

In chapter 2, we study the collider signals from supersymmetric models. In Sec. 2.1, we summarize the existing accelerator constraints that all New Physics candidates should satisfy. Then we begin with reviewing the phenomenology of the MSSM. We will explain the production and decay channels of the sparticles in generic, and show how they actually manifest at the LHC by choosing two (representing) parameter sets in mSUGRA. In Sec. 2.3, we will briefly discuss the general phenomenological aspects of supersymmetric grand unified theories, which is followed by a detailed study on an SO(10) model with two step intermediate symmetry breaking. In particular, we compare its signatures at the LHC with those of mSUGRA. In the last section, we will study the $N = 2$ supersymmetry at some length.

In chapter 3, we turn our attention to Dark Matter. Sec. 3.1 is devoted to the relic density calculation. We firstly review the standard computation, and then show a simple way to include a certain class of one-loop corrections, with technical details and applications. In Sec. 3.2, we will focus on the direct and indirect Dark Matter search experiments. First, we will briefly explain the underlying theory. Then we will discuss the detectability of Dark Matter candidates in the mSUGRA and in the SO(10) model we studied in Sec. 2.3.

Finally, in chapter 4, we will summarize and conclude.

1.2 Publication

Parts of this thesis have been published (or submitted for the publication) in scientific journals:

- *Color-Octet Scalars of N=2 Supersymmetry at the LHC*,
  S. Y. Choi, M. Drees, J. Kalinowski, J. M. Kim, E. Popenda and P. M. Zerwas,
  Phys. Lett. B672:246-252, 2009, arXiv:0812.3586

- *Potentially Large One-loop Corrections to WIMP Annihilation*,
  M. Drees, J. M. Kim and K. I. Nagao, Phys. Rev. D 81, 105004, 2010, arXiv:0911.3795

- *Dirac Neutralinos and Electroweak Scalar Bosons of N=1/N=2 Hybrid Supersymmetry at Colliders*,
  S. Y. Choi, D. Choudhury, A. Freitas, J. Kalinowski, J. M. Kim, and P. M. Zerwas,
  arXiv:1005.0818

Parts of this thesis are in preparation for the publication:

- *Direct and Indirect Detection of Neutralino Dark Matter and Collider Signatures in an SO(10) Model with Two Intermediate Scales*,

M. Drees, J. M. Kim, and E. -K. Park,
In preparation

2 Collider Signals from Supersymmetric Models

2.1 Current Accelerator Constraints

2.1.1 Electroweak precision experiments

1. Electroweak symmetry breaking and tachyons

As mentioned earlier, the condition for the EWSB is written in terms of soft breaking and superpotential mass parameters at the weak scale. Technically, one solves equations that allow to express μ^2 and the bilinear Higgs soft mass parameter $B\mu$ in terms of M_Z and the $\tan\beta$. However, these equations sometimes formally lead to $\mu^2 < 0$, which indicates that EWSB is not possible for the given set of input parameters.

2. Branching ratio of $b \to s\gamma$

In the SM, flavor changing neutral currents (FCNC) are absent at tree level. Thus, the radiative $B \to X_s\gamma$ decay is mediated by loops containing up–type quarks and W bosons. As well known [21], SUSY loop contributions can be comparable to those from the SM. Therefore, the measurement of the branching ratio for this decay, performed by CLEO, Belle and BaBar [22],

$$B(b \to s\gamma) = (352 \pm 23 \pm 9) \times 10^{-6} \tag{5}$$

can be used to constrain the parameter space of our model. The first error in (5) includes statistical, systematic, extrapolation and $b \to d\gamma$ contamination errors, while the second one is estimated to be the difference of the average after varying the central value of each experimental result by $\pm 1\sigma$. To be conservative, we take the linear sum of the errors in Fig. 6, since the calculation strongly depends on the assumptions of the boundary conditions. Even minor deviations from strict universality, for example due to the running between M_X and M_{Pl} [23, 24], can have very large effects [25] .

3. The anomalous magnetic moment of the muon

The anomalous magnetic moment of the muon is one of the most precisely calculated and measured quantities. There is an about 3σ discrepancy between the SM prediction based on data from e^+e^- annihilation into hadrons and the experimental value. While this is still somewhat controversial – an SM prediction which instead makes use of τ decay data plus some assumptions is in fair agreement with the data – we here constrain the parameter space of models that allows to explain this discrepancy.

The world average, dominated by data from the E821 collaboration at BNL, is [5]

$$a_\mu^{exp} = \frac{g_\mu - 2}{2} = (11659208.0(5.4)(3.3)) \times 10^{-10}\,. \tag{6}$$

The theoretical value [26] is calculated as the sum of (i) pure QED contributions including the diagrams of virtual photon, vacuum polarization (VP) from e, μ and τ, and leptonic light–by–light scattering, (ii) hadronic contributions including VP from quarks, most reliably estimated using $e^+e^- \to$ hadrons data, and hadronic light–by–light scattering, and (iii) electroweak contributions. The resulting SM prediction is [5]

$$a_\mu^{theory} = (116591788(2)(46)(35)) \times 10^{-11} . \tag{7}$$

Demanding that supersymmetric loops, involving smuons and neutralinos or smuon neutrinos and charginos, lead to agreement between theory and experiment at the 2σ level thus implies

$$5.2 \times 10^{-10} < \delta a_{\mu,\mathrm{SUSY}} < 34.6 \times 10^{-10} . \tag{8}$$

2.1.2 Constraints from direct searches

The most important constraints are those on the masses of the lightest Higgs boson and the lightest chargino. In combination, they imply that constraints on the masses of strongly interacting sparticles [5] are automatically satisfied.

We interpret the limit $M_{H_{\mathrm{SM}}} > 114.4$ GeV, which comes from searches for $e^+e^- \to ZH^0$, as imposing a lower mass on the mass of the lighter CP–even Higgs boson of the MSSM,

$$M_h > 111 \text{ GeV} , \tag{9}$$

where we allowed for a ~ 3 GeV theoretical uncertainty [27] in the calculation of m_h. We also require

$$m_{\tilde{\chi}_1^\pm} > 104 \text{ GeV} , \tag{10}$$

since scenarios allowing chargino masses significantly below the highest LEP beam energy cannot be realized in our scenario: These scenarios all require the presence of sneutrinos with mass near or slightly below that of the chargino, and scenarios where both the sneutrino and $\tilde{\chi}_1^\pm$ have mass below the limit (10) violate the Higgs constraint (9).

2.2 Minimal Supergravity

2.2.1 Production and decays of the Supersymmetric particles

We review the production and decays of the supersymmetric particles. The discussions in this subsection are based on [2, 3]. Although the discussion is on general ground, i.e. not assuming any specific model, the examples are more focused on the mSUGRA scenario.

1. Sparticle production at lepton collider

Even though the superparticles have not been discovered at LEP 2 e^+e^- collider ($\sqrt{s} \simeq$

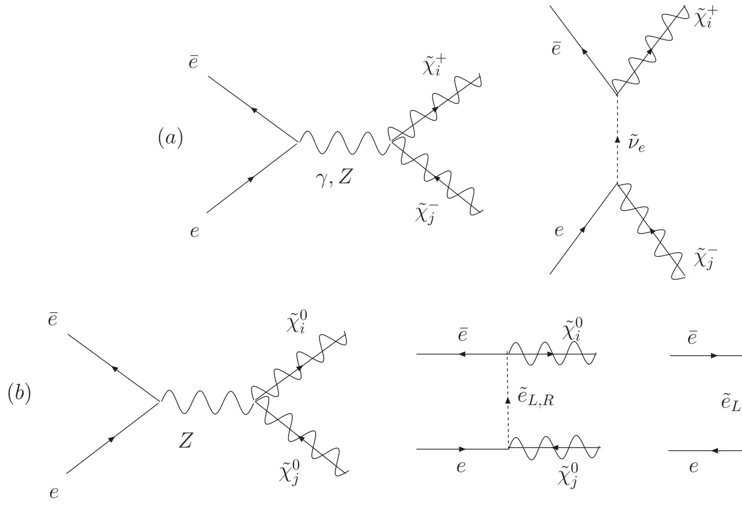

Figure 2: Tree-level diagram for the (a) $e^+e^- \to \tilde{\chi}_i^+\tilde{\chi}_j^-$, (b) $e^+e^- \to \tilde{\chi}_i^0\tilde{\chi}_j^0$.

209GeV), it has set the most stringent constraints (together with Tevatron) so far. Furthermore, another e^+e^- collider called International Linear Collider (ILC) with the $\sqrt{s} \sim (0.5 - 1)$TeV is under the serious planning. The lepton colliders have the following advantages compared to the hadron collider:

- All the center of mass energy can, in principle, be used for the new particle production.[3]
- Detailed kinematic reconstruction of events is possible.
- The background is well-understood and calculable.
- The polarized beam is available.

Therefore, precision studies are in general possible.

Charginos and neutralinos

Charginos (neutralinos) are pairwisely produced via s-channel γ, Z boson (Z boson) exchange and t-channel (t-, u-) sneutrinos (sleptons) exchange. See Fig. 2. If the $|\mu| \gg M_{1,2}$, then $\tilde{\chi}_{1,2}^0$, $\tilde{\chi}_1^+$ are gaugino-like. For the wino-like $\tilde{\chi}_1^+$, the cross section can be large because of the enhanced isotriplet coupling to the Z boson, but it depends on the sneutrino mass, due to the interference between the s- and the t-channel. For the bino (neutral wino)-like $\tilde{\chi}_{1(2)}^0$, the $Z\tilde{\chi}_{1(2)}^0\tilde{\chi}_{1(2)}^0$ coupling is suppressed, yet the $e\tilde{e}_{L,R}\tilde{\chi}_1^0$ coupling is the gauge coupling with the large hypercharge for the $\tilde{e}_R$. If $|\mu| \ll M_{1,2}$, the $\tilde{\chi}_1^{0,+}$ is higgsino-like,

---

[3] Complications arise due to the bremsstrahlung, and the beamstrahlung (The real photons emitted by the $e^\pm$ interact cause energy loss).

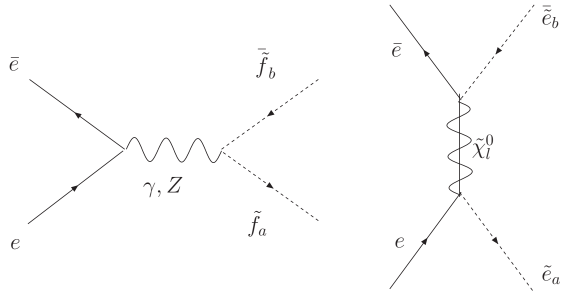

Figure 3: Tree-level diagram for the slepton pair production.

and the couplings to the sneutrino and slepton become negligible. The production cross section, in this case, for the $\tilde{\chi}_1^+\tilde{\chi}_1^-$ and $\tilde{\chi}_1^0\tilde{\chi}_2^0$ are comparable, yet $\tilde{\chi}_1^0\tilde{\chi}_1^0$ and $\tilde{\chi}_2^0\tilde{\chi}_2^0$ are very small due to the cancellations between two contributions in the coupling.

Sleptons

The Feynmann diagrams are shown in Fig. 3. Note that the t-channel neutralino exchange takes place only for the selectron final states, with two features: First, since the electron Yukawa coupling is negligible, only the gaugino component contributes. Second, this is the S-wave amplitude possible for the slepton pair production, meaning that this channel is much less suppressed near the threshold.[4] At a $\sqrt{s} = 500\text{GeV}$ e^+e^- collider, the typical size of a stau or smuon pair production cross section (away from the threshold) is $\sim 50\text{fb}$, and that of selectron is about an order of magnitude larger, depending on the neutralino mixing and the masses.

2. Sparticle production at hadron collider

The biggest physical advantage of hadron colliders is the high beam energy. Currently there are two working machines: 1) Fermilab Tevatron $p\bar{p}$ collider at $\sqrt{s} \simeq 2\text{TeV}$, and 2) CERN LHC pp collider at $\sqrt{s}$ up to $\simeq 14\text{TeV}$.

The sparticle production occurs via presumably hard scattering between quarks, antiquarks, and gluons. Therefore, we can use the perturbative QCD within the framework of parton model to compute the cross section. The hadronic cross section is obtained through convolution with the parton distribution function (PDF), $f_{i|p}(x_1, Q^0)$:

$$d\sigma(p(k)^{(}\bar{p}^{)}(k') \to XY) = \int_{x_1,min}^{1} dx_1 \int_{x_2,min}^{1} dx_2 f_{i|p}(x_1, Q^2) f_{j|^{(}\bar{p}^{)}}(x_2, Q^2) d\hat{\sigma}(ij \to X), \quad (11)$$

where $\hat{\sigma}$ describes the subprocess, and Y represents the beam remnants and the initial state radiation (ISR). The total energy of the parton subsystem is not known exactly,

---

[4] Recall that the P(S)–wave has the β^3 (β) dependence, with $\beta = \sqrt{1 - \frac{2m_{\tilde{e}}^2}{s}}$.

but the total transverse momentum is zero for the initial system. Therefore, the presence of the neutral and stable object will be signalled by an imbalance in the transeverse momentum (energy), called 'missing transverse energy' ($\not{E}_T$). Even though the neutrinos also contribute to the $\not{E}_T$, the amount of $\not{E}_T$ in supersymmetric processes in general is significantly greater, and applying the lower cut on $\not{E}_T$ can increase the ratio of signal to the background.

Charginos and neutralinos

The Feynmann diagrams for the chargino and the neutralino pair production is the same as Fig. 2, with $e^+e^- \to q\bar{q}$, and $\tilde{l} \to \tilde{q}$. If the $|M_3| \simeq 3.5|M_2|$ as in mSUGRA, the first two generation squarks are significantly heavier than the light charginos and neutralinos. For the gaugino-like charginos, the s-channel photon and the Z boson exchange contributions dominate, while for the gaugino-like neutralinos the couplings to the Z boson are suppressed, as pointed out previously. The higgsino-like neutralinos would be pair-produced, in particular as $\tilde{\chi}_1^0\tilde{\chi}_2^0$, with comparable rates as charginos.

A novel subprocess at the hadron collider is, $q\bar{q}', q'\bar{q} \to \tilde{\chi}_l^0\tilde{\chi}_k^\pm$ ($q = d, s$; $q' = u, c$; $l = 1, ..., 4$; $k = 1, 2$), via s-channel W boson exchange as well as via t-, u-channel squark exchange. This is the most prominent of all sparticle production processes at the Tevatron, assuming the gaugino mass unification condition [2]. If $|\mu| \gg |M_{1,2}|$, the wino-like $\tilde{\chi}_2^0$ and $\tilde{\chi}_1^\pm$ have large gauge coupling to the W boson, while the coupling of bino-like $\tilde{\chi}_1^0$ to the W boson is suppressed by the electroweak symmetry. When $|\mu| \ll |M_{1,2}|$, the $\tilde{\chi}_1^+\tilde{\chi}_1^-$, $\tilde{\chi}_{1,2}^0\tilde{\chi}_1^\pm$, and $\tilde{\chi}_1^0\tilde{\chi}_2^0$ are pair-produced through smaller isodoublet gauge couplings to the W boson, compared to the isotriplet one for the wino-like states.

Sleptons

The charged sleptons may be produced in pairs via s-channel γ, Z boson exchange. (Corresponding to the first diagram in Fig. 3, with $e \to q$.) In addition, the $q\bar{q}' \to W^* \to \tilde{l}_L\bar{\tilde{\nu}}_l$ may take place. Note that the channel to the $\tilde{l}_R\bar{\tilde{\nu}}_l$ is forbidden, for the W boson couples only to the left-handed sleptons and their superpartners.

Squarks and gluinos

Although gluinos and (the first and second generation) squarks are expected to be the heaviest among the sparticles, their production rate at the hadron colliders may be much larger than those of sleptons and neutralinos due to the strong interaction.

For the gluino pair production from the quark pair, we can take Fig. 2, with $e \to q$, Z→g, $\tilde{e} \to \tilde{q}$. In Fig. 4, we list the relevant Feynmann diagrams for the gluino pair production from the gluon pair. For the squark pair production, there are three classes of subprocesses: $q_i\bar{q}_j \to \tilde{q}_i\bar{\tilde{q}}_j$, $q_i\bar{q}_i \to \tilde{q}_j\bar{\tilde{q}}_j$; $q_iq_j \to \tilde{q}_i\tilde{q}_j$, and $gg \to \tilde{q}_i\bar{\tilde{q}}_i$. ($i, j$ are flavor indices.)

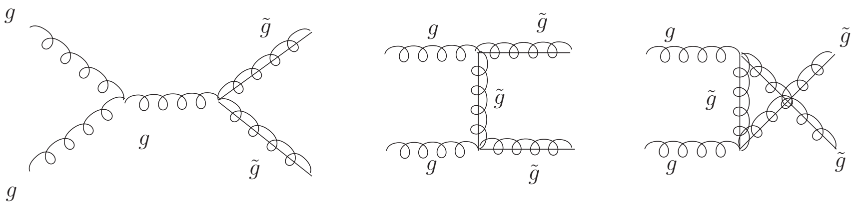

Figure 4: Tree-level diagram for the gluino production.

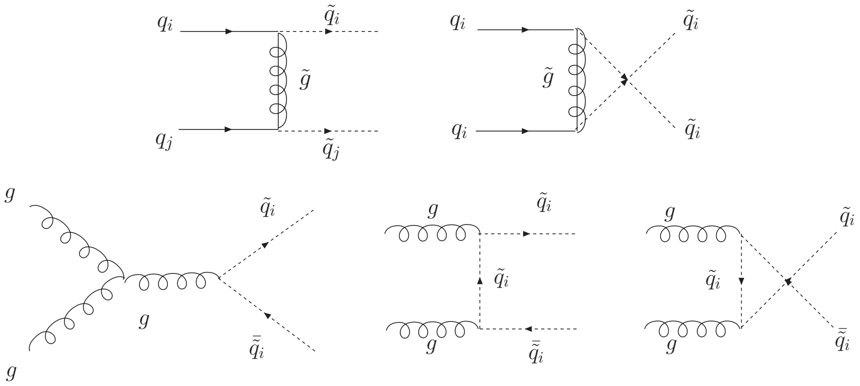

Figure 5: Tree-level diagram for the squark production.

For first two processes, we can take the Fig. 3 with $e \to q$, $\gamma, Z \to g$, $\tilde{\chi} \to \tilde{g}$, and $\tilde{f} \to \tilde{q}$. We list the diagrams for the other two ones in Fig. 5.

Since the gluon PDF dominates for the small partonic center of mass energy, the gluino production from the gg initial state is dominant for the lower $m_{\tilde{g}}$ ($\lesssim$ 1TeV) and the large beam center of mass energy (e.g. LHC), while (valence) $q\bar{q}$ dominates for the large $m_{\tilde{g}}$ at the Tevatron.

3. Sparticle decays

The produced sparticles would decay into other sparticles and SM particles, until they decayed down to the LSP.

Gluinos and squarks

Let us first consider the first two generation squarks, assuming that they have the common mass, $m_{\tilde{q}}$. In mSUGRA, their mass differences are indeed very small due to the negligible Yukawa contribution and the common strong gauge interaction contribution. In the following, $q = d, s$; $q' = u, c$, $l = 1, ..., 4$; $k = 1, 2$, and the charge-conjugated processes should be added.

1) $m_{\tilde{q}} < m_{\tilde{g}}$

- $\tilde{g} \to \bar{q}\tilde{q}_{L,R}$.
- $\tilde{q}_{L,R} \to q\tilde{\chi}^0_l$; $\tilde{q}_L \to q'\tilde{\chi}^\pm_k$.
    - The $\tilde{q}_R$ with large hypercharge decays preferably to the bino-like gaugino ($\tilde{\chi}^0_1$ in most of mSUGRA parameter space).
    - The $\tilde{q}_L$ with larger $SU(2)_L$ gauge coupling decays preferably to a charged or neutral gaugino.
- $\tilde{q} \to q\bar{b}\tilde{b}_1$, $qb\bar{\tilde{b}}_1$, if $m_{\tilde{q}} > (m_b + m_{\tilde{b}_1})$.
    - Gluino-mediated, large if $\tilde{\chi}^0_{1,2}$ and $\tilde{\chi}^+_1$ are higgsino-like.

2) $m_{\tilde{g}} < m_{\tilde{q}}$

- $\tilde{q}_{L,R} \to q\tilde{g}$.
- $\tilde{q}_{L,R} \to q\tilde{\chi}^0_l$; $\tilde{q}_L \to q'\tilde{\chi}^\pm_k$.
    - Subdominant contribution, $\tilde{q}_L$ to the charged or neutral $SU(2)_L$ gauginos.
- $\tilde{g} \to q\bar{q}\tilde{\chi}^0_l$, $q\bar{q}'\tilde{\chi}^\pm_k$;
- $\tilde{g} \to \bar{t}\tilde{t}_1$, if $m_{\tilde{g}} > (m_t + m_{\tilde{t}_1})$; $\bar{b}\tilde{b}_1$, if $m_{\tilde{g}} > (m_b + m_{\tilde{b}_1})$
    - Since the gluino has only strong interaction, the three-body decays are mediated by squarks.
- $\tilde{g} \to g\tilde{\chi}^0_l$.
    - Via q-q-$\tilde{q}$ or q-$\tilde{q}$-$\tilde{q}$ triangle loop diagrams. Significant if LSP is higgsino-like, or if $m_{\tilde{g}} \ll m_{\tilde{q}}$.

For the third generation squarks, firstly, due to the large m_t one needs to include the top mass in the final states when considering the kinematics, while we may neglect the other quark masses. Secondly, both the light and heavy stop/sbottoms can decay to charginos and W bosons, since they are mixture of left- and right-squarks:

$$\begin{aligned}\tilde{t}_{1,2} &\to t\chi^0_l, \quad b\chi^+_k, \\ \tilde{b}_{1,2} &\to b\chi^0_l, \quad t\chi^-_k.\end{aligned}$$

Thirdly, the large expected mass splitting between the stop and sbottom mass eigenstates enables the stop/sbottom final states for the stop/sbottom decay. Furthermore, because of the large stop (and sbottom, for large tanβ) Yukawa couplings, the decays involving Higgs final states are possible:

$$\begin{array}{rcl} \tilde{b}_{1,2} & \to & \tilde{t}_{1,2}W^-, \quad \tilde{t}_{1,2}H^-, \\ \tilde{b}_2 & \to & \tilde{b}_1 Z, \quad \tilde{b}_1 h, \quad \tilde{b}_1 H, \quad \tilde{b}_1 A, \\ \tilde{t}_{1,2} & \to & \tilde{b}_{1,2}W^+, \quad \tilde{b}_{1,2}H^+, \\ \tilde{t}_2 & \to & \tilde{t}_1 Z, \quad \tilde{t}_1 h, \quad \tilde{t}_1 H, \quad \tilde{t}_1 A. \end{array}$$

If all two body decays of $\tilde{t}_1$ are forbidden at the tree-level, the loop-induced decay,

$$\tilde{t}_1 \to c\tilde{\chi}^0_1, \tag{12}$$

the three-body decays,

$$\tilde{t}_1 \to b\nu_l\bar{\tilde{l}}, \quad b\tilde{\nu}_l\bar{l}, \quad b\tilde{\chi}^0_l W^+, \quad b\tilde{\chi}^0_l H^+, \tag{13}$$

or the four-body decays,

$$\tilde{t}_1 \to b\tilde{\chi}^0_1 f\bar{f}', \tag{14}$$

take place. ($f, \bar{f}'$ are SM fermions.) The Eq. (12) occurs via mixing between $\tilde{t}$ and $\tilde{c}$ flavor eigenstates. Although the tree-level flavor-violating interactions are absent in the Lagrangian at high energy scales, radiative corrections can induce them at the weak scale. In mSUGRA, the first two of Eq. (13) are favored (especially at low m_0) due to the light sleptons. If the $\tilde{t}_1$ is so light that even the three-body decays are kinematically forbidden, then Eq. (14) can occur.

Sleptons

The decay modes for the first two generation sleptons are:

$$\begin{array}{rcl} \tilde{l}_{L,R} & \to & l\tilde{\chi}^0_l; \quad \tilde{l}_L \to \nu_l\tilde{\chi}^\pm_k, \\ \tilde{\nu}_l & \to & \nu_l\tilde{\chi}^0_l, l\tilde{\chi}^\pm_k. \end{array}$$

The $\tilde{l}_R$ can decay only to neutralinos via $U(1)_Y$ interaction, while the $\tilde{l}_L$ decays preferably to both of the charginos and neutralinos via larger SU(2) gauge coupling.

The decay modes of third generation sleptons are similar to that of third generation squarks, due to the mixing effect and the Yukawa coupling (especially for the large tanβ), i.e. including the Higgs and Z boson final states.

In gauge mediated supersymmetry breaking models where $\tilde{\tau}_1$ is the Next Lightest Supersymmetric Particle (NLSP), $\tilde{\tau}_1$ decays to the $\tau\tilde{G}$, where $\tilde{G}$ is the gravitino. Here, the $\tilde{\chi}^0_1$ may be heavier than some of the sleptons, then the following decay mode of first two generation $\tilde{l}_R$ dominates:

$$\tilde{l}_R \to \tilde{\tau}^-_1\tau^+ l, \quad \tilde{\tau}^+_1\tau^- l. \tag{15}$$

In mSUGRA, there is co-annihilation region in the parameter space which is important on the cosmological ground. The $\tilde{\tau}_1$ is almost degenerate with the LSP, $\tilde{\chi}_1^0$, and the co–annihilation of the NLSP $\tilde{\tau}_1$ and the $\tilde{\chi}_1^0$ may effectively take place in the early Universe. Hence the neutralino Dark Matter relic density is consistent with the WMAP observation.

Neutralinos and charginos

The charginos and neutralinos decay dominantly via tree-level two-body channels, as long as allowed kinematically:

$$\begin{aligned}
\tilde{\chi}_k^+ &\rightarrow l_i^+\tilde{\nu}_j, \quad \nu_j\tilde{l}_i, \quad \bar{d}_i\tilde{u}_j, \quad u_i\bar{\tilde{\bar{d}}}_j, \\
\tilde{\chi}_k^+ &\rightarrow W^+\tilde{\chi}_l^0, \quad H^+\tilde{\chi}_l^0, \\
\tilde{\chi}_2^+ &\rightarrow Z\tilde{\chi}_1^+, \quad h\tilde{\chi}_1^+, \quad H\tilde{\chi}_1^+, \quad A\tilde{\chi}_1^+. \qquad (16)
\end{aligned}$$

$$\begin{aligned}
\chi_l^0 &\rightarrow \tilde{\nu}_i\bar{\nu}_j, \quad l_i\tilde{l}_j, \quad \bar{u}_i\tilde{u}_j, \quad \bar{d}_i\tilde{d}_j, \\
\tilde{\chi}_l^0 &\rightarrow W^+\tilde{\chi}_k^-, \quad H^+\tilde{\chi}_k^-, \\
\tilde{\chi}_l^0 &\rightarrow Z\tilde{\chi}_n^0, \quad h\tilde{\chi}_n^0, \quad H\tilde{\chi}_n^0, \quad A\tilde{\chi}_n^0. \qquad (17)
\end{aligned}$$

The wino-like gauginos decay to the $SU(2)_L$ doublet sfermions with the full gauge strength. As noted previously, since the neutralinos couple to the Z boson only via the higgsino, the decays of neutralinos involving Z boson final states can occur only when neutralinos in the process include large higgsino components. This is also true for the three-body decay of neutralino to another neutralino and a fermion pair via virtual Z boson exchange. On the other hand, the wino-like as well as the higgsino-like charginos have large gauge coupling to the W boson, and the corresponding decay channels can be dominant. The coupling of Higgs boson to the neutralinos and charginos originate from the product of Higgs chiral superfild, its hermitian conjugate and a vector superfield with gauge strength coupling. Therefore, decays with Higgs bosons in the final state will have large coupling only when one of the chargino/neutralinos in the decay channel is higgsino-like and the other is gaugino-like.

2.2.2 Signatures at the LHC: Benchmark points

In this subsection we focus on the collider signals from the mSUGRA. In mSUGRA, the LSP can be the lighter stop, lighter stau, or the lightest neutralino, depending on the parameters. In order for the stable LSP to be the Dark Matter candidate, however, it has to be electrically neutral. Hence, it is often taken as a part of mSUGRA that the lightest neutralino be the LSP.

1. Identification of the SUSY events

In a large part of parameter space, the gluino and the squarks are expected to be dominant among the SUSY production modes. Their cascade decay signatures will be in general very complicated, and the identification of SUSY events depends on the final states. Nevertheless, there are general features we might exploit:

- Missing transverse energy ($\not{E}_T$): At the end of each sparticle decay chain, there must be an LSP in the R-parity conserving SUSY. Being unobservable, the LSP leaves its footprint as the (large) $\not{E}_T$.

- Multiple jets: If the gluino and/or the squark decays into some other (s)particle and a quark, generally a high p_T jet is produced from the latter, which can be distinguished from the softer QCD jets.

- Transverse sphericity (S_T): The transverse sphericity is defined as

  $$S_T = \frac{2\lambda_2}{(\lambda_1 + \lambda_2)} ,$$

  where λ_1 and λ_2 are the eigenvaluesof the 2×2 sphericity tensor, $S_{ij} = \sum_k p_{ki} p^{kj}$ [29], where the k runs over the particles. For the SUSY events S_T tends to be larger, for the heavier sparticles are rather at rest compared to the lighter Standard model particles. QCD events are dominated by back-to-back process ($S_T \ll 1$).

- Effective mass (M_{eff}): The effective mass is defined to estimate the mass scale associated with the SUSY production [28]

  $$M_{eff} = \sum_{i=1}^{4} p_T^{jet,i} + \sum_{i=1} p_T^{lep,i} + E_T^{miss}, \tag{18}$$

  where the sums run over the four highest p_T jets, and over all the identified leptons.

We will see shortly how we apply them to suppress the background.

2. Benchmark points

Even though the number of parameters is reduced down to five by imposing boundary conditions, the signals still depend strongly on the parameter set. Hence, seven benchmark points have been chosen by ATLAS Collaboration to do the detailed analysis [29].

Here we briefly review the signatures at the LHC from two of them, applying the discussions in the previous subsection. Extensive studies including the systematic uncertainties can be found in [29].

In Fig. 6, we show them (SU1, SU2) in the $(M_{1/2}, m_0)$ plane of mSUGRA. The SU1 represents the co-annihilation region, where the co-annihilation of the NLSP $\tilde{\tau}_1$ and the $\tilde{\chi}_1^0$ in the early Universe occurs effectively, as mentioned in the previous subsection. The

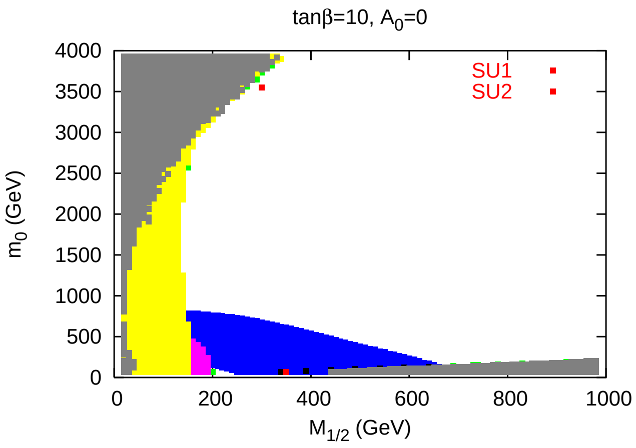

Figure 6: Regions in the $(M_{1/2}, m_0)$ plane of mSUGRA. The grey areas are those excluded by the EWSB condition or by tachyonic or too light sfermions. The region excluded by the Higgs and chargino mass constraints is shown in yellow and the one excluded by the $b \to s\gamma$ constraint (5) in pink. The blue area satisfies the $g_\mu - 2$ constraint (8), while green regions satisfy the Dark Matter constraint (4). Finally, black regions satisfy all constraints. The benchmark points are denoted with red dots. The figure is generated using `SOFTSUSY2.0` [30] and `micrOMEGAs 1.3.7` [31].

SU2 lies in the focus-point region, where the $\tilde{\chi}_1^0$ has the significant higgsino component, so that the $\tilde{\chi}_1^0$ pairs can annihilate to the weak gauge bosons. In both cases, therefore, the Dark Matter relic denisty is consistent with the WMAP observation. The mass spectra are listed in Table 3.

parameter	SU1	SU2
$M_{1/2}$ [GeV]	350	300
m_0 [GeV]	70	3550
A_0	0	0
tanβ	10	10

Table 2: The proposed benchmark points.

In SU1, the squarks and gluino masses are comparable, much heavier than the gauginos and sleptons. Nevertheless, their masses are below 1TeV, and the dominant sparticle production process is $qg \to \tilde{g}\tilde{q}_{L,R}$. The gluinos mainly decay to the third generation squarks (plus quarks), followed by squarks mainly decaying to $\tilde{\chi}_{1,2}^0$ and $\tilde{\chi}_{1,2}^\pm$ (plus quarks). The μ is large enough that the $\tilde{\chi}_2^0$ is mostly wino-like, which prefers decaying to the $SU(2)_L$ doublet sfermions; to the $\tilde{\tau}_1$ (plus tau) is dominant (by an order of magnitude), due to the large left-right mixing, while to the $\tilde{e}$, $\tilde{\mu}$ is suppressed by phase space.

spectra [GeV]	SU1	SU2	spectra [GeV]	SU1	SU2
μ	463	463	u_L, c_L	754	3547
χ_1^0	139	126	u_R, c_R	731	3559
χ_2^0	262	242	d_L, s_L	761	3547
χ_3^0	466	470	d_R, s_R	730	3560
χ_4^0	483	485	t_1	567	2074
$\chi_1^\pm$	262	242	t_2	753	2893
$\chi_2^\pm$	485	490	b_1	695	2890
$\tilde{g}$	824	810	b_2	729	3531
h^0	113	121	e_L, μ_L	251	3544
H^0, A^0	517	3532	e_R, μ_R	156	3548
$H^\pm$	523	3534	τ_1	147	3519
			τ_2	254	3529

Table 3: Mass spectra are calculated using `SOFTSUSY 2.0` [30]. All spectra are on-shell masses except the $\mu(M_{SUSY})$.

Nevertheless, tau identification is much more challenging than that of electron or of muon. When it decays leptonically, due to the presence of the neutrino, the kinematic reconstruction is impossible. For the hadronic decays, the resultant jets need to be distinguished from the QCD backgrounds. Thereby, we only quote the mass reconstruction from the dilepton (i.e. electron or muon) invariant mass here. The interested readers can find the studies on the tau final state in [29].

For the decay chain $\tilde{q}_L \to q\tilde{\chi}_2^0 \to \tilde{l}_{L,R}^{\pm} l^{\mp} q \to \tilde{\chi}_1^0 l^+ l^- q$, the distribution of the invariant mass of the two final leptons ends at

$$m_{ll}^{edg} = m_{\tilde{\chi}_2^0} \sqrt{1 - \left(\frac{m_{\tilde{l}}}{m_{\chi_2^0}}\right)^2} \sqrt{1 - \left(\frac{m_{\chi_1^0}}{m_{\tilde{l}}}\right)^2}. \tag{19}$$

The main background comes from $t\bar{t}$, where the top decays to the $bl^+\nu$. For the optimized event selection, the following cuts are applied [29]:

- $p_T(j1) > 200$GeV, $p_T(j2) > 150$GeV.
- Missing $E_T > 120$GeV.

Since the lepton pairs from the signal are of the opposite sign and the same flavor (OSSF), only OSSF lepton pairs are selected. Furthermore, since the lepton pairs from the background can be either of the different flavor or the same flavor with the same probability, the events with opposite sign opposite flavor (OSOF) lepton pairs are subtracted.

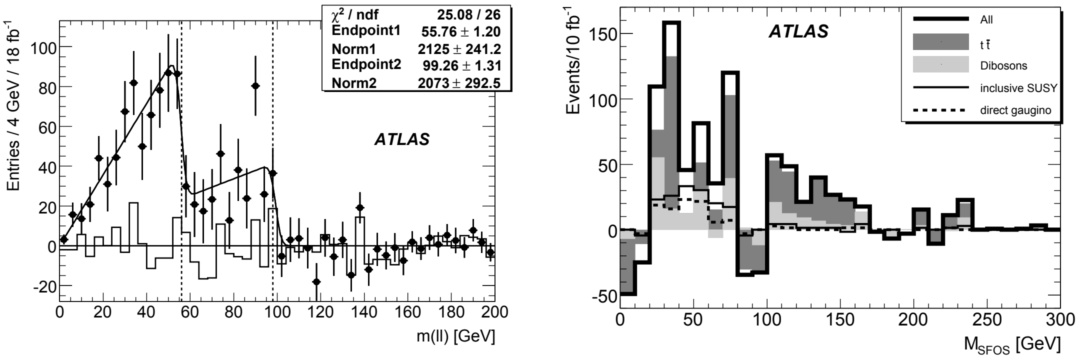

Figure 7: (a) Dilepton invariant mass distribution of (OSSF-OSOF) after cuts for SU1, taking into account the correction factor for the electron and the muon recontruction efficiencies. The points with error bars show SUSY plus Standard Model background, and the solid histogram shows Standard Model contribution alone. (b) Dilepton invariant mass distribution of (OSSF-$\overline{\text{OSSF}}$) after cuts for SU2. Adopted from [29].

The resulting dilepton invariant mass for the integrated luminosity of $18fb^{-1}$ is shown in Fig. 7 (a). The endpoint computed from the Eq. (19) (verticle lines) can be clearly seen.

In SU2, the squarks are significantly heavier than not only the gluino but also all of the neutralinos and charginos. As a consequence, the main SUSY production channels are the $gg \to \tilde{g}\tilde{g}$ as well as $q\bar{q} \to \tilde{\chi}_2^0\tilde{\chi}_1^{\pm}$. The $\tilde{\chi}_2^0$ ($\tilde{\chi}_1^{\pm}$) is wino-like, and it decays mainly to the $\tilde{\chi}_1^0$ plus sleptons via virtual Z (W) boson exchange. The gluino decays to the $\tilde{\chi}_{1,2}^{\pm}$, $\tilde{\chi}_2^{\pm}$ plus quark pairs via virtual squark exchange.

All Zb, diboson, and the $t\bar{t}$ contribute to the Standard Model background. In case of direct gaugino production, from the above decay channel only the small $\not{E}_T$ and the soft jets are produced, which makes it challenging to suppress the background. In the ATLAS study, the following cuts are applied [29], with a certain lepton isolation criteria:

- At least one pair of OSSF leptons.
- $N_l \geq 3$.
- No OSSF dilepton pair with 81.2GeV $< M_{ll} <$ 102.2GeV, to prevent those from Z boson.
- Missing $E_T >$ 30GeV.

Furthermore, the number of events with three leptons ($\overline{\text{OSSF}}$), which does not include an OSSF pair, is subtracted, considering that the backgrounds do not necessarily produce the OSSF pairs.

Note that once the sufficient integrated luminosity is collected, it will be relatively easy to distinguish the SUSY process coming from the gluino decay from the SM processes, by the additional cuts on the high p_T.

In Fig. 7 (b), the dilepton ivariant mass spectrum is shown for the integrated luminosity $10fb^{-1}$. We see the peak around 50GeV for the inclusive SUSY.

2.3 Supergravity Grand Unified Theory

In the previous section, we worked mainly under the universality conditions for the gaugino masses, scalar masses, and the trilinear parameters at the scale $M_{GUT} \simeq 10^{16}$GeV. In this section, we discuss a well-motivated extension of the mSUGRA, the supersymmetric Grand Unified Theories (SUSY-GUTs). In the next subsection, we begin with the discussions on the general features of the SUSY-GUTs by examining the minimal model [2, 3].

2.3.1 General Aspects

The simplest model of GUT is based on the SU(5) gauge group. The SU(5) unification extends to, at highest, the Planck scale, and is broken down to the MSSM at the GUT scale, when the **24** dimensional Higgs (Σ) obtains a vacuum expectation value. The symmetry breaking occurs via the super-Higgs mechanism, where the supersymmetry is preserved. The vacuum expectation value is determined by the F- as well as the D-flatness conditions.

The quark doublets, the u-type antiquark singlets and the antilepton singlets form a **10**- (T), and the d-type antiquark singlets and the lepton doublets are in a $\bar{\mathbf{5}}$ ($\overline{F}$) dimensional representation. The $\bar{\mathbf{5}}$-, **5**- dimensional Higgs (H_1, H_2) contain the MSSM Higgs doublet H_d, H_u, respectively.

The superpotential is given by

$$W = \lambda Tr\Sigma^3 + MTr\Sigma^2 + H_2(\lambda'\Sigma + M')H_1 + Tf_uTH_2 + Tf_d\bar{F}H_1\,. \qquad (20)$$

λ, M are the GUT Higgs self coupling, and the superpotential mass parameter, respectively. The M must be of order M_{GUT}, while M' is the generalization of the mSUGRA higgsino mass parameter. The corresponding soft supersymmetry breaking terms are parametrized as follows:

$$\begin{aligned}\mathcal{L}_{soft} &= -m_{H_1}^2|H_1|^2 - m_{H_2}^2|H_2|^2 - m_\Sigma^2 Tr\Sigma^\dagger\Sigma - m_5^2|\bar{F}|^2 - m_{10}^2 TrT^\dagger T \\ &- \frac{1}{2}M_5\bar{\lambda}\lambda \\ &+ \Big[B_\Sigma\mu_\Sigma Tr\Sigma^2 + A_\lambda\lambda Tr\Sigma^3 + B_H\mu_H H_1H_2 + A_{\lambda'}\lambda' H_1\Sigma H_2 \\ &+ A_u f_u\epsilon_{ijklm}T^{ij}T^{kl}H_2^m + A_d f_d T^{ij}\bar{F}_i H_{1j} + h.c.\Big], \qquad (21)\end{aligned}$$

As in mSUGRA, once we impose boundary conditions for the parameters at some high scale, we can obtain the low energy spectra via RGEs. Let us assume the following universality at M_P:

$$\begin{aligned}m_{10} = m_5 = m_{H_1} = m_{H_2} = m_\Sigma \equiv m_0, \\ A_u = A_d = A_\lambda = A_{\lambda'} \equiv A_0. \qquad (22)\end{aligned}$$

First, the gaugino loop contribution in the soft mass differs for the fields in different representation of SU(5) gauge group, which leads only the partial universality for the MSSM soft breaking parameters at M_{GUT}:

$$\begin{aligned}m_Q = m_U = m_E \equiv m_{10}, \quad m_D = m_L \equiv m_5, \\ m_{H_d} \equiv m_{H_1}, \quad m_{H_u} \equiv m_{H_2}. \qquad (23)\end{aligned}$$

Second, the novel coupling λ' in the Eq. (20) contributes to the m_{H_1}, m_{H_2}, such that they get more reduced at the weak scale. As a result, electroweak symmetry breaking requires larger values $|\mu|$ than in mSUGRA, which means that the lighter charginos and neutralinos are more gaugino-like.

Even though we discussed a specific model – the minimal SU(5) –, the nonuniversality in the scalar sector at the GUT scale as well as the modification on the low energy spectra due to the interplay between MSSM and the novel parameters are the generic features in the SUSY-GUT models. In the next subsection, we will adopt an SO(10) model, and perform an analysis at some length.

2.3.2 A Detailed Study: An SO(10) Model

1. Introduction to the Model

As mentioned in the Introduction, Grand Unified Theories (GUTs) based on the gauge group $SO(10)$ have been considered good candidates for the unification of electroweak and strong interactions [32]. All matter fields of one generation are incorporated in a single irreducible representation, the spinor **16**. Moreover, the "seesaw" mechanism [33], which can explain small neutrino masses as indicated by neutrino oscillations, is naturally embedded.

In [18], we in particular chose a model by Aulakh et al. [34], a supersymmetric $SO(10)$ model with two intermediate scales: $SO(10)$ is firstly broken to $SU(4)_C \times SU(2)_L \times SU(2)_R$ by a **54** dimensional Higgs at the GUT scale M_X; then to $SU(3)_C \times U(1)_{B-L} \times SU(2)_L \times SU(2)_R$ by **45** at scale M_C; finally to the Standard Model gauge group by $\mathbf{126} + \overline{\mathbf{126}}$ at scale M_R. Imposing the unification condition for the gauge couplings fixes the intermediate scales M_C and M_R for given M_X; i.e. M_X is a free parameter. However, its lower bound is set by the lower bound on the lifetime of the proton [5]. We took $M_X = 3 \cdot 10^{15}$GeV as default value. In addition, a second pair of Higgs doublets was introduced, in order to modify the minimal $SO(10)$ predictions for the masses of quarks and leptons, which are not consistent with experiments. In order to compare the low energy phenomenology of the model with that of mSUGRA [2], we assumed universal soft breaking parameters $(m_0, M_{1/2}, A_0)$ as boundary condition at the GUT scale.

The **126**–dimensional Higgs whose vacuum expectation value breaks $SU(2)_R \times U(1)_{B-L}$ to $U(1)_Y$ also gives Majorana masses to the right–handed neutrinos. The resulting masses for the light neutrinos are schematically written as

$$m_\nu = \frac{m_D^2}{M_N} = \frac{(Y_\nu \langle H_u^0 \rangle)^2}{Y_N \langle \overline{\mathbf{126}} \rangle}. \tag{24}$$

The Yukawa coupling Y_N, and to a lesser extent Y_ν, gives new contributions to the Renormalization Group Equations (RGEs) of the MSSM Yukawa couplings and soft breaking parameters. Therefore the weak–scale masses, and thus the radiative electroweak symmetry breaking and the relic density of Dark Matter, depend on Y_N, and hence on the light neutrino masses for fixed M_R. This remains qualitatively true for other $SO(10)$ GUTs with a "type–I" seesaw mechanism at an intermediate scale. Note that Y_ν unifies with the up–type quark Yukawa couplings, and is hence fixed. For given M_R, and hence given $\langle \overline{\mathbf{126}} \rangle$, the absolute scale of the light neutrino masses is thus determined by Y_N, with *larger* Y_N yielding *lighter* neutrinos. For our minimal choice $M_X = 3 \cdot 10^{15}$ GeV, the requirement that Y_N remains perturbative at least up to scale M_X therefore leads to the lower bound $m_\nu \gtrsim 0.15$ eV on the mass of the heaviest light neutrino.

For our current study the most important modification of the weak–scale spectrum is the reduction of the higgsino mass parameter $|\mu|$, which comes about as follows. The weak–scale stop masses are reduced compared to the mSUGRA prediction, due to the Yukawa coupling given by

$$W_{\text{Yuk},422} \ni \frac{1}{2} Y_N \left(F^c \overline{\Sigma}_R F^c + F \overline{\Sigma}_L F \right) . \tag{25}$$

Here $W_{\text{Yuk},422}$ is the superpotential valid between the scales M_C and M_X, $\overline{\Sigma}_R$ and $\overline{\Sigma}_L$ are in the $(\mathbf{10}, \mathbf{1}, \mathbf{3})$ and $(\overline{\mathbf{10}}, \mathbf{3}, \mathbf{1})$ representation, respectively, of the gauge group $SU(4)_C \times SU(2)_L \times SU(2)_R$, and F and F^c denote quark and lepton superfields in the **(4,2,1)** and

($\overline{\mathbf{4}}, \mathbf{1}, \mathbf{2}$) representation. This reduces the term $\propto Y_t^2$ in the RGE for $m^2_{H_u}$, leading to an increase of $m^2_{H_u}$ at the weak scale. As a result, electroweak symmetry breaking requires *smaller* values of $|\mu|$ than in mSUGRA does.

Another distinctive feature of the model is the rapid increase of the gauge couplings at high energies. This is due to the introduction of large additional Higgs representations, needed in order to break the gauge symmetry. As a result, relations between weak–scale and the GUT–scale soft breaking parameters are modified. In particular, for a given universal gaugino mass $M_{1/2}$ at the GUT scale, the $SO(10)$ model predicts much smaller gaugino masses at the weak scale than mSUGRA does.

2. Benchmark points

We performed detailed analyses of collider signals for two distinct benchmark points. The input parameters and superparticle and Higgs spectra are listed in Table 4. We chose points that satisfy all constraints, including the Dark Matter relic density constraint (but ignoring the indication of a deviation of the magnetic dipole moment of the muon from the Standard Model prediction [35]). We chose M_X at its lower bound of $3 \cdot 10^{15}$ GeV, and small $m_\nu = 0.2$ eV, in order to maximize the differences between our model and mSUGRA. On the other hand, we chose the parameters of the mSUGRA points such that the sparticle spectra are as similar as possible to that of the corresponding $SO(10)$ benchmark points. In particular, we adjust the values of $M_{1/2}$ such that the gluino masses are essentially the same in both models. In contrast, we chose the same m_0 in both models, since this gives similar first and second generation squark masses. In this way we hope to isolate the non–trivial effects of the additional couplings via the RGE.

Point 1 is chosen such that, at least in the $SO(10)$ model, the lightest neutralino has a significant higgsino component. This requires $m_0 > M_{1/2}$ even in this model. However, for the same gluino mass, one would need much larger m_0 to achieve a similarly small μ in mSUGRA. This would put squarks out of the reach of the LHC, making the scenario easily distinguishable from our $SO(10)$ point. We instead chose to increase $\tan\beta$ from 40 to 52, and also took a nonvanishing (but fairly small) A_0. This leads to greatly reduced mass of the CP–odd Higgs boson, i.e. we are now close to the "$A-$pole" region [36] where $\tilde{\chi}_1^0$ annihilation is enhanced since $A-$exchange in the $s-$channel becomes (nearly) resonant. These changes do not affect μ very much, i.e. in our mSUGRA point 1 the LSP remains a nearly pure bino.

Benchmark point 2 lies in the co–annihilation region. Recall that the new coupling Y_N reduces $m_{\tilde{\tau}_R}$ below its mSUGRA prediction. Chosing $M_{1/2}$ such that one gets the same $\tilde{g}$ (or $\tilde{\chi}_1^0$) mass, while keeping all other input parameters the same, would thus lead to an mSUGRA point with too high a relic density. We consider two different methods

parameter	SO(10) 1	mSUGRA 1	SO(10) 2	mSUGRA 2a	mSUGRA 2b
$M_{1/2}$	1100	600	1000	550	550
m_0	1400	1400	280	280	280
A_0	0	300	0	-120	0
$\tan\beta$	40	52	40	40	41.5
μ	307	587	607	682	663
χ_1^0	243	253	229	227	227
χ_2^0	313	468	430	431	430
χ_3^0	317	597	615	690	671
χ_4^0	519	618	628	698	680
$\chi_1^\pm$	298	470	434	434	433
$\chi_2^\pm$	517	615	625	694	676
$\tilde{g}$	1423	1427	1246	1258	1258
u_L, c_L	1865	1862	1168	1178	1177
u_R, c_R	1842	1836	1140	1140	1140
d_L, s_L	1870	1868	1175	1185	1184
d_R, s_R	1843	1831	1138	1135	1134
t_1	1205	1311	874	886	897
t_2	1409	1495	1062	1086	1088
b_1	1418	1463	998	1016	1017
b_2	1529	1532	1056	1074	1076
e_L, μ_L	1490	1461	544	473	473
e_R, μ_R	1466	1421	472	354	354
τ_1	900	960	238	237	238
τ_2	1230	1259	488	464	465
h^0	116	116	115	115	115
H^0, A^0	1018	588	580	615	593
$H^\pm$	1021	594	586	621	598
Ωh^2	0.09	0.09	0.11	0.11	0.12
P_τ	0.72	0.96	0.92	0.89	0.89

Table 4: Proposed benchmark points. Mass spectra are calculated using `SOFTSUSY 2.0`. All spectra from row 6 through 28 are on-shell masses except the $\mu(M_{SUSY})$. Rows 2 through 5 give the input parameters. We indicate also the LSP relic density and the longitudinal polarization of the τ lepton in $\tilde{\tau}_1^- \to \tau^- \tilde{\chi}_1^0$ decays. All dimensionful quantities are in GeV.

to correct for this. In mSUGRA point 2a we take non–vanishing A_0, such that $m_{\tilde{\tau}_R}$ is reduced and μ is increased; the latter also decreases $m_{\tilde{\tau}_1}$, helping to get a sufficiently large $\tilde{\chi}_1^0 - \tilde{\tau}_1$ co–annihilation cross section. In mSUGRA point 2b, this is instead achieved by increasing $\tan\beta$, which again reduces $m_{\tilde{\tau}_R}$ and increases $\tilde{\tau}_L - \tilde{\tau}_R$ mixing. Notice that in either case the change of these input parameters is not very dramatic.

At the $SO(10)$ point 1, all of the squarks as well as the gluino are significantly heavier than all of the neutralinos and charginos. Furthermore, due to the low value of $|\mu|$, the heaviest neutralino $\tilde{\chi}_4^0$ has the largest $SU(2)$ gaugino component. Due to the small higgsino mass, the dominant SUSY production channel is $q\bar{q} \to \tilde{\chi}_2^0 \tilde{\chi}_1^\pm$. Mostly due to this process, the total inclusive SUSY production cross section at $\sqrt{s} = 14$TeV is nearly three times larger than that of the mSUGRA point 1. However, $\tilde{\chi}_{2,3}^0$ and $\tilde{\chi}_1^+$ decay predominantly into $\tilde{\chi}_1^0$ and a quark–antiquark pair, which carries relatively little energy due to the small mass splitting. Direct $\tilde{\chi}_{2,3}^0 \tilde{\chi}_1^\pm$ production therefore predominantly gives rise to events with four relatively soft jets, and correspondingly only a small amount of missing E_T. This signal will be completely swamped by backgrounds, e.g. from W, Z plus multi–jet production. The inclusive cross section for squark and gluino production, which should be detectable in this scenario (see below), is quite similar in the $SO(10)$ and mSUGRA versions of point 1.

Another distinctive feature of $SO(10)$ point 1 is the much smaller polarization P_τ of τ leptons produced in $\tilde{\tau}_1^- \to \tau^- \tilde{\chi}_1^0$ decays. P_τ depends [37] both on $\tilde{\tau}_L - \tilde{\tau}_R$ mixing and on gaugino–higgsino mixing. In the case at hand, $\tilde{\tau}_1$ is dominated by the $\tilde{\tau}_R$ component in both the $SO(10)$ model and in mSUGRA; the $\tilde{\tau}_L$ component is slightly smaller in the $SO(10)$ case due to the reduced value of $\mu \tan\beta$. However, the $SO(10)$ model features much stronger bino–higgsino mixing in this case. Note that the bino couples $\tilde{\tau}_R$ to τ_R, while the (down–type) higgsino couples $\tilde{\tau}_R$ to τ_L. As a result, P_τ is significantly smaller in the $SO(10)$ case.

P_τ can be measured via the energies of hadronic τ decay products [38]. Of course, this requires a copious source of $\tilde{\tau}_1$ particles. At an e^+e^- collider this measurement can therefore only be performed if the beam energy is well above $m_{\tilde{\tau}_1}$, i.e. $\sqrt{s} \gtrsim 2$TeV in our case. Monte Carlo simulations indicate [39] that P_τ could then be determined with sufficient accuracy to distinguish these scenarios. At the LHC this measurement is probably only possible if $\tilde{\tau}_1$ particles are produced copiously in the decays of gluinos and/or squarks [40]; this is not the case in our benchmark point 1.

For the $SO(10)$ point 2, since the gluinos and squarks are relatively lighter, the dominant sparticle production process is $qg \to \tilde{g}\tilde{q}_{L,R}$. Our choices of $M_{1/2}$ and m_0 ensure that the corresponding cross section is very similar in the $SO(10)$ and both mSUGRA scenarios.

Recall that we adjusted the mSUGRA parameters such that we get very similar $m_{\tilde{\tau}_1}$, and hence similar LSP relic density, as in the $SO(10)$ scenario. These adjustments also imply that the masses of third generation squarks are only slightly smaller in the $SO(10)$ scenario than in both mSUGRA scenarios, i.e. the effect of the new Yukawa couplings on sfermion masses has been partly compensated by adjusting soft breaking parameters. However, the effect of the new couplings is still visible in $|\mu|$, which is significantly smaller in the $SO(10)$ benchmark point than in both mSUGRA variants.

Moreover, having adjusted parameters such that we obtain similar gaugino and first generation squark masses, we get significantly heavier first generation sleptons in $SO(10)$ than in mSUGRA [18]. This can be tested trivially at e^+e^- colliders operating at $\sqrt{s} > 2m_{\tilde{e}_R}$. However, even in the mSUGRA versions of our point 2, sleptons are too heavy for direct slepton pair production to yield a viable signal at the LHC [41].

3. Measurements using di–lepton events at the LHC

In order to analyze the gaugino–higgsino sector of the theory, we have to rely on neutralinos and charginos produced in the decays of squarks and gluinos. Direct production of charginos and neutralinos is only detectable in purely leptonic final states [42]. In the case at hand the relevant neutralino and chargino states are quite massive, and have small leptonic branching ratios, leading to very small signal rates.

We therefore look for events with several energetic jets in addition to two or more leptons. To that end, we simulate proton–proton collisions at the LHC ($\sqrt{s} = 14$TeV) using `PYTHIA 6.4` [43] and the toy detector PYCELL. The detector is assumed to cover pseudorapidity $|\eta| < 5$ with a uniform segmentation $\Delta\eta = \Delta\phi = 0.1$. We ignore energy smearing, which should not be important for our analyses. We use a cone jet algorithm, requiring the total transverse energy E_T summed over cells within $R = 0.4$ to exceed 10 GeV; here $R = \sqrt{(\delta\eta)^2 + (\delta\phi)^2}$, where $\delta\eta$ and $\delta\phi$ measure the deviation in pseudorapidity and azimuthal angle from the jet axis. $t\bar{t}$ and diboson production are assumed to be the main Standard Model backgrounds in the di–lepton channels we are interested in.

We require electrons and muons to be isolated, i.e. to have less than 10 GeV of additional E_T in a cone with $R = 0.2$ around them. Also, leptons within $R < 0.4$ of a jet are not counted. These requirements essentially remove leptons from the decay of c and b quarks. Finally, we require the invariant mass of opposite–sign, like–flavor lepton pairs to exceed 20 GeV, in order to suppress contributions involving virtual photons.

Point 1

In this case the difference in μ between the $SO(10)$ and mSUGRA scenarios is quite drastic: in the $SO(10)$ case, μ is only slightly above M_1 and well below M_2, leading to $m_{\tilde{\chi}_2^0} \simeq m_{\tilde{\chi}_3^0} \simeq m_{\tilde{\chi}_1^\pm}$ only about 70 GeV above the LSP mass, and well below the masses of the wino–like $\tilde{\chi}_2^\pm$ and $\tilde{\chi}_4^0$ states. In contrast, in the mSUGRA scenario we have μ slightly above M_2, leading to wino–like $\tilde{\chi}_2^0$ and $\tilde{\chi}_1^\pm$ well above the LSP.

In order to understand what this means for multi–jet plus di–lepton signatures, we have to analyze the most important sparticle production and decay channels. In the case at hand, the most important production channels (after cuts) are squark pair and associated squark plus gluino production, where the squarks are in the first generation. Most squarks will decay into a gluino and a quark here, so that most events start out as gluino pairs with one or two additional jets.

In the $SO(10)$ version of point 1, nearly all gluinos decay into $\tilde{t}_1$ plus top, since this is the only allowed two–body decay of the gluino. In turn, $\tilde{t}_1$ decays mostly into $\tilde{\chi}_1^+ b$ and $\tilde{\chi}_{1,2,3}^0 t$. These decays are preferred by phase space, and because here the *lighter* neutralinos and *lighter* chargino are dominantly higgsino–like, and hence couple more strongly to (s)top (since the top Yukawa coupling is larger than the electroweak gauge couplings). Leptons can then originate from semi–leptonic decays of top quarks, from leptonic decays of $\tilde{\chi}_1^\pm$ states, and from leptonic decays of $\tilde{\chi}_{2,3}^0$. Note that the latter decays, which have branching ratios near 3%, can only produce di–lepton pairs with invariant mass below 70 GeV.

In contrast, in the mSUGRA version of point 1, gluinos can only undergo three–body decays. Nevertheless decays involving third generation quarks are strongly preferred, since the $\tilde{b}_1$ and $\tilde{t}_1$ exchanged in $\tilde{g}$ decay can be nearly on–shell. The dominant decay modes again involve higgsino–like states, i.e. $\tilde{g} \rightarrow \tilde{\chi}_2^+ b\bar{t}$ or $\tilde{\chi}_{3,4}^0 t\bar{t}$; due to the larger phase space, the branching ratio for $\tilde{g} \rightarrow \tilde{\chi}_1^+ b\bar{t}$ is also significant. The higgsino–like states decay into lighter gaugino–like states plus a real gauge or Higgs boson. Leptons can then originate from semi–leptonic top decays, and from the decays of the $W^\pm$ and Z^0 decays produced in the decays of the heavier neutralinos and both charginos. Note that we do not expect any structure in the di–lepton invariant mass below M_Z in this case.

We apply the following cuts to suppress the Standard Model background [29]:

- At least four jets with $E_T > 150$ GeV each, at least one of which satisfies $E_T > 300$ GeV.
- Missing $E_T > 200$ GeV.
- Transverse sphericity $S_T > 0.2$.
- Two charged leptons with opposite sign and same flavor (OSSF).

No SM diboson event passed these cuts. One $t\bar{t}$ event passed, for a simulated integrated luminosity of 1 fb^{-1}. Note that our cuts are quite generic, not optimized for our scenario. In our case, the background can be further suppressed by requiring at least three tagged

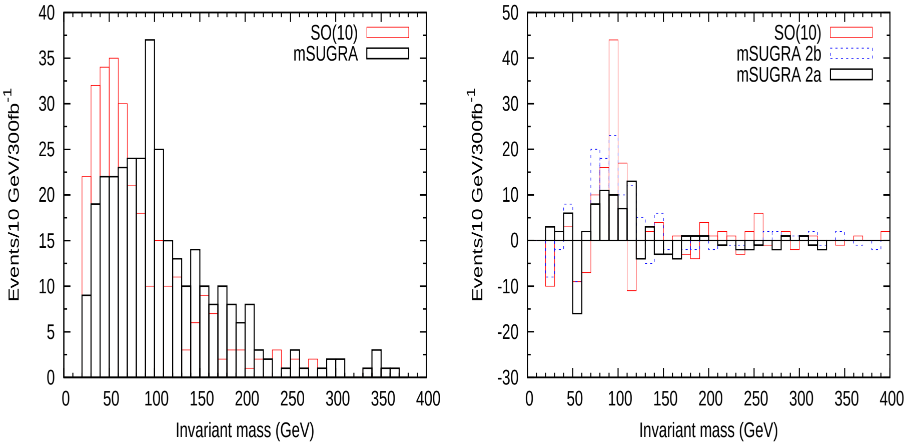

Figure 8: (a) The dilepton invariant mass distribution of opposite sign, same flavor dilepton events after cuts for point 1, corresponding to an integrated luminosity of 300 fb^{-1}; the black and red (grey) histograms are for the mSUGRA and $SO(10)$ versions of this point, respectively. (b) The subtracted (OSSF−OSOF) dilepton invariant mass distribution after cuts for point 2; the solid black and dashed blue histograms are for the mSUGRA points 2a and 2b, while the solid red (grey) histogram is for the $SO(10)$ version.

b quarks in the event (all the final states we discussed above have at least four b quarks); by requiring the presence of additional jets (most events will have at least one hard jet in addition to the gluino pair, which by itself already produces at least four jets); and/or by optimizing the numerical values of the cuts employed. This should allow to extract an almost pure SUSY sample, without significant loss of signal.

The results of our simulations for point 1 are shown in the left frame of Fig. 8. We see that the di–lepton invariant mass distributions peaks near 50 GeV in the $SO(10)$ scenario, whereas it peaks at M_Z in the mSUGRA scenario. mSUGRA also predicts a somewhat larger number of events at large di–lepton invariant mass; we saw above that only in this scenario we expect significant numbers of on–shell $W^\pm$ bosons from chargino and neutralino decay. The two distributions should be easily distinguishable, with high statistical significance, once several hundred fb^{-1} of data will have been collected.

Point 2

We now turn to the benchmark point 2. We saw in Table 4 that now $\tilde\chi_2^0 \to \tilde e_R^\pm e^\mp$ are allowed in the mSUGRA scenarios, but not in $SO(10)$. Unfortunately, the branching ratios for these decays remain at the permille level even in the mSUGRA scenarios. This is partly due to the small phase space available for these decays, but mostly due to the fact that $\tilde\chi_2^0$ is dominantly a neutral wino in the co–annihilation region, and thus has only small couplings to $SU(2)$ singlet sleptons; recall that $\tilde\tau_1$ also has a significant $SU(2)$ doublet, $\tilde\tau_L$

component. As a result, we do not see any evidence for $\tilde{\chi}_2^0 \to \tilde{\ell}_R^{\pm}\ell^{\mp} \to \tilde{\chi}_2^0\ell^{\pm}\ell^{\mp}$ $(\ell = e,\ \mu)$ in the mSUGRA scenarios; in particular, no kinematic edge at $m_{\ell^+\ell^-} = 189$ GeV, the nominal endpoint for this decay chain, is visible.

We instead first try to find evidence for increased gaugino–higgsino mixing in the $SO(10)$ scenario, due to the lower value of μ, by analyzing the decays of the heavier charginos and neutralinos. In the case at hand the dominant production channel is associate production of a first generation squark with a gluino. The decays of first and second generation squarks will predominantly produce $\tilde{\chi}_{1,2}^0$ and $\tilde{\chi}_1^{\pm}$ states. On the other hand, here in the co–annihilation region gluinos are heavier than all squarks, but – as usual in scenarios where squark masses unify at some high scale [44] – gluino decays into third generation quarks and squarks are preferred. We saw in the discussion of benchmark point 1 that third generation squarks in turn frequently decay into higgsino–like charginos and neutralinos. We look for these heavier states through their decays into real Z^0 bosons.

Modes	$SO(10)$ 2	mSUGRA 2a	mSUGRA 2b
$\tilde{g} \to \tilde{b}_1\bar{b}$	12.3 %	11.8 %	12.0 %
$\tilde{g} \to \tilde{b}_2\bar{b}$	7.0 %	6.2 %	6.2 %
$\tilde{g} \to \tilde{t}_1\bar{t}$	12.3 %	12.5 %	11.8 %
$\tilde{g} \to \tilde{t}_2\bar{t}$	2.9 %	-	-
$\tilde{t}_1 \to \tilde{\chi}_3^0 t$	18.1 %	5.2 %	13.6 %
$\tilde{t}_1 \to \tilde{\chi}_2^+ b$	21.9 %	21.3 %	22.5 %
$\tilde{t}_2 \to \tilde{\chi}_3^0 t$	10.4 %	8.0 %	8.9 %
$\tilde{t}_2 \to \tilde{\chi}_2^+ b$	24.8 %	20.4 %	22.6 %
$\tilde{t}_2 \to Z^0\tilde{t}_1$	7.4 %	9.3 %	7.5 %
$\tilde{b}_1 \to \tilde{\chi}_3^0 b$	14.6 %	10.7 %	12.2 %
$\tilde{b}_1 \to \tilde{\chi}_2^- t$	14.5 %	8.7 %	9.8 %
$\tilde{b}_2 \to \tilde{\chi}_3^0 b$	14.6 %	11.9 %	12.9 %
$\tilde{b}_2 \to \tilde{\chi}_2^- t$	46.1 %	39.0 %	40.9 %
$\tilde{\chi}_3^0 \to \tilde{\chi}_{1,2}^0 Z^0$	29.3 %	28.0 %	28.0 %
$\tilde{\chi}_2^+ \to \tilde{\chi}_1^+ Z^0$	23.8 %	22.8 %	22.4 %
$\tilde{g} \to Z^0 X$	7.6%	4.3%	5.0 %

Table 5: Branching ratios for important modes in benchmark point 2, as calculated with `ISAJET 7.78` [45]; note that charge conjugate gluino decay modes have to be added. The last line denotes the sum of the branching ratios of all gluino decay chains which give us a Z boson in the final state.

The relevant branching ratios are summarized in Table 5. We see that the slightly reduced third generation squark masses of the $SO(10)$ scenario increase the branching ratio for gluino decays into the third generation to 69% in the $SO(10)$ case, compared to 61% (60%) in mSUGRA point 2a (2b). Moreover, the decays of third generation squarks into $\tilde{\chi}_3^0$ and $\tilde{\chi}_2^\pm$ are enhanced in the $SO(10)$ case. This is also predominantly a phase space effect; the slightly reduced squark masses in the $SO(10)$ case are over–compensated by the reduced masses of the higgsino–like states. This effect is especially drastic for $\tilde{t}_1 \to \tilde{\chi}_3^0 t$, where the available phase space volume is very small in the mSUGRA scenarios. However, the strong phase space dependence of the relevant partial widths[5] [2, 3] leads to quite significant differences also in many other modes.[6] Finally, the smaller value of μ in the $SO(10)$ scenario also leads to more higgsino–gaugino mixing, and hence to slightly larger branching ratios for decays of the heavier neutralinos and charginos into real Z^0 bosons. The combination of these three effects leads to a substantially larger Z^0 production rate in gluino cascade decays in the $SO(10)$ scenario than in mSUGRA.

In order to suppress backgrounds, we first make use of the fact that most signal events will have (at least) one very energetic jet from the decay of a first generation squark into a light gaugino–like state. Moreover, the above discussion shows that many events with real Z^0 bosons in the final state also will have a top quark in the final state, and/or a real $W^\pm$ boson from $\tilde{\chi}_1^\pm$ decay; the branching ratio for this latter decay amounts to 12.6% in the $SO(10)$ scenario. The decays of these particles can lead to additional, somewhat softer, jets and/or additional leptons. On the other hand, since the dominant production channel only contains a single gluino, we only expect two b (anti–)quarks in the final state; $b-$tagging will therefore not be of much help to suppress the $t\bar{t}$ background, which we again expect to be the most dangerous one.

This leads us to use two complementary sets of cuts; at the end we simply add both event samples in order to increase the statistics:

1) Set 1

   - $E_T(j_1) > 600$ GeV, $E_T(j_2) > 200$ GeV, $E_T(j_3) > 100$ GeV.
   - $N_\ell = 2$.

2) Set 2

   - $E_T(j_1) > 300$ GeV, $E_T(j_2) > 150$ GeV, $E_T(j_3) > 75$ GeV.

---

[5] If m_q is negligible, the partial width for $\tilde{q} \to \tilde{\chi} + q$ is $\propto (1 - m_{\tilde{\chi}}^2/m_{\tilde{q}}^2)^2$.

[6] This also holds for decays into $\tilde{\chi}_4^0$. However, $\text{Br}(\tilde{\chi}_4^0 \to \tilde{\chi}_{1,2}^0 Z^0)$ only amounts to $\sim 3\%$. This large difference between the decay modes of the higgsino–like states $\tilde{\chi}_3^0$ and $\tilde{\chi}_4^0$ can be traced back to the fact that $\tilde{\chi}_3^0$ is a very pure *symmetric* higgsino, i.e. the higgsino components of this eigenvector are nearly equal in both magnitude and sign, whereas $\tilde{\chi}_4^0$ is mostly an *antisymmetric* higgsino. As a result, the $\tilde{\chi}_4^0 \tilde{\chi}_{1,2}^0 Z^0$ couplings are suppressed, and the $\tilde{\chi}_4^0 \tilde{\chi}_{1,2}^0 h$ couplings are enhanced, where h is the light neutral Higgs boson.

- $N_\ell \geq 3$.

Note that we do not apply any cut on missing E_T, since this wasn't necessary to suppress the backgrounds we studied. In Set 1, a modest missing E_T cut will be needed to suppress the Z^0+jets background, but this can be done without any significant loss of signal.

For set 1, we require both charged leptons to be of opposite charge. In set 2, we chose the opposite–sign lepton pair whose invariant mass is closer to M_Z as "Z^0 candidate". We found that the background from $t\bar{t}$ is almost entirely removed by either set of cuts. Furthermore, in order to extract the lepton pairs from the decays of Z^0 bosons, we subtract the events with opposite sign opposite flavor (OSOF) lepton pairs. This removes SUSY backgrounds where the two leptons originate from independent (semi–)leptonic decays; in benchmark point 2, these come primarily from the decays of $W^\pm$ bosons.

The resulting di–lepton invariant mass spectrum is shown in Fig. 8 (b), for an integrated luminosity of 300 fb^{-1}. We see that the Z^0 peak is indeed much more pronounced in the $SO(10)$ scenario than in the two mSUGRA scenarios. This allows to distinguish between $SO(10)$ and mSUGRA at about 3σ statistical significance in this case.

As noted above, in the $SO(10)$ point 2, we find a branching ratio for $\tilde{\chi}_1^\pm \to W^\pm \tilde{\chi}_1^0$ of about 12.6%. In the mSUGRA points 2a and 2b, this branching ratio is only 6.1% and 6.6%, respectively. At an e^+e^- linear collider with sufficient energy to produce $\tilde{\chi}_1^+\tilde{\chi}_1^-$ pairs this large difference in branching ratios should be straightforward to measure.

At the LHC we have to pursue a somewhat different strategy: Leptonic decays of these $W^\pm$ can give rise to events with two leptons of the *same* charge (like–sign di–lepton events). These can originate from associate $\tilde{q}_L\tilde{g}$ production where $\tilde{g}$ decay also produces a lepton; the charge of this lepton from gluino decay is uncorrelated to that from squark decay, i.e. half the time the two leptons will have the same charge. The results of Table 5 indicate that the inclusive branching ratio for $\tilde{g} \to \ell^\pm$ is somewhat higher in the $SO(10)$ scenario than in both mSUGRA analogues. Other sources are $\tilde{u}_L\tilde{u}_L$ and $\tilde{d}_L\tilde{d}_L$ production, which give rise to $\ell^+\ell^+$ and $\ell^-\ell^-$ pairs, respectively, if both squarks decay into $\tilde{\chi}_1^\pm$. Of course, gluino pairs can also produce like–sign dileptons, but the gluino pair production cross section is relatively small at this benchmark point. Note also that the physics background for like–sign dileptons events is very small.

We applied the following cuts to isolate a clean sample of SUSY events:

- At least two jets, with $E_T(j_1) > 500$ GeV, $E_T(j_2) > 200$ GeV. These cuts are quite asymmetric, since we expect at least one very energetic jet from $\tilde{q}_L$ decay in the event.

- Exactly two equally charged isolated leptons, with $p_T(\ell) > 10$ GeV as before.

With these cuts, we find 492 events in 300 fb^{-1} for the $SO(10)$ scenario, as compared to 422 and 434 events in mSUGRA 2a and 2b, respectively. This difference of ~ 3 statistical standard deviations is much less than the above discussion would lead one to expect. The reason is that there is another large source of $\ell^\pm$ from $\tilde{q}_L$ decay: $\tilde{q}_L \to q\tilde{\chi}_2^0$ with $\tilde{\chi}_2^0 \to \tau^\pm \tilde{\tau}_1^\mp$, and $\tau^\pm \to \ell^\pm \nu \bar{\nu}$.[7] Unfortunately the branching ratios for these decays are somewhat *larger* in mSUGRA than in the $SO(10)$ scenario, because higgsino–gaugino mixing tends to suppress the corresponding partial widths. This significantly reduces the difference between the predictions for the total like–sign dilepton event rate.

One can imagine two strategies to enhance the difference between the predictions. One possibility is to veto leptons from $\tilde{\chi}_2^0 \to \tau^\pm \tilde{\tau}_1^\mp$ decays by vetoing against the secondary $\tau^\mp$ from $\tilde{\tau}_1^\mp$ decay. However, this τ will be quite soft, so it is not clear how efficient such a τ veto would be. Another possibility is to subtract this source of hard leptons, by using events with an identified τ jet and the known τ decay branching ratios. Again, the feasibility of this method depends on τ tagging efficiencies and their uncertainties. We do therefore not pursue this strategy any further.

4. Measurements involving Higgs bosons at the LHC

Our benchmark points have quite large values of $\tan\beta$. This increases the cross sections for inclusive $gg \to A,\, H$ production, and for associate $gg \to b\bar{b}(A,\, H)$ production. The heavy Higgs bosons can be searched for using their decays into $\tau^+\tau^-$. According to simulations by the CMS collaboration [46], for $\tan\beta = 40$ this would allow discovery of the heavy Higgs bosons out to $m_A \simeq 650$ GeV with 60 fb^{-1} of data. In particular, we expect a robust signal for H, A production in the mSUGRA version of benchmark point 1, but not in the $SO(10)$ version. In benchmark point 2, we expect signals of comparable size in all three cases. The $\tau^+\tau^-$ invariant mass resolution should suffice to distinguish between the $SO(10)$ and mSUGRA 2a scenarios, but distinguishing the $SO(10)$ scenario from mSUGRA 2b might be challenging.

In benchmark point 2, $\tilde{\chi}_2^0 \to \tilde{\chi}_1^0 + h$ decays might also allow to discriminate between $SO(10)$ and the two mSUGRA analogues. The branching ratio for this decay is 11.5% in the $SO(10)$ case, but only 5.3% (5.7%) for mSUGRA 2a (2b). About 90% of the light Higgs bosons will decay into $b\bar{b}$ pairs. Recall, however, that in this scenario gluino decays frequently lead to $b\bar{b}$ pairs in the final state, giving rise to a large SUSY background. We have therefore not pursued this avenue further.

---

[7] The decay of the $\tilde{\tau}_1$ produced in this chain, or via the dominant decay $\tilde{\chi}_1^\pm \to \tilde{\tau}_1^\pm \nu$, only produces very soft τ leptons, and hence even softer $\ell^\pm$, since we are in the co–annihilation region where the $\tilde{\tau}_1^\pm - \tilde{\chi}_1^0$ mass difference is small.

2.4 $N = 2$ Supersymmetry

In this section, we investigate another possibility as an extension of the MSSM, the $N = 2$ supersymmetry [4].

In $N = 2$ supersymmetry, however, the standard left(L)/right(R)-handed matter supermultiplets are complemented with new R/L-handed matter multiplets. To keep the theory chiral, in agreement with experimental observations,[8] the masses of the new multiplets must be chosen to be very large so that $N = 2$ supersymmetry is effectively reduced to $N = 1$ supersymmetry in this sector. Exceptions are the two Higgs doublets which can be associated with the two supermultiplets within a Higgs hypermultiplet. Since the gauge and Higgs sectors are framed in the $N = 2$ formalism, but the matter sector in $N = 1$ is not, the theory is conventionally termed $N = 1/N = 2$ hybrid theory.

We begin with reviewing the theoretical basis. In the following subsections, we will perform detailed studies in the color sector, and in the electroweak sector, respectively.

2.4.1 Theoretical basis

The $N = 2$ gauge hypermultiplets $\mathcal{G} = \{\hat{G}, \hat{\Sigma}\}$ can be decomposed into the usual $N = 1$ vector supermultiplets of gauge and gaugino fields $\hat{G} = \{G_\mu, \tilde{G}\}$, complemented by chiral supermultiplets of novel gaugino and scalar fields $\hat{\Sigma} = \{\tilde{G}', \sigma\}$. The new gauge/gaugino fields, together with the MSSM fields, are shown explicitly for the color SU(3)$_C$ and the electroweak isospin SU(2)$_I$ and hypercharge U(1)$_Y$ gauge groups in Table 6.[9]

In parallel to the gauge fields, the neutral gaugino fields $\tilde{G}$ are self-conjugate Majorana fields with two helicity components, analogously the novel gaugino fields $\tilde{G}'$. [10] To match the two gaugino degrees of freedom in the new chiral supermultiplet, the components of the scalar fields σ are complex. Suitable mass matrices provided, the two gaugino Majorana fields $\tilde{G}$ and $\tilde{G}'$ can be combined to a Dirac field $\tilde{G}_D$.

In a similar way, the two Higgs-doublet superfields $\hat{H}_d$ and $\hat{H}_u^\dagger$ of the MSSM can be united to an $N = 2$ hyperfield $\mathcal{H} = \{\hat{H}_d, \hat{H}_u^\dagger\}$ [10]. It may be noted that, after diagonalizing the off-diagonal 2×2 mass matrix, the two neutral higgsinos can be interpreted as a Dirac field.

Corresponding to the complex spectrum of fields, a set of actions with different bases and characteristics describes the $N = 1/N = 2$ hybrid theory. The $N = 2$ action of

---

[8] Including such a large number of new matter fields would also make the entire theory asymptotically non-free.[56]

[9] Note that in this section we use the subscript "I" for the SU(2) gauge group to emphasize the electroweak isospin, while in the Introduction and in the previous section we have used "L" in contradistinction to the $SU(2)_R$ in Pati-Salam group.

[10] The notation $G_\mu, \tilde{G}, \tilde{G}', \sigma$ is used generically for gauge, gaugino and sigma fields; when specific gauge groups are referred to, the notation follows Table 6.

superfields	$\mathrm{SU}(3)_C, \mathrm{SU}(2)_I, \mathrm{U}(1)_Y$	Spin 1	Spin 1/2	Spin 0
$\hat{G}_C$ / color	$\mathbf{8}, \mathbf{1}, \mathbf{0}$	g^a	$\tilde{g}^a$	
$\hat{G}_I$ / isospin	$\mathbf{1}, \mathbf{3}, \mathbf{0}$	W^i	$\tilde{W}^i$	
$\hat{G}_Y$ / hypercharge	$\mathbf{1}, \mathbf{1}, \mathbf{0}$	B	$\tilde{B}$	
$\hat{\Sigma}_C$ / color	$\mathbf{8}, \mathbf{1}, \mathbf{0}$		$\tilde{g}'^a$	σ_C^a
$\hat{\Sigma}_I$ / isospin	$\mathbf{1}, \mathbf{3}, \mathbf{0}$		$\tilde{W}'^i$	σ_I^i
$\hat{\Sigma}_Y$ / hypercharge	$\mathbf{1}, \mathbf{1}, \mathbf{0}$		$\tilde{B}'$	σ_Y^0

Table 6: The $N = 2$ gauge hyper-multiplets for the color $\mathrm{SU}(3)_C$, isospin $\mathrm{SU}(2)_I$ and hypercharge $\mathrm{U}(1)_Y$ groups. Here, the superscripts $a =$ 1-8 and $i =$ 1-3 denote the $\mathrm{SU}(3)_C$ color and $\mathrm{SU}(2)_I$ isospin indices, respectively.

the gauge hypermultiplet $\mathcal{G} = \{\hat{G}, \hat{\Sigma}\}$ consists of the usual $N = 1$ action of the gauge supermultiplet $\hat{G}$ plus the action of the chiral supermultiplet $\hat{\Sigma}$ which couples the new gaugino and scalar fields to the gauge superfield:

$$\mathcal{A}_G = \sum \frac{1}{16 g^2 k} \int d^4x\, d^2\theta \;\; \mathrm{tr}\, \hat{G}^\alpha \hat{G}_\alpha \tag{26}$$

$$\mathcal{A}_\Sigma = \sum \int d^4x\, d^2\theta d^2\,\bar{\theta} \;\; \hat{\Sigma}^\dagger \exp[\hat{G}]\, \hat{\Sigma}\,, \tag{27}$$

the sums running over the gauge groups $\mathrm{SU}(3)_C$, $\mathrm{SU}(2)_I$ and $\mathrm{U}(1)_Y$. g are the gauge couplings (denoted by g_s, g and g' for color, isospin and hypercharge) and k are the corresponding quadratic Casimir invariants $C_2(G)$. $\hat{G}_\alpha = 2g\hat{G}^a_\alpha T^a$ are the gauge superfield-strengths, T^a the generators in the adjoint representation; the traces run over gauge-algebra indices, which are not shown explicitly. To this class of actions belongs also the standard (s)lepton/(s)quark gauge action

$$\mathcal{A}_Q = \sum \int d^4x\, d^2\theta d^2\bar{\theta} \;\; \hat{Q}^\dagger \exp[\hat{G}]\, \hat{Q}\,, \tag{28}$$

summed over the standard matter chiral superfields (denoted generically as $\hat{Q}$).

These actions are complemented by gauge-invariant $N = 1$ supersymmetric Majorana mass terms M' for the new gauge superfields and Dirac mass terms M^D coupling the original and new gauge superfields:

$$\mathcal{A}_{M'} = \int d^4x\, d^2\theta\, M'\, \mathrm{tr}\, \hat{\Sigma}\, \hat{\Sigma}\,, \tag{29}$$

$$\mathcal{A}_D = \int d^4x\, d^2\theta\, M^D\, \mathrm{tr}\, \theta^\alpha \hat{G}_\alpha \hat{\Sigma}\,. \tag{30}$$

$\mathcal{A}_{M'}$, bilinear in the Σ fields, is part of the superpotential of the theory. The Dirac mass term can be generated, *e.g.*, by the interaction $\sqrt{2}\hat{X}^\alpha \hat{G}_\alpha \hat{\Sigma}/M_X$ when a hidden-sector

$U(1)'$ spurion superfield acquires a D-component vacuum expectation value $\hat{X}^\alpha = \theta^\alpha D_X$, giving rise to the Dirac mass $M^D = D_X/M_X$ [47].

According to the general rules, this set of actions generates D-terms bilinear in the usual slepton and squark fields and linear in the new scalar sigma field with a coefficient given by the Dirac mass M^D. When the auxiliary fields D are eliminated through their equations of motion, the sigma fields get coupled to bilinears of the slepton and squark fields with strength M^D.

The Higgs sector is extended by the interactions with the non-colored scalar sigma fields. The $N=2$ Higgs supermultiplets $\hat{H}_d$ and $\hat{H}_u^\dagger$ are coupled to the $\mathrm{SU}(2)_I \times \mathrm{U}(1)_Y$ supergauge fields in the usual way,

$$\mathcal{A}_H = \sum_{i=u,d} \int d^4x\, d^2\theta d^2\,\bar{\theta}\, \hat{H}_i^\dagger \exp[\hat{G}_I + \hat{G}_Y]\, \hat{H}_i\,. \tag{31}$$

The part of the superpotential which includes Higgs fields, consists of the standard $N=1$ bilinear μ-term,

$$\mathcal{A}_\mu = \int d^4x\, d^2\theta\, \mu \hat{H}_u \cdot \hat{H}_d\,, \tag{32}$$

and the trilinear Higgs Yukawa terms involving the matter fields, which can be adopted from the $N=1$ theory:

$$\mathcal{A}'_Q = \int d^4x\, d^2\theta \;\; \sum g_Q\, \hat{q}^c \hat{Q} \cdot \hat{H}_q\,, \tag{33}$$

the dots denote the asymmetric contraction of the multiplet components. New trilinear interactions are predicted in $N=2$ supersymmetry [4] which couple the two supercomponents of the Higgs hypermultiplet with the new chiral superfields in the superpotential:

$$\mathcal{A}'_H = \int d^4x\, d^2\theta\, \frac{1}{\sqrt{2}} \hat{H}_u \cdot (\lambda_I \hat{\Sigma}_I + \lambda_Y \hat{\Sigma}_Y) \hat{H}_d\,. \tag{34}$$

In $N=2$ supersymmetry the couplings λ_I, λ_Y are identified with the $\mathrm{SU}(2)_I$ and $\mathrm{U}(1)_Y$ gauge couplings,

$$\lambda_I = g/\sqrt{2}\,, \quad \lambda_Y = -g'/\sqrt{2}\,. \tag{35}$$

In our numerical analyses we will treat them as independent couplings.

It may be noticed that the Majorana action $\mathcal{A}_{M'}$, the μ-term $\mathcal{A}_\mu$ and the trilinear Higgs-sigma term $\mathcal{A}'_H$ are manifestly not R-invariant.

Finally the bilinear and trilinear soft supersymmetry breaking terms must be added to the gauge, Higgs and matter Lagrangians:

$$
\begin{aligned}
-\mathcal{L}_{gauge,soft} &= \tfrac{1}{2}M_{\tilde{B}}\,\tilde{B}\,\tilde{B} + \tfrac{1}{2}M_{\tilde{W}}\,\left(\tilde{W}^+\,\tilde{W}^- + \tilde{W}^-\,\tilde{W}^+ + \tilde{W}^0\,\tilde{W}^0\right) + \tfrac{1}{2}M_{\tilde{g}}\,\tilde{g}^a\,\tilde{g}^a + \text{h.c.} \\
&+ m_Y^2\,|\sigma_Y^0|^2 + \tfrac{1}{2}\left(m_Y'^2\sigma_Y^{02} + \text{h.c.}\right) + m_I^2\,\left|\sigma_I^i\right|^2 + \tfrac{1}{2}\left(m_I'^2\sigma_I^{i2} + \text{h.c.}\right) \\
&+ m_C^2\,|\sigma_C^a|^2 + \tfrac{1}{2}\left(m_C'^2\sigma_C^{a2} + \text{h.c.}\right)\,, \qquad (36) \\
-\mathcal{L}_{Higgs,soft} &= m_{H_u}^2\,\left(\left|H_u^+\right|^2 + \left|H_u^0\right|^2\right) + m_{H_d}^2\,\left(\left|H_d^-\right|^2 + \left|H_d^0\right|^2\right) \\
&+ \left[B_\mu\,\left(H_u^+\,H_d^- - H_u^0\,H_d^0\right) + \text{h.c.}\right] \\
&+ \left[A_Y\,\lambda_Y\,\sigma_Y^0\,\left(H_u^+\,H_d^- - H_u^0\,H_d^0\right) + A_I\,\lambda_I\,\sigma_I^i\,\left(H_u\cdot\tau^i\,H_d\right) + \text{h.c.}\right]\,, \qquad (37)
\end{aligned}
$$

with i and a being the $\text{SU}(2)_I$ and $\text{SU}(3)_C$ indices, τ^i being the Pauli matrices and, finally,

$$
\begin{aligned}
-\mathcal{L}_{matter,soft} &= \left(m_{\tilde{Q}}^2\right)_{ij}\left(\tilde{u}_{iL}^*\tilde{u}_{jL} + \tilde{d}_{iL}^*\tilde{d}_{jL}\right) + \left(m_{\tilde{u}}^2\right)_{ij}\,\tilde{u}_{iR}^*\tilde{u}_{jR} + \left(m_{\tilde{d}}^2\right)_{ij}\,\tilde{d}_{iR}^*\tilde{d}_{jR} \\
&+ \left(m_{\tilde{L}}^2\right)_{ij}\left(\tilde{\nu}_{iL}^*\tilde{\nu}_{jL} + \tilde{e}_{iL}^*\tilde{e}_{jL}\right) + \left(m_{\tilde{e}}^2\right)_{ij}\,\tilde{e}_{iR}^*\tilde{e}_{jR}\,, \qquad (38)
\end{aligned}
$$

with i,j now denoting the matter generations. Here, the convention is adopted to use subscripts C, I, Y for parameters corresponding to color, isospin and hypercharge gauge groups, respectively. Capitalized mass parameters M are the Majorana gaugino masses (M^D for Dirac), while lower-case m denotes soft scalar masses. Note that, unlike for chiral matter fermions, the soft mass terms $M'_{\tilde{B}}, M'_{\tilde{W}}, M'_{\tilde{g}}$ for gauge adjoint fermions are allowed since the Majorana mass terms already present in Eq. (29) are supersymmetric.[11]

From this set of actions and Lagrangians, and after eliminating the auxiliary D^a fields through their equations of motion, the masses and mixings of the Higgs and gauge-adjoint scalar particles and their interactions can be read off, and correspondingly those of their superpartners as will be detailed below. The final form of the Lagrangians are collected in the following list which, in general, includes only interactions of the new fields.

1. $\text{SU(3)}_C\times\text{SU(2)}_I\times\text{U(1)}_Y$ gauge boson/sigma sector:

The gauge interactions of the adjoint sigma fields are determined from the scalar kinetic term $(D_\mu\sigma)^\dagger(D^\mu\sigma)$ with the covariant derivative $D_\mu = \partial_\mu + ig_sT^ag_\mu^a + igT^iW_\mu^i$. In addition to their kinetic terms, the term generates the Lagrangian for the derivative three-point and seagull four-point interaction terms:

$$
\mathcal{L}_{\sigma_C,gauge} = -g_sf^{abc}g_\mu^a\sigma_C^{b*}\overleftrightarrow{\partial^\mu}\sigma_C^c + g_s^2f^{ace}f^{bde}g_\mu^ag^{\mu b}\sigma_C^{*c}\sigma_C^d\,, \qquad (39)
$$

$$
\mathcal{L}_{\sigma_I,gauge} = -g\epsilon_{ijk}W_\mu^i\sigma_I^{j*}\overleftrightarrow{\partial^\mu}\sigma_I^k + g^2\epsilon_{ikm}\epsilon_{jlm}W_\mu^iW^{\mu j}\sigma_I^{*k}\sigma_I^l\,, \qquad (40)
$$

---

[11] Many of the mass parameters and couplings defining the $N = 1/N = 2$ hybrid model can be in general complex. Nevertheless, for the sake of discussion all the parameters are assumed to be real through this section.

where f^{abc} and ϵ_{ijk} are the $\mathrm{SU}(3)_C$ and $\mathrm{SU}(2)_I$ structure constants, respectively, and $A\overleftrightarrow{\partial_\mu}B \equiv A\partial_\mu B - (\partial_\mu A)B$.

2. $\mathbf{SU(3)}_C$ sfermion/gaugino/sigma sector:

The interaction Lagrangian of the sigma field σ_C with the squarks is given by

$$\mathcal{L}_{\sigma_C(\sigma_C)\tilde{q}\tilde{q}} = -\sqrt{2}\, g_s\, M_3^D\, (\sigma_C^a + \sigma_C^{a*}) \left(\tilde{q}_L^* \, \frac{\lambda^a}{2}\, \tilde{q}_L - \tilde{q}_R^* \, \frac{\lambda^a}{2}\, \tilde{q}_R \right) + i\, g_s^2\, f^{abc}\, \sigma_C^{a*} \sigma_C^b \tilde{q}^\dagger \frac{\lambda^c}{2}\, \tilde{q}\,, \tag{41}$$

where λ^a $(a = 1, ..., 8)$ are the Gell-Mann matrices. Therefore, the L- and R-chiral squarks contribute with opposite signs as demanded by the general form of the super-QCD D-terms. On the other hand, the interactions of the two gluino fields, $\tilde{g}$ and $\tilde{g}'$, with the $\mathrm{SU}(3)_C$ sigma field σ_C and to the squark and quark fields are described by the interaction Lagrangians:

$$\mathcal{L}_{\tilde{g}\tilde{g}'\sigma_C} = -\sqrt{2}\, i\, g_s\, f^{abc}\, \overline{\tilde{g}'^a_L}\, \tilde{g}^b_R\, \sigma^c_C + \text{h.c.}\,, \tag{42}$$

$$\mathcal{L}_{\tilde{g}q\tilde{q}} = -\sqrt{2}\, g_s \left(\overline{q_L}\, \frac{\lambda^a}{2}\, \tilde{g}^a_R\, \tilde{q}_L - \overline{q_R}\, \frac{\lambda^a}{2}\, \tilde{g}^a_L\, \tilde{q}_R \right) + \text{h.c.}\,, \tag{43}$$

where f^{abc} are the $\mathrm{SU}(3)_C$ structure constants. Note that only the standard gluino couples to squark fields since, as required by $N = 2$ supersymmetry, the new gluino $\tilde{g}'$ couples only to mirror matter fields, which in the hybrid model are assumed to be very heavy.

3. $\mathbf{SU(2)}_I\times\mathbf{U(1)}_Y$ sfermion/gaugino/sigma sector:

In the weak basis, the R-chiral sfermions $\tilde{f}_R$ are $\mathrm{SU}(2)_I$ singlets so that only the L-chiral sfermions $\tilde{f}_L$ interact with the $\mathrm{SU}(2)_I$ sigma field σ_I through the interaction Lagrangians:

$$\mathcal{L}_{\sigma_I(\sigma_I)\tilde{f}\tilde{f}} = -\sqrt{2}\, g\; M_I^D\, (\sigma_I^i + \sigma_I^{i*})\; \tilde{f}_L^\dagger\, \frac{\tau^i}{2}\, \tilde{f}_L + i g^2\, \epsilon_{ijk}\, \sigma_I^{j*} \sigma_I^k\; \tilde{f}_L^\dagger\, \frac{\tau^i}{2}\, \tilde{f}_L\,, \tag{44}$$

where $\tilde{f}_L$ is any matter $\mathrm{SU}(2)_I$-doublet field. On the other hand, the Lagrangians governing the interactions of the winos, $\tilde{W}$ and $\tilde{W}'$, with the $\mathrm{SU}(2)_I$ sigma field σ_I and the (s)fermion fields are given by

$$\mathcal{L}_{\sigma_I\tilde{W}\tilde{W}'} = -\sqrt{2}\, i\, g\, \epsilon^{ijk}\, \overline{\tilde{W}'^i_L}\, \tilde{W}^j_R\, \sigma^k_I + \text{h.c.}\,, \tag{45}$$

$$\mathcal{L}_{\tilde{W}f\tilde{f}} = -\sqrt{2}\, g\, \overline{f_L}\, \frac{\tau^i}{2}\, \tilde{W}^a_R\, \tilde{f}_L + \text{h.c.}\,. \tag{46}$$

Only the L-chiral sfermions $\tilde{f}_L$ couple to the standard wino $\tilde{W}$.

The $\mathrm{U}(1)_Y$ sigma field σ_Y is essentially a SM singlet state with no tree–level gauge interaction to any of the gauge bosons, gauginos and higgsinos. The singlet scalar field couples only to the Higgs bosons and the (s)fermion fields, with the latter being given by the Lagrangian:

$$\mathcal{L}_{\sigma_Y\tilde{f}\tilde{f}} = -\sqrt{2}\, g'\, M_Y^D (\sigma_Y^0 + \sigma_Y^{0*})\; (Y_{f_L} |\tilde{f}_L|^2 - Y_{f_R} |\tilde{f}_R|^2)\,, \tag{47}$$

and the standard bino $\tilde{B}$ (but not the new bino $\tilde{B}'$) couples to the (s)fermion fields through the interaction Lagrangian:

$$\mathcal{L}_{\tilde{B}f\tilde{f}} = -\sqrt{2}g'\,(Y_{f_L}\overline{f_L}\tilde{B}_R\tilde{f}_L - Y_{f_R}\overline{f_R}\tilde{B}_L\tilde{f}_R) + \text{h.c.}\,, \tag{48}$$

where Y_{f_L} and Y_{f_R} are the hypercharges of the L-chiral and R-chiral fermions, f_L and f_R, respectively.

4. SU(2)$_I$×U(1)$_Y$ higgsino/sigma sector:
The superpotential (34) coupling the new SU(2)$_I$×U(1)$_Y$ chiral superfields with the Higgs hypermultiplets leads to the Yukawa-type interactions of the electroweak sigma fields with the higgsino fields. In the weak basis, the interactions are described by the Lagrangian

$$\begin{aligned}\mathcal{L}_{\sigma\tilde{H}\tilde{H}} &= -\lambda_Y\sigma^0_Y(\overline{\tilde{H}^+_{uR}}\tilde{H}^-_{dL} - \overline{\tilde{H}^0_{uR}}\tilde{H}^0_{dL}) + \lambda_I\sigma^0_I(\overline{\tilde{H}^+_{uR}}\tilde{H}^-_{dL} + \overline{\tilde{H}^0_{uR}}\tilde{H}^0_{dL}) + \text{h.c.} \\ &\quad -\sqrt{2}\lambda_I\,(\sigma^-_1\overline{\tilde{H}^+_{uR}}\tilde{H}^0_{dL} - \sigma^+_2\overline{\tilde{H}^0_{uR}}\tilde{H}^-_{dL}) + \text{h.c.}\,, \end{aligned} \tag{49}$$

where we have introduced two charged scalars and one neutral scalar defined as

$$\sigma^-_1 = \frac{1}{\sqrt{2}}\left(\sigma^1_I + i\sigma^2_I\right)\,, \quad \sigma^+_2 = \frac{1}{\sqrt{2}}\left(\sigma^1_I - i\sigma^2_I\right)\,; \quad \sigma^0_I = \sigma^3_I\,. \tag{50}$$

Here, it is noteworthy that the σ fields are complex.

Combining the above Lagrangian (49) with the Lagrangian (45) for the interactions of the sigma fields with gauginos enables us to derive the vertices for the interactions of the sigma fields with charginos and neutralinos in the mass eigenstate basis.

5. SU(2)$_I$×U(1)$_Y$ Higgs/sigma sector :
The potential for the neutral and charged electroweak Higgs and scalar fields receives contributions from three different sources: The gauge kinetic terms, the superpotential, and the soft-breaking terms. The potential $V_{\sigma H}$ for the charged and neutral electroweak

Higgs and adjoint scalars can be written as a sum over four characteristic contributions:

$$\begin{aligned}
V_{\sigma H|1} &= m^2_{H_u}(|H_u^+|^2+|H_u^0|^2)+m^2_{H_d}(|H_d^0|^2+|H_d^-|^2)+[B_\mu(H_u^+H_d^- - H_u^0H_d^0)+\text{h.c.}]\,, &(51)\\
V_{\sigma H|2} &= \frac{1}{2}[\sqrt{2}M_Y^D(\sigma_Y^0+\sigma_Y^{0*})+\frac{1}{2}g'(|H_u^+|^2-|H_d^-|^2+|H_u^0|^2-|H_d^0|^2)]^2\\
&+ \frac{1}{2}|2M_I^D(\sigma_1^+ + \sigma_2^+)+\sqrt{2}g(\sigma_1^+\sigma_I^0-\sigma_2^+\sigma_I^{0*})+g(H_u^+H_u^{0*}+H_d^0H_d^+)|^2\\
&+ \frac{1}{2}[\sqrt{2}M_I^D(\sigma_I^0+\sigma_I^{0*})+g(|\sigma_2^+|^2-|\sigma_1^-|^2)+\frac{1}{2}g(|H_u^+|^2-|H_d^-|^2-|H_u^0|^2+|H_d^0|^2)]^2\,, &(52)\\
V_{\sigma H|3} &= |(\mu+\lambda_Y\sigma_Y^0-\lambda_I\sigma_I^0)H_d^-+\sqrt{2}\lambda_I\sigma_1^-H_d^0|^2+|(\mu+\lambda_Y\sigma_Y^0-\lambda_I\sigma_I^0)H_u^+-\sqrt{2}\lambda_I\sigma_2^+H_u^0|^2\\
&+ |(\mu+\lambda_Y\sigma_Y^0+\lambda_I\sigma_I^0)H_d^0+\sqrt{2}\lambda_I\sigma_2^+H_d^-|^2+|(\mu+\lambda_Y\sigma_Y^0+\lambda_I\sigma_I^0)H_u^0-\sqrt{2}\lambda_I\sigma_1^-H_u^+|^2\\
&+ |M_Y\sigma_Y^0+\lambda_Y(H_u^+H_d^- - H_u^0H_d^0)|^2+|M_I\sigma_I^0-\lambda_I(H_u^+H_d^- + H_u^0H_d^0)|^2\\
&+ |M_I\sigma_1^- - \sqrt{2}\lambda_I H_u^0H_d^-|^2+|M_I\sigma_2^+ + \sqrt{2}\lambda_I H_u^+H_d^0|^2\,, &(53)\\
V_{\sigma H|4} &= m_Y^2|\sigma_Y^0|^2+m_I^2(|\sigma_I^0|^2+|\sigma_1^-|^2+|\sigma_2^+|^2)+\frac{1}{2}(m_Y'^2\sigma_Y^{02}+\text{h.c.})+\frac{1}{2}[m_I'^2(\sigma_I^{02}+2\sigma_2^+\sigma_1^-)+\text{h.c.}]\\
&+ A_Y\lambda_Y\sigma_Y^0(H_u^+H_d^- - H_u^0H_d^0)-A_I\lambda_I\,\sigma_I^0(H_u^+H_d^- + H_u^0H_d^0)+\text{h.c.}\\
&+ \sqrt{2}A_I\lambda_I(\sigma_1^-H_u^+H_d^0-\sigma_2^+H_d^-H_u^0)+\text{h.c.} &(54)
\end{aligned}$$

After shifting the neutral fields by their vacuum expectation values, the physical scalar masses and the tri- and quattro-linear interaction vertices can be read off.

2.4.2 QCD Sector: Color-Octet Scalar

In this subsection, we study the phenomenology in the $SU(3)_C$ sector, in particular, the production and decay of the color-octet scalar, σ_C. We use σ for the σ_C in this subsection, in order to avoid too many subscripts.

For simplicity, we will set $m_C'^2 = 0$ in Eq. (36), so that the physical mass of the complex scalar octet is

$$M_\sigma = \sqrt{|M_3'|^2 + m_C^2}\,. \tag{55}$$

For given mean mass, a nonzero ${m_C'}^2$ generating a mass splitting of the scalar fields would increase the total cross section for the production of the new scalars.

In the simplest realization the two gluinos, $\tilde{g}$ and $\tilde{g}'$, are not endowed with individual masses (i.e. $M_3' = 0$) but they are coupled by the mass parameter M_3^D in a purely off-diagonal mass matrix.[12] In this configuration the two Majorana gluinos can be combined to a 4-component Dirac gluino field $\tilde{g}_D$ as

$$\tilde{g}_D = \tilde{g}_R + \tilde{g}'_L\,, \tag{56}$$

---

[12] Note that this Dirac mass term must be nonzero, since otherwise the lightest member of the superfield $\hat{g}'$ would be stable. In contrast, scenarios where the diagonal Majorana entries of the gluino mass matrix vanish are perfectly acceptable.

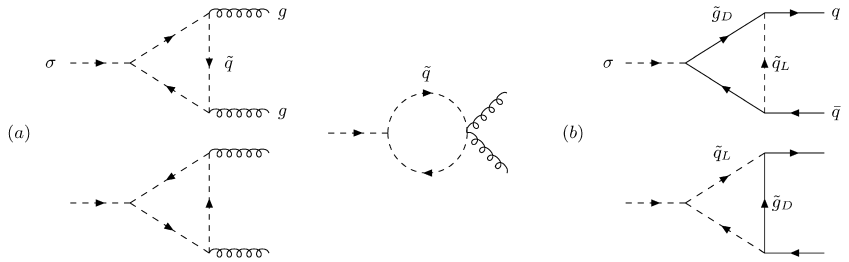

Figure 9: Diagrams for (a) the effective σgg vertex built up by squark loops; (b) the effective $\sigma q\bar q$ vertex with L squarks and gluinos – the coupling to R squarks being mediated by the charge-conjugate Dirac gluinos.

with the mass eigenvalue given by $|M_3^D|$, cf. [48]. The couplings of this Dirac field $\tilde g_D$ to the σ-field and to the squark and quark fields are summarized in the interaction Lagrangians

$$\mathcal{L}_{\tilde g_D \tilde g_D \sigma} = -\sqrt{2} i \, g_s \, f^{abc} \, \overline{\tilde g^a_{DL}} \, \tilde g^b_{DR} \, \sigma^c + \text{h.c.}\,, \tag{57}$$

$$\mathcal{L}_{\tilde g_D q \tilde q} = -\sqrt{2} \, g_s \sum_q \left(\overline{q_L} \frac{\lambda^a}{2} \tilde g^a_{DR} \, \tilde q_L + \overline{q_R} \frac{\lambda^{aT}}{2} \tilde g^{aC}_{DL} \, \tilde q_R \right) + \text{h.c}\,. \tag{58}$$

where $\tilde g_D^{CT} = -(\tilde g'_R + \tilde g_L)$ is the charge-conjugate 4-component Dirac gluino [48], f^{abc} are the SU(3)$_C$ structure constants and λ^a are the Gell-Mann matrices. In addition, the sgluon fields couple to gluons in tri-and quattro-linear vertices as prescribed by gauge theories for scalar octet fields, i.e. proportional to the octet self-adjoint SU(3)$_C$ representation F. As a result, at tree level σ pairs can be produced in gluon collisions as well as in $q\bar q$ annihilation, but single production of σ's is not possible.

Even at the one-loop level, gluino loops do not contribute to the σgg coupling, due to the Bose symmetry of the gluons. The coupling is even in the 4-momenta under gluon exchange but it is odd, on the other hand, due to the antisymmetric octet matrix elements f^{abc} in color space. (Note that SU(3)$_C$ singlet particles, like Higgs bosons, couple symmetrically to gluons, by contrast.) Actually, the coupling of the octet sgluon to any number of gluons is forbidden in the general softly broken N=2 pure gauge theory with two Majorana gluinos (which may or may not be combined to a single Dirac gluino) because the totally antisymmetric factor f^{abc} forces the sgluon to couple only to two *different* Majorana gluinos, while gluons always couple to *diagonal* Majorana gluino pairs.

However, σ can couple non-trivially to gluon pairs and quark-antiquark pairs through triangle diagrams involving squark lines. Characteristic examples are depicted in Fig. 9. In parallel to the interaction Lagrangian it turns out that all L- and R-squark contributions to the couplings come with opposite signs so that they cancel each other for mass degenerate squarks. In addition, the quark-antiquark coupling is suppressed by the quark

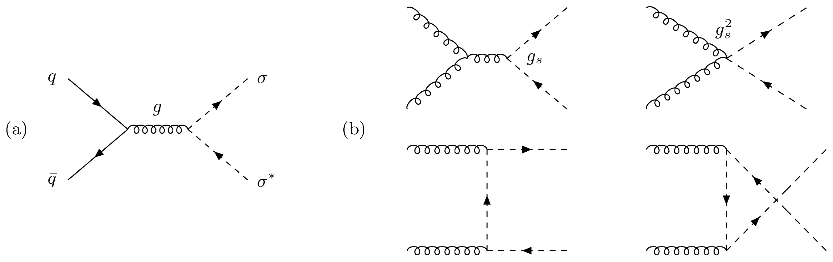

Figure 10: Feynman diagrams for sigma-pair production in quark annihilation (a) and gluon fusion (b).

mass as evident from general chirality rules.

1. σ Production

As mentioned in the beginning of this subsection, the phenomenological analysis will be carried out for a complex color-octet σ fields without mass splitting between the real and imaginary components.

Pair production

The Feynman diagrams for the two parton processes $gg, q\bar{q} \to \sigma\sigma^*$ are displayed in Fig. 10. They are identical (*modulo* color factors) to squark-pair production [49, 50] if initial and final-state flavors are different.

The total cross sections for the two $\sigma\sigma^*$ parton processes are easy to calculate:

$$\sigma[q\bar{q} \to \sigma\sigma^*] = \frac{4\pi\alpha_s^2}{9s}\,\beta_\sigma^3\,, \tag{59}$$

$$\sigma[gg \to \sigma\sigma^*] = \frac{15\pi\alpha_s^2\beta_\sigma}{8s}\left[1 + \frac{34}{5}\frac{M_\sigma^2}{s} - \frac{24}{5}\left(1 - \frac{M_\sigma^2}{s}\right)\frac{M_\sigma^2}{s}\frac{1}{\beta_\sigma}\log\left(\frac{1+\beta_\sigma}{1-\beta_\sigma}\right)\right] \tag{60}$$

The standard notation has been adopted for the parameters: $\sqrt{s}$ is the invariant parton-parton energy, and M_σ and $\beta_\sigma = (1 - 4M_\sigma^2/s)^{1/2}$ the mass and center-of-mass velocity of the σ particle. The QCD coupling is inserted to leading order, $\alpha_s(Q^2) = \alpha_s^{(5)}(Q^2)[1 + \alpha_s^{(5)}(Q^2)/(6\pi) \cdot \log M_t^2/Q^2]^{-1}$, where $\alpha_s^{(5)}(Q^2)$ evolves from $\alpha_s^{(5)}(M_Z^2) \simeq 0.120$ with $N_F = 5$ flavors by definition, while the top-quark threshold is accounted for explicitly and supersymmetric particles do not affect the running in practice; the renormalization scale for the parton subprocesses is set to $Q = M_\sigma$.

While the quark-annihilation cross section increases near threshold with the third power β_σ^3 of the sgluon velocity, as characteristic for P-wave production, the cross section for equal-helicity gluon-fusion increases steeply $\sim \beta_\sigma$ with the velocity, as predicted for S-waves by the available phase space. Asymptotically the two parton cross sections scale $\propto s^{-1}$.

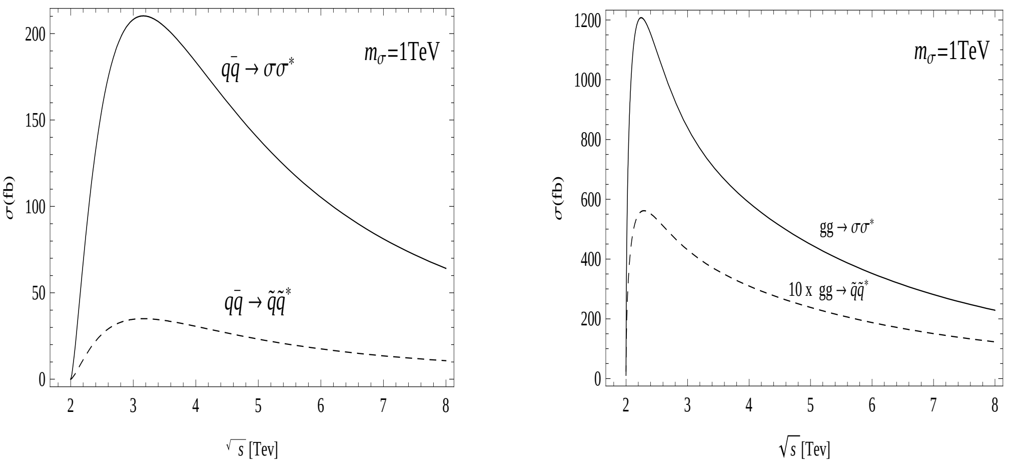

Figure 11: Parton cross sections for $\sigma\sigma^*$ production in the $q\bar{q}$ (left) and gg (right) channel. For comparison, the production of 3rd generation squark pairs is shown by the dotted lines for the same masses.

The $\sigma\sigma^*$ cross sections are compared in Fig. 11 with the production of squark pairs (of the 3rd generation to match the dynamical production mechanisms): $gg, q\bar{q} \to \tilde{q}_3\tilde{q}_3^*$. As expected, the $\sigma\sigma^*$ cross sections exceed the $\tilde{q}_3\tilde{q}_3^*$ cross sections by a large factor, i.e. ~ 20 for gg collisions and 6 for $q\bar{q}$ collisions. This can be exemplified by considering the evolution of ratios for the cross sections from small to maximum velocity, β being again the center-of-mass velocity of the sgluon or squark in the final state:

$$\frac{\sigma\left[gg \to \sigma\sigma^*\right]}{\sigma\left[gg \to \tilde{q}_3\tilde{q}_3^*\right]} = \begin{cases} \dfrac{tr\left[\{F^a, F^b\}\{F^a, F^b\}\right]}{tr\left[\left\{\frac{\lambda_a}{2}, \frac{\lambda_b}{2}\right\}\left\{\frac{\lambda_a}{2}, \frac{\lambda_b}{2}\right\}\right]} = \dfrac{216}{28/3} \simeq 23 & \text{for } \beta \to 0\,, \\[2ex] \dfrac{tr\left(2F^aF^bF^bF^a + F^aF^bF^aF^b\right)}{tr\left(2\frac{\lambda^a}{2}\frac{\lambda^b}{2}\frac{\lambda^b}{2}\frac{\lambda^a}{2} + \frac{\lambda^a}{2}\frac{\lambda^b}{2}\frac{\lambda^a}{2}\frac{\lambda^b}{2}\right)} = \dfrac{180}{10} = 18 & \text{for } \beta \to 1\,, \end{cases} \tag{61}$$

$$\frac{\sigma\left[q\bar{q} \to \sigma\sigma^*\right]}{\sigma\left[q\bar{q} \to \tilde{q}_3\tilde{q}_3^*\right]} = \frac{tr\left(\frac{\lambda^a}{2}\frac{\lambda^b}{2}\right)\, tr\left(F^aF^b\right)}{tr\left(\frac{\lambda^a}{2}\frac{\lambda^b}{2}\right)\, tr\left(\frac{\lambda^a}{2}\frac{\lambda^b}{2}\right)} = \frac{12}{2} = 6 \quad \text{for any } \beta\,. \tag{62}$$

The ratio (61) decreases monotonically as β increases but by no more than 20%. Most important is the ratio at the maximum of the gg cross sections where it is still close the initial maximal value; this can easily be explained by observing that, in Feynman gauge, the leading contribution is generated by the quartic coupling. The differences in the color factors reflect the different strengths of the couplings in the fractional triplet $\lambda/2$ and the integer octet F couplings of $\mathrm{SU}(3)_C$ with $(F^a)_{bc} = -if^{abc}$. The cross sections are shown in Fig. 11 for $M_\sigma = 1\mathrm{TeV}$ across the invariant energy range relevant for the LHC. The values of the maxima in the gg and $q\bar{q}$ channels are about 1 pb and 0.2 pb, respectively, a typical size for such processes.

2. σ Decays

At tree level the σ particles can decay to a pair of Dirac gluinos $\tilde{g}_D$ or into a pair of squarks, with one or both of these sparticles being potentially virtual when $M_\sigma < 2M_{\tilde{g}_D}, 2m_{\tilde{q}}$. For on-shell decays and assuming pure Dirac gluinos the partial widths are

$$\begin{aligned} \Gamma[\sigma \to \tilde{g}_D \bar{\tilde{g}}_D] &= \frac{3\alpha_s M_\sigma}{4} \beta_{\tilde{g}} \, (1 + \beta_{\tilde{g}}^2) \, , \\ \Gamma[\sigma \to \tilde{q} \tilde{q}^*] &= \frac{\alpha_s}{4} \frac{|M_3^D|^2}{M_\sigma} \beta_{\tilde{q}} \, , \end{aligned} \tag{63}$$

where $\beta_{\tilde{g},\tilde{q}}$ are the velocities of $\tilde{g}, \tilde{q}$. In the presence of non–trivial $\tilde{q}_L$-$\tilde{q}_R$ mixing the subscripts L, R in the second Eq. (63) have to be replaced by $1, 2$ labeling the mass eigenstates, and the contribution from this flavor is suppressed by a factor $\cos^2(2\theta_{\tilde{q}})$; the mixing angle is defined via the decomposition of the lighter mass eigenstate $\tilde{q}_1 = \cos\theta_{\tilde{q}}\, \tilde{q}_L + \sin\theta_{\tilde{q}}\, \tilde{q}_R$. In addition, decays into $\tilde{q}_1 \tilde{q}_2^*$ and $\tilde{q}_1^* \tilde{q}_2$ are possible, with the coefficient $\sin^2(2\theta_{\tilde{q}})$ and with the velocity $\beta_{\tilde{q}}$ replaced by the phase-space function $\lambda^{1/2}(1, m_{\tilde{q}_1}^2/M_\sigma^2, m_{\tilde{q}_2}^2/M_\sigma^2)$. The gluinos subsequently decay to quarks and squarks, again either real or virtual, and the squarks to quarks and charginos/neutralinos tumbling eventually down to the LSP.

On the other hand, the trilinear interaction in Eq. (41) gives rise to an effective σgg coupling via squark loops, Fig. 9(a), leading to the partial decay width

$$\Gamma(\sigma \to gg) = \frac{5\alpha_s^3}{384\pi^2} \frac{|M_3^D|^2}{M_\sigma} \left| \sum_q \left[\tau_{\tilde{q}_L} f(\tau_{\tilde{q}_L}) - \tau_{\tilde{q}_R} f(\tau_{\tilde{q}_R}) \right] \right|^2 \, , \tag{64}$$

with $\tau_{\tilde{q}_{L,R}} = 4m_{\tilde{q}_{L,R}}^2 / M_\sigma^2$ and [51]

$$f(\tau) = \begin{cases} \left[\sin^{-1}\left(\frac{1}{\sqrt{\tau}} \right) \right]^2 & \text{for } \tau \geq 1 \, , \\ -\frac{1}{4} \left[\ln \frac{1+\sqrt{1-\tau}}{1-\sqrt{1-\tau}} - i\pi \right]^2 & \text{for } \tau < 1 \, . \end{cases} \tag{65}$$

In the presence of nontrivial $\tilde{q}_L$–$\tilde{q}_R$ mixing, the subscripts L, R in Eq. (64) again have to be replaced by $1, 2$ labeling the mass eigenstates, and the contribution from this flavor is suppressed by a factor $\cos(2\theta_{\tilde{q}})$ multiplying the term in square parentheses. Note that the σgg coupling vanishes in the limit of degenerate L and R squarks.

Furthermore, the σ field couples to quark-antiquark pairs – in principle. By standard helicity arguments, this chirality-flip coupling is suppressed however by the quark mass. For pure Dirac gluinos, the triangle diagrams, Fig. 9(b), either with two internal gluino lines and one squark line or with two internal squark lines and one gluino line again vanish for degenerate L and R squarks. The resulting partial width can be written as

$$\Gamma(\sigma \to q\bar{q}) = \frac{9\alpha_s^3}{128\pi^2} \frac{|M_3^D|^2 m_q^2}{M_\sigma} \, \beta_q \left[\left(M_\sigma^2 - 4m_q^2 \right) |\mathcal{I}_S|^2 + M_\sigma^2 \, |\mathcal{I}_P|^2 \right] \, . \tag{66}$$

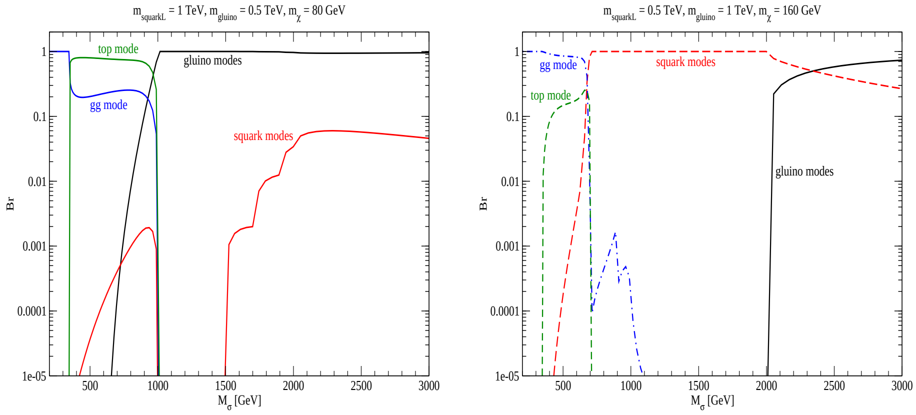

Figure 12: Branching ratios for σ decays, for $m_{\tilde{q}_L} = 2m_{\tilde{g}} = 1$TeV (Left) and $m_{\tilde{g}} = 2m_{\tilde{q}_L} = 1$TeV (Right). In both cases we assumed a neutralino mass $m_{\tilde{\chi}} = 0.16 m_{\tilde{g}}$, and moderate squark mass splitting: $m_{\tilde{q}_R} = 0.95 m_{\tilde{q}_L}$, $m_{\tilde{t}_L} = 0.9 m_{\tilde{q}_L}$, $m_{\tilde{t}_R} = 0.8 m_{\tilde{q}_L}$, with $\tilde{t}_L$-$\tilde{t}_R$ mixing determined by $X_t = m_{\tilde{q}_L}$.

The loop integrals for the effective scalar (S) and pseudoscalar (P) couplings are given by

$$\begin{aligned} \mathcal{I}_S &= \int_0^1 dx \int_0^{1-x} dy \left\{ (1-x-y) \left(\frac{1}{C_L} - \frac{1}{C_R} \right) + \frac{1}{9}(x+y) \left(\frac{1}{D_L} - \frac{1}{D_R} \right) \right\} , \\ \mathcal{I}_P &= \int_0^1 dx \int_0^{1-x} dy \left(\frac{1}{C_L} - \frac{1}{C_R} \right) , \end{aligned} \tag{67}$$

where we have defined ($a = L, R$)

$$\begin{aligned} C_a &= (x+y)|M_3^D|^2 + (1-x-y) m_{\tilde{q}_a}^2 - xy M_\sigma^2 - (x+y)(1-x-y) m_q^2 , \\ D_a &= (1-x-y)|M_3^D|^2 + (x+y) m_{\tilde{q}_a}^2 - xy M_\sigma^2 - (x+y)(1-x-y) m_q^2 . \end{aligned} \tag{68}$$

$\mathcal{I}_{S,P}$ can also be expressed in terms of standard Passarino-Veltman functions [52], e.g. $\mathcal{I}_P = C_{0L} - C_{0R}$, with $C_{0L,R} \equiv C_0(|M_3^D|, m_{\tilde{q}_{L,R}}, |M_3^D|; m_q^2, m_q^2, M_\sigma^2)$. In the presence of nontrivial $\tilde{q}_L$–$\tilde{q}_R$ mixing, the subscripts L, R in Eq. (67) have to be replaced by $1, 2$ labeling the squark mass eigenstates, and the contribution from this flavor to the double integrals is suppressed by a factor $\cos(2\theta_q)$. Note that $\mathcal{I}_S = \mathcal{I}_P = 0$ if $m_{\tilde{q}_L} = m_{\tilde{q}_R}$. In the presence of $\tilde{q}_L$-$\tilde{q}_R$ mixing this cancelation is no longer exact for two non-degenerate Majorana gluinos. The corresponding 2-body branching ratios are compared to those for tree–level decays in Fig. 12. Here we assume moderate mass splitting between the L and R squarks of the five light flavors, and somewhat greater for soft breaking $\tilde{t}$ masses: $m_{\tilde{q}_R} = 0.95 m_{\tilde{q}_L}$, $m_{\tilde{t}_L} = 0.9 m_{\tilde{q}_L}$, $m_{\tilde{t}_R} = 0.8 m_{\tilde{q}_L}$. We parameterize the off–diagonal element of the squared $\tilde{t}$ mass matrix as $X_t m_t$, and take $X_t = m_{\tilde{q}_L}$. We again assume the gluino to be a pure Dirac state, i.e. $m_{\tilde{g}} = |M_3^D|$.

Even for this small mass splitting, the loop decays into two gluons and, if kinematically allowed, a $t\bar{t}$ pair always dominate over tree–level four–body decays $\sigma \to \tilde{g}q\bar{q}\tilde{\chi}$ (which is part of the "gluino modes" in Fig. 12) and $\sigma \to q\bar{q}\tilde{\chi}\tilde{\chi}$ (which is part of the "squark modes"). For simplicity we evaluated these higher order tree-level decays for a photino LSP state, with mass $0.16m_{\tilde{g}}$. $\mathrm{SU}(2)_L$ gauginos have larger couplings to doublet squarks, but are also expected to be heavier. Including them in the final state would at best increase the partial widths for four–body final states by a factor of a few, which would still leave them well below the widths for the loop induced decays. On the other hand, the partial width for the tree–level three–body decays $\sigma \to \tilde{q}\bar{q}\tilde{\chi},\ \tilde{q}^* q\tilde{\chi}$ can be comparable to that for the loop–induced decays if M_σ is not too much smaller than $2m_{\tilde{q}}$.

Figure 12 also shows that the ordering between the two loop-induced decay modes for $M_\sigma > 2m_t$ depends on the values of various soft breaking parameters. Increasing the gluino mass increases the $\sigma\tilde{q}\tilde{q}^*$ coupling and hence the partial width into two gluons which is due to pure squark loops. On the other hand, the $t\bar{t}$ partial width, which is due to mixed squark–gluino loops, decreases rapidly with increasing gluino mass. The increase of the $\sigma\tilde{q}\tilde{q}$ couplings is over–compensated by the gluino mass dependence of the propagators. For $|M_3^D| > m_{\tilde{q}}$ the loop functions $\mathcal{I}_{S,P}$ are additionally suppressed since then $C_L \simeq C_R,\ D_L \simeq D_R$ up to corrections of $\mathcal{O}(m_{\tilde{q}}^2/|M_3^D|^2)$. (A similar cancelation also occurs for $M_\sigma^2 \gg m_{\tilde{q}}^2$, for both the σgg and $\sigma t\bar{t}$ couplings.) In total, the $t\bar{t}$ final state will dominate for small gluino mass and the gg final state for large gluino mass. Moreover, as noted earlier, the partial width into both gluons and quarks vanishes for exact degeneracy between L and R squarks.

Not surprisingly, the two–body final states of Eq. (63) that are accessible at tree level will dominate if they are kinematically allowed. Note that well above all thresholds the partial width into gluinos always dominates, since it grows $\propto M_\sigma$ while the partial width into squarks asymptotically scales like $1/M_\sigma$. This is a result of the fact that the supersymmetry breaking $\sigma\tilde{q}\tilde{q}^*$ coupling has mass dimension 1, while the supersymmetric $\sigma\tilde{g}\bar{\tilde{g}}$ coupling is dimensionless.

3. Signatures at the LHC

Pair production and decays at the LHC

The cross section for σ-pair production at LHC, $pp \to \sigma\sigma^*$, is shown by the solid red curve in Fig. 13 for the σ-mass range between 500 GeV and 2TeV (adopting the LO CTEQ6L parton densities [53]). The cross section exceeds stop or sbottom-pair production (red dashed line), mediated by a set of topologically equivalent Feynman diagrams, by more than an order of magnitude, as anticipated at the parton level. With values from several picobarn downwards, a sizable $\sigma\sigma^*$ event rate can be generated.

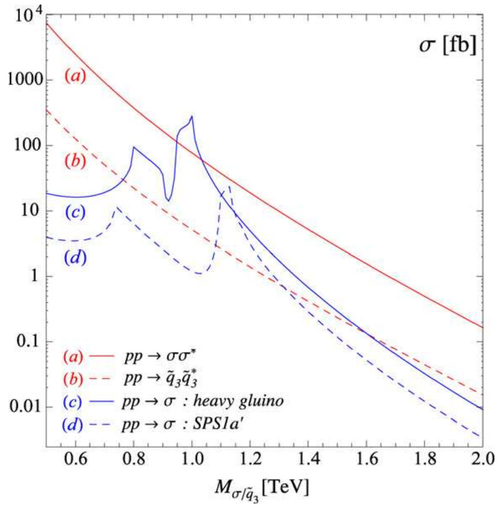

Figure 13: Cross sections for σ-pair (and $\tilde q_3$-pair) production (red lines), as well as for single σ production (blue lines), at the LHC. In the latter case the solid blue curve has been obtained using the same mass parameters as in Fig. 12 (Right), while the dashed blue curve adopts the mSUGRA benchmark point SPS1a′.

With the exception of $\sigma \to gg$ decays, all the modes shown in Fig. 12 give rise to signatures that should be easily detectable if σ is not too heavy. The most spectacular signature results from $\sigma \to \tilde g \tilde g$ decay, each σ decaying into at least four hard jets and two invisible neutralinos as LSP's. σ-pair production then generates final states with a minimum of eight jets and four LSP's.

The transverse momenta of the hard jets produced in the simplest case $\tilde\chi = \tilde\chi^0_1$ can easily be estimated by analyzing productions and decays near the mass thresholds, i.e. $M_\sigma \simeq 2m_{\tilde g} \simeq 2m_{\tilde q} \gg m_{\tilde\chi^0_1}$. In this kinematic configuration the total jet transverse energy and the average jet transverse energy amount to

$$\sigma\sigma^* \;\;:\;\; \langle E^{tot}_{\perp j}\rangle \sim 2m_{\tilde q} \quad \text{and} \quad \langle E_{\perp j}\rangle \sim m_{\tilde q}/4\,. \tag{69}$$

The total transverse energy E_T carried by the LSPs and the vector sum of the momenta of the four χ^0_1 in the final state, which determines the measured missing transverse momentum p_T, are predicted to be

$$\sigma\sigma^* \;\;:\;\; \langle E^{tot}_{\perp\chi}\rangle \sim 2m_{\tilde q} \quad \text{and} \quad \langle p_{\perp\chi}\rangle \sim m_{\tilde q} \tag{70}$$

in the random-walk approximation for the χ momenta in the transverse plane. This is to be contrasted to gluino-pair production near threshold, where the corresponding observables are for the same mass configuration:

$$\tilde g\tilde g \;\;:\;\; \langle E^{tot}_{\perp j}\rangle \sim m_{\tilde q} \quad \text{and} \quad \langle E_{\perp j}\rangle \sim m_{\tilde q}/4\,, \tag{71}$$

$$\langle E^{tot}_{\perp\chi}\rangle \sim m_{\tilde q} \quad \text{and} \quad \langle p_{\perp\chi}\rangle \sim m_{\tilde q}/\sqrt{2}\,. \tag{72}$$

Thus, the total jet transverse energies and the missing transverse momenta are markedly different in the $N = 1$ and $N = 2$ theories for the same mass configurations.

$M_{\sigma/\tilde{g}}$		2σ		$2\tilde{g}$		2σ	$2\tilde{g}$
		$\langle E_{\perp j}^{tot} \rangle$	$\langle E_{\perp j} \rangle$	$\langle E_{\perp j}^{tot} \rangle$	$\langle E_{\perp j} \rangle$	$\langle p_{\perp \chi} \rangle$	$\langle p_{\perp \chi} \rangle$
1.50 TeV	[tot]	1.67	0.21	1.67	0.42	0.45	0.65
	[high]		0.27		0.53		
	[low]		0.15		0.31		
0.75 TeV	[tot]	0.91	0.11	0.93	0.23	0.22	0.31
	[high]		0.14		0.29		
	[low]		0.08		0.17		
$M_\sigma = 2\,M_{\tilde{g}} = 8/3\,M_{\tilde{q}} = 15\,M_\chi$							

Table 7: Transverse jet energies and vector sum of the LSP transverse momenta for final states in 2σ and $2\tilde{g}$ production, with primary $\sigma/\tilde{g}$-masses of 1.5 and 0.75TeV; the mass hierarchy in the cascade decays is noted in the bottom line. Below the transverse energy per jet of the total jet ensemble [tot], the transverse energies in the high and the low jet-energy groups [high/low] are displayed. All units in TeV.

These simple estimates are backed up by a Monte-Carlo simulation of σ-pair production at the LHC, followed by the decay into four on–shell gluinos. The total transverse jet energy and the vector sum of the LSP transverse momenta are summarized in Tab. 2.4.2 for a spectrum of σ-masses, and fixed ratios of gluino, squark and LSP neutralino masses. The squark and gluino masses are again chosen at about half a TeV. The values of the transverse momenta match the earlier estimates quite well. It should be noted however that the jet transverse momenta fall into two groups. The transverse momenta of jets in gluino to squark decays are generally small while the transverse momenta of the jets generated in squark decays are large. Both groups are populated equally so that the average transverse momenta of the jets are reduced by an approximate factor two compared with the MSSM gluino pair production (setting $m_{\tilde{g}}|_{\rm MSSM} = M_\sigma|_{\rm hybrid\ model}$ for the proper comparison).

Other interesting final states resulting from σ-pair production are four-top states $\tilde{t}_1\tilde{t}_1\tilde{t}_1^*\tilde{t}_1^*$, which can be the dominant mode if $m_{\tilde{q}} \lesssim m_{\tilde{g}}$ and L-R mixing is significant in the stop sector, and $\tilde{q}\tilde{q}^*\tilde{g}\tilde{g}$, which can be a prominent mode if $M_\sigma > 2m_{\tilde{g}} \gtrsim 2m_{\tilde{q}}$. These channels also lead to four LSPs in the final state, plus a large number of hard jets. On the other hand, the $tt\bar{t}\bar{t}$ final state, which can be the dominant mode if the two–body decays into squarks and gluinos are kinematically excluded, might allow the direct kinematic reconstruction of M_σ.

Single σ Channel

As noted earlier, sgluons can be generated singly in gluon-gluon collisions via squark loops. The partonic cross section, with the Breit-Wigner function factorized off, is given by

$$\hat{\sigma}[gg \to \sigma] = \frac{\pi^2}{M_\sigma^3}\Gamma(\sigma \to gg)\,, \tag{73}$$

where the partial width for $\sigma \to gg$ decays has been given in Eq. (64).

The resulting cross section for single σ production at the LHC is shown by the blue curves in Fig. 13 (based on the LO CTEQ6L parton densities [53]). The solid curve has been calculated for the parameter set of the right frame of Fig. 12, while the dashed curve has been determined by taking the soft breaking parameters in the gluino and squark sector from the widely used benchmark point SPS1a′ [54]. In the former case the single σ cross section can exceed the σ-pair production cross section for $M_\sigma \sim 1$TeV. Since SPS1a′ has a somewhat smaller gluino mass (which we again interpret as a Dirac mass here) it generally leads to smaller cross sections for single σ production. Taking $m_{\tilde{q}} \simeq 2|M_3^D|$, as in the left frame of Fig. 12, would lead to a very small single σ production cross section. Recall that $m_{\tilde{q}} > |M_3^D|$ is required if $\sigma \to t\bar{t}$ decays are to dominate. We thus conclude that one cannot simultaneously have a large $\sigma(pp \to \sigma)$ and a large $\mathrm{Br}(\sigma \to t\bar{t})$.

The signatures for single σ production, which is an $\mathcal{O}(\alpha_s^3)$ process, are potentially exciting as well. However, since all final states resulting from σ decay can also be produced directly in tree-level $\mathcal{O}(\alpha_s^2)$ processes at the LHC, it is a problem to be solved by experimental simulations whether single σ production is detectable as a resonance above the SM plus MSSM backgrounds, given that in most cases, with the exception of the 2-gluon channel, the direct kinematic reconstruction of M_σ is not possible.

2.4.3 Electroweak Sector

In this subsection, we analyze the electroweak sector, which includes the Dirac neutralinos and the electroweak scalar bosons.

Introducing the vacuum expectation values of the scalar/Higgs fields in the Lagrangians of the Sec. 2.4.1, their values are determined by the absence of terms linear in the fields, while from the terms bilinear in the fields the mass matrices for the scalars/Higgs, the charginos and neutralinos can be read off. The vacuum expectation values (vevs) of the neutral Higgs and the sigma fields are defined as

$$\langle H_{u/d}^0 \rangle = \frac{1}{\sqrt{2}}\, v_{u/d}\,, \tag{74}$$

$$\langle \sigma_{Y/I}^0 \rangle = \frac{1}{\sqrt{2}} v_{Y/I}\,. \tag{75}$$

As usual, the vevs of the Higgs sector can be rewritten as

$$v = \sqrt{v_u^2 + v_d^2} \quad \text{and} \quad \tan\beta = \frac{v_u}{v_d}\,. \tag{76}$$

The masses of the electroweak vector bosons W, Z are generated by the interactions of the fields with the ground states of the neutral Higgs H_u, H_d and the scalar iso-triplet field σ_I (the hypercharge-neutral field σ_Y does not couple)

$$m_Z^2 = \frac{1}{4}(g'^2 + g^2)v^2\,, \qquad m_W^2 = \frac{1}{4}g^2v^2 + g^2v_I^2\,. \tag{77}$$

The iso-triplet vev shifts the tree-level ρ-parameter away from unity by the amount

$$\Delta\rho = \rho - 1 = 4v_I^2/v^2 \tag{78}$$

Allowing a maximum value $\Delta\rho \leq 10^{-3}$ for the shift, it turns out that the vacuum expectation value must be very small, $v_I \leq 3\,\mathrm{GeV}$. We will assume that the soft supersymmetry breaking scalar σ_I mass parameter m_I of order TeV drives v_I to a small value. As a result, the Higgs value v is close to the standard value $v = 246\,\mathrm{GeV}$, and $\tan\beta$ may be identified approximately with the corresponding MSSM parameter. And while almost any value for v_Y is phenomenologically quite consistent, a large m_Y would typically drive v_Y to relatively smaller values.

1. Charginos and Neutralinos

Masses and mixing

1) Charginos

Defining the current basis $\{\tilde{W}'^-, \tilde{W}^-, \tilde{H}_d^-\}$ for the two charged winos and the higgsino, the chargino mass matrix can be written as

$$\mathcal{M}_C = \begin{pmatrix} M_2' & M_2^D - gv_I & -\lambda_I v_u \\ M_2^D + gv_I & M_2 & \frac{1}{\sqrt{2}}gv_d \\ \lambda_I v_d & \frac{1}{\sqrt{2}}gv_u & \mu_c \end{pmatrix}\,, \tag{79}$$

where

$$M_2 = M_{\tilde{W}}, \quad M_2' = M_{\tilde{W}}' + M_I, \quad M_2^D = M_I^D \quad \text{and} \quad \mu_c = \mu + (\lambda_Y v_Y - \lambda_I v_I)/\sqrt{2}\,. \tag{80}$$

Three charginos, i.e. one degree of freedom more than in MSSM and related iso-singlet extensions like Next-to-minimal supersymmetric Standard Model or U(1)-extended supersymmetric Standard Model, are predicted in the general $N = 1/N = 2$ hybrid model, labeled $\tilde{\chi}_1^\pm, \tilde{\chi}_2^\pm, \tilde{\chi}_3^\pm$ (ultimately for ascending mass values). The MSSM case is reached in the limit $M_2' \to -\infty$ which corresponds to infinitely heavy $\tilde{W}'$. By raising the magnitude of the $\tilde{W}'$ gaugino mass parameter M_2' from $-\infty$ to 0 and lowering at the same time M_2 to 0 the Dirac limit is obtained. Although the 3×3 mass matrix can be diagonalized analytically for arbitrary parameters, we study instead the evolution of the eigenvalues numerically by varying $-\infty \leq M_2' \leq 0$ from MSSM to the Dirac limit below.

Note that for small gaugino/higgsino mixings in the area where the supersymmetry mass parameters M_2', M_2, M_I^D, μ (and the size of their mutual differences) are much larger than the electroweak parameter v and the vevs of the sigma fields (v_Y and v_I), the eigenvalues and mixing parameters can be calculated analytically. This approximation leaves us with one higgsino mass eigenvalue

$$\overline{m}_3^{\pm} \approx \mu \,, \tag{81}$$

and a 2×2 gaugino mass submatrix with two eigenvalues

$$\overline{m}_{1,2}^{\pm} \approx \frac{1}{2}\left|\, |M_2' + M_2| \mp \delta_2 \,\right| \quad \text{where} \quad \delta_2 = \sqrt{(M_2' - M_2)^2 + 4(M_2^D)^2}\,, \tag{82}$$

and the mixing angle

$$\cos\theta_2/\sin\theta_2 = \sqrt{\frac{1 \pm (M_2' - M_2)/\delta_2}{2}}\,, \tag{83}$$

under the assumption that $M_2' + M_2 \leq 0$ and $M_2^{(D)} \geq 0$. With $M_2' = -\infty$ in the MSSM limit we get $\cos\theta_2 = 0$ and $\sin\theta_2 = 1$, while $\cos\theta_2 = \sin\theta_2 = 1/\sqrt{2}$ in the Dirac limit ($M_2' = M_2 = 0$). Switching on the weak couplings among the gaugino sectors and higgsino sector, the chargino mass eigenvalues and mixing parameters derived from

$$\mathcal{M}_C^{\text{diag}} = U^T \mathcal{M}_C V \tag{84}$$

can be calculated analytically in simple form.

We study the evolution of the eigenvalues in Fig. 14 numerically by varying the mass parameters along the path

$$\begin{aligned} \mathcal{P}_C \;\; : \qquad & M_2' = my/(1+y)\,, \\ & M_2 = -my\,, \\ & M_2^D = m\,, \\ & \mu = 2m\,, \end{aligned} \tag{85}$$

for a fixed value of $m = 200$ GeV with the control parameter $-1 \leq y \leq 0$ running from the MSSM ($y = -1$) to the Dirac limit ($y = 0$). This set corresponds to mass parameters in the decoupled wino/higgsino sectors of $m_{\tilde{\chi}_1^\pm} = m$ (fixed), $m_{\tilde{\chi}_2^\pm} = m[y + 1/(1+y)]$, moving from ∞ to m, and $m_{\tilde{\chi}_3^\pm} = \mu$ (fixed). Other parameters in the chargino mass matrix (79) are chosen as $\tan\beta = 5$, and the $N = 2$ values for the couplings $\lambda_{Y,I}$ are

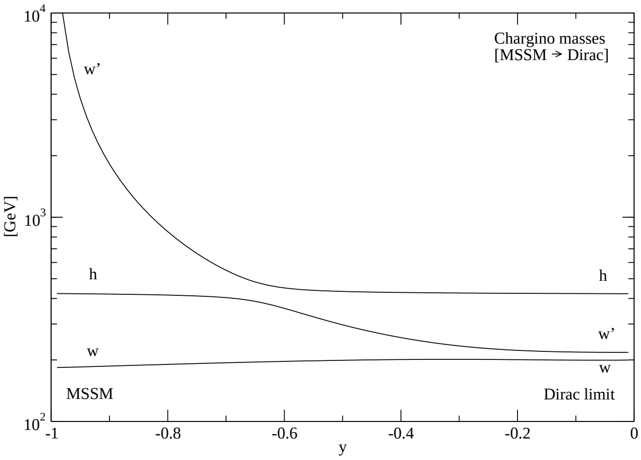

Figure 14: Evolution of the chargino masses as a function of the control parameter y from the MSSM doublet ($y = -1$) to the Dirac ($y = 0$) triplet along the path $\mathcal{P}_C$ in Eq. (85) for $m = 200$ GeV and $\tan\beta = 5$.

adopted; with parameters as specified in the scalar sector the very small vevs v_I and v_Y can be neglected.

For the parameters chosen, the descending order of the physical masses in the figure reflects, in obvious notation, the pattern $w' \gg h > w$ in the MSSM limit. At medium y, the states w' and h cross over to $h > w'$, keeping the ordering $h > w' > w$ until the Dirac limit is reached. The mixing of masses in the cross-over zone, in which they mutually approach each other, cannot be described by the standard analytical expansion applied above. They must either be obtained numerically or by analytical expansions tailored specifically for cross-over phenomena, see [55].

2) Neutralinos
Six neutral Majorana fields are incorporated in the $N = 1/N = 2$ hybrid model. The mass matrix can be extracted from the bilinear terms of the gaugino, gaugino$'$ and higgsino fields in the Lagrangian of the preceding subsection, written in the current basis $\{\tilde{B}', \tilde{B}, \tilde{W}'^0, \tilde{W}^0, \tilde{H}_u^0, \tilde{H}_d^0\}$ as

$$\mathcal{M}_N = \begin{pmatrix} M_1' & M_1^D & 0 & 0 & -\frac{1}{\sqrt{2}}\lambda_Y v_d & -\frac{1}{\sqrt{2}}\lambda_Y v_u \\ M_1^D & M_1 & 0 & 0 & \frac{1}{2}g' v_u & -\frac{1}{2}g' v_d \\ 0 & 0 & M_2' & M_2^D & -\frac{1}{\sqrt{2}}\lambda_I v_d & -\frac{1}{\sqrt{2}}\lambda_I v_u \\ 0 & 0 & M_2^D & M_2 & -\frac{1}{2}g v_u & \frac{1}{2}g v_d \\ -\frac{1}{\sqrt{2}}\lambda_Y v_d & \frac{1}{2}g' v_u & -\frac{1}{\sqrt{2}}\lambda_I v_d & -\frac{1}{2}g v_u & 0 & -\mu_n \\ -\frac{1}{\sqrt{2}}\lambda_Y v_u & -\frac{1}{2}g' v_d & -\frac{1}{\sqrt{2}}\lambda_I v_u & \frac{1}{2}g v_d & -\mu_n & 0 \end{pmatrix}, \qquad (86)$$

where

$$M_1 = M_{\tilde{B}}, \quad M_1' = M_{\tilde{B}}' + M_Y, \quad M_1^D = M_Y^D, \quad \mu_n = \mu + (\lambda_Y v_Y + \lambda_I v_I)/\sqrt{2}\,. \tag{87}$$

This 6×6 mass matrix is diagonalized by the unitary transformation

$$\mathcal{M}_N^{\rm diag} = U_N^T\, \mathcal{M}_N\, U_N. \tag{88}$$

Six neutralinos, i.e. two degrees of freedom more than in MSSM, are predicted in the general $N = 1/N = 2$ hybrid model, labeled $\tilde{\chi}^0_{1\cdots 6}$ (ultimately ordered according to ascending mass values). They evolve from the MSSM by raising the magnitude of the gaugino mass parameters $M'_{1,2}$ from $-\infty$ to finally 0 in the Dirac limit.

In general the diagonalization of the 6×6 neutralino mass matrix cannot be carried out in analytic form. However, in the limit in which the supersymmetry masses are much larger than the electroweak scale, approximate solutions can be found analytically. First switching off the electroweak mixings among the bino, wino and higgsino sectors leaves us with two bino mass eigenvalues, two wino mass eigenvalues and two higgsino mass eigenvalues:

$$\begin{aligned} \overline{m}^0_{1,2} &= \frac{1}{2}\left||M_1 + M_1'| \mp \delta_1\right|\,, \\ \overline{m}^0_{3,4} &= \frac{1}{2}\left||M_2 + M_2'| \mp \delta_2\right|\,, \\ \overline{m}^0_{5,6} &= \mu\,, \end{aligned} \tag{89}$$

with $\delta_{1,2} = \sqrt{(M'_{1,2} - M_{1,2})^2 + 4(M^D_{1,2})^2}$, and the block-diagonal mixing matrix

$$\overline{U}_N = {\rm diag}\left(\overline{U}_1, \overline{U}_2, \overline{U}_h\right),$$

$$\text{with} \quad \overline{U}_{1,2} = \begin{pmatrix} c_{1,2} & -is_{1,2} \\ s_{1,2} & ic_{1,2} \end{pmatrix} \quad \text{and} \quad \overline{U}_h = \begin{pmatrix} i/\sqrt{2} & -1/\sqrt{2} \\ i/\sqrt{2} & 1/\sqrt{2} \end{pmatrix}, \tag{90}$$

with the mixing angles $c_{1,2}/s_{1,2} = \sqrt{[1 \pm (M'_{1,2} - M_{1,2})/\delta_{1,2}]/2}$. Switching on the weak couplings among the bino and wino gaugino sectors and higgsino sector, the mass eigenvalues and mixing parameters can be calculated using the block-diagonalization method [55].

The numerical evolution of the neutralinos in the hybrid model is displayed in Fig. 15 as a function of the control parameter y for the same path and parameter set as in the chargino sector, Eq. (85), and supplemented by the bino/wino mass relations $M_1^{(D)} = M_2^{(D)}/2$, and setting $v_I = v_Y = 3$ GeV.

The evolution of the neutralino masses follows the same pattern as the charginos, though being more complex due to the increased number of states. Starting from the mass pattern $w' > b' \gg h_1 = h_2 > w > b$ of the neutral states in the MSSM limit for the

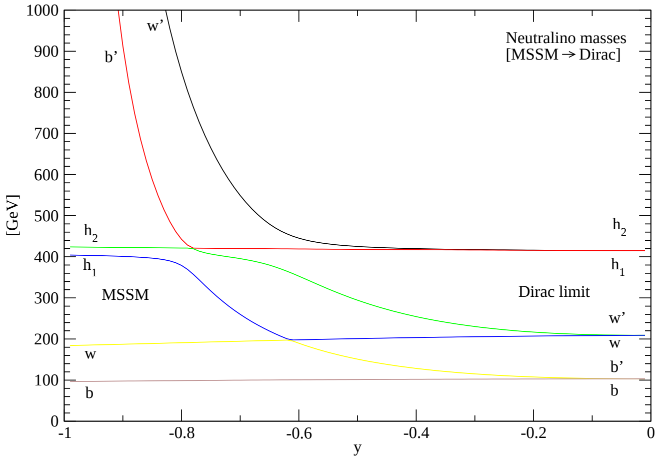

Figure 15: Evolution of the neutralino masses as a function of the control parameter y from the MSSM ($y = -1$) quartet to the Majorana sextet, merging to the Dirac triplet in the ($y = 0$) limit, for the same path (85) as in the chargino sector with bino/wino relations chosen as $M_1^{(D)}/M_2^{(D)} = 1/2$.

parameters chosen above, the first cross-over is observed for $b' \leftrightarrow h_1$, followed by $w' \leftrightarrow h_2$ and $b' \leftrightarrow w$ at roughly the same position. The mass system moves to the final pattern $h_1 = h_2 > w' = w > b' = b$ in the Dirac limit.

The transition from the Majorana to the Dirac theory in the limits M_2', M_2 and $M_1', M_1 \to 0$ can easily be studied by analyzing the mass matrix $\mathcal{M}_N$ for vanishing gaugino/higgsino mixing. The eigenvalues of the matrix come in pairs of opposite signs: $\pm m_j$ for $j = 1, 2, 3$. The Majorana fields in each pair, denoted by $\tilde{\chi}_\pm$ according to the sign of the eigenvalue, can be combined to one Dirac field,

$$\tilde{\chi}_D = (\tilde{\chi}_+ + i\tilde{\chi}_-)/\sqrt{2}\,, \tag{91}$$

the superposition giving rise to vanishing contractions $\langle \tilde{\chi}_D \tilde{\chi}_D \rangle = 0$, as required for Dirac fields.

The $\pm$ pairing of the eigenstates is not restricted to the hybrid neutralino mass matrix with vanishing gaugino/higgsino mixing but it is also realized if the gaugino/higgsino mixing is switched on and the couplings $\lambda_{Y,I}$ are given by the $N = 2$ relations, $\lambda_Y = -g'/\sqrt{2}$ and $\lambda_I = g/\sqrt{2}$. The key is the vanishing of the coefficients of odd powers of the eigenvalues in the characteristic eigenvalue equation:

$$\det(\mathcal{M}_N - m) = r_0 + r_2 m^2 + r_4 m^4 + r_6 m^6 = 0 \tag{92}$$

with the coefficients given by

$$\begin{aligned}
r_6 &= 1\,, \\
r_4 &= -\frac{1}{2}\mathrm{tr}(\mathcal{M}_N^2) \\
&\to -[(M_Y^D)^2 + (M_I^D)^2 + \mu_n^2 + m_Z^2]\,, \\
r_2 &= \frac{1}{8}[\mathrm{tr}(\mathcal{M}_N^2)]^2 - \frac{1}{4}\mathrm{tr}(\mathcal{M}_N^4) \\
&\to (M_Y^D M_I^D)^2 + [(M_Y^D)^2 + (M_I^D)^2]\mu_n^2 + 2m_Z^2[(M_Y^D)^2 c_W^2 + 2(M_I^D)^2 s_W^2] \\
&- 2m_Z^2(M_Y^D s_W^2 + M_I^D c_W^2)\mu_n c_{2\beta} + m_Z^4\,, \\
r_0 &= -\frac{1}{48}[\mathrm{tr}(\mathcal{M}_N^2)]^3 + \frac{1}{12}[\mathrm{tr}(\mathcal{M}_N^3)]^2 + \frac{1}{8}\mathrm{tr}(\mathcal{M}_N^4)\,\mathrm{tr}(\mathcal{M}_N^2) - \frac{1}{6}\mathrm{tr}(\mathcal{M}_N^6) \\
&\to -(M_Y^D M_I^D \mu_n)^2 + 2m_Z^2 M_Y^D M_I^D \mu_n(M_Y^D c_W^2 + M_I^D s_W^2)c_{2\beta} - m_Z^4(M_Y^D c_W^2 + M_I^D s_W^2)
\end{aligned} \tag{93}$$

The odd coefficients r_{2j+1} are linear in traces of odd powers of $\mathcal{M}_N$ which vanish. While this is obvious for $\mathrm{tr}(\mathcal{M}_N)$, it can easily be proven also for odd powers of the mass matrix if the submatrix that mixes the mass submatrix of the gauginos with the mass submatrix of the higgsinos is orthogonal. This is satisfied in Eq. (86), a sufficient (but not necessary) condition for orthogonality being the $N = 2$ symmetry of the basic Lagrangian.

In the limit of large supersymmetry scales (in relation to the electroweak scale), the Dirac chargino fields and their charge conjugates are given by

$$\tilde{\chi}^-_{D1} = \tilde{W}'^-_L + \tilde{W}^-_R, \qquad \tilde{\chi}^+_{D1} = -\tilde{W}^+_L - \tilde{W}'^+_R, \tag{94}$$

$$\tilde{\chi}^-_{D2} = \tilde{W}^-_L + \tilde{W}'^-_R, \qquad \tilde{\chi}^+_{D2} = -\tilde{W}'^+_L - \tilde{W}^+_R, \tag{95}$$

$$\tilde{\chi}^-_{D3} = \tilde{H}^-_{dL} + \tilde{H}^-_{uR}, \qquad \tilde{\chi}^+_{D3} = \tilde{H}^+_{uL} + \tilde{H}^+_{dR}, \tag{96}$$

whereas the Dirac neutralino fields and their charge conjugates are

$$\tilde{\chi}^0_{D1} = \tilde{b}'_L + \tilde{b}_R, \qquad \tilde{\chi}^{0c}_{D1} = -\tilde{b}_L - \tilde{b}'_R, \tag{97}$$

$$\tilde{\chi}^0_{D2} = \tilde{W}'^0_L + \tilde{W}^0_R, \qquad \tilde{\chi}^{0c}_{D2} = -\tilde{W}^0_L - \tilde{W}'^0_R, \tag{98}$$

$$\tilde{\chi}^0_{D3} = i(\tilde{H}^0_{dL} - \tilde{H}^0_{uR}), \qquad \tilde{\chi}^{0c}_{D3} = i(\tilde{H}^0_{uL} - \tilde{H}^0_{dR}), \tag{99}$$

up to terms of order v/M_{SUSY}. Expressed in terms of these fields, the Lagrangians for matter-chargino/neutralino interactions in the MSSM Majorana limit and in the Dirac theory can be written as

$$\mathcal{L}^{\mathrm{C}}_{\mathrm{Majo}} = g\,\overline{u_L}\,\tilde{\chi}^+_1\tilde{d}_L + g\,\overline{\tilde{\chi}^+_1}\,u_L\,\tilde{d}^*_L - g\,\overline{d_L}\,\tilde{\chi}^-_1\,\tilde{u}_L - g\,\overline{\tilde{\chi}^-_1}\,d_L\,\tilde{u}^*_L\,, \tag{100}$$

$$\mathcal{L}^{\mathrm{C}}_{\mathrm{Dirac}} = g\,\overline{u_L}\,\tilde{\chi}^+_{D2}\tilde{d}_L + g\,\overline{\tilde{\chi}^+_{D2}}\,u_L\,\tilde{d}^*_L - g\,\overline{d_L}\,\tilde{\chi}^-_{D1}\tilde{u}_L - g\,\overline{\tilde{\chi}^-_{D1}}\,d_L\,\tilde{u}^*_L\,, \tag{101}$$

and

$$\mathcal{L}^{\mathrm{N}}_{\mathrm{Majo}} = -g_{Li}\,\overline{f_L}\,\tilde{\chi}^0_i\,\tilde{f}_L - g^*_{Li}\,\overline{\tilde{\chi}^0_i}\,f_L\,\tilde{f}^*_L + g_{Ri}\,\overline{f_R}\,\tilde{\chi}^0_i\,\tilde{f}_R + g^*_{Ri}\,\overline{\tilde{\chi}^0_i}\,f_R\,\tilde{f}^*_R\,, \tag{102}$$

$$\mathcal{L}^{\mathrm{N}}_{\mathrm{Dirac}} = -g_{Li}\,\overline{f_L}\,\tilde{\chi}^0_{Di}\,\tilde{f}_L - g^*_{Li}\,\overline{\tilde{\chi}^0_{Di}}\,f_L\,\tilde{f}^*_L + g_{Ri}\,\overline{f_R}\,\tilde{\chi}^{0c}_{Di}\,\tilde{f}_R + g^*_{Ri}\,\overline{\tilde{\chi}^{0c}_{Di}}\,f_R\,\tilde{f}^*_R\,, \tag{103}$$

where

$$g_{Li} = \sqrt{2}\left[g' Y_{f_L}\delta_{i1} + g I^3_f \delta_{i2}\right], \quad \text{and} \quad g_{Ri} = \sqrt{2}\, g' Y_{f_R}\delta_{i1}. \tag{104}$$

Here $u/\tilde{u}$ correspond to up-type (s)quarks or (s)neutrinos, whereas $d/\tilde{d}$ denote down-type (s)quarks or charged (s)leptons. The mixings from electroweak symmetry breaking as well as from the CKM matrix have been neglected.

In the approximation described by the Dirac Lagrangians a Dirac charge D [48] can be defined which is conserved in all processes:

$$\begin{aligned} D[\tilde{q}^{1,2}_L] &= D[\tilde{\ell}^{1,2}_L] = D[\tilde{\nu}^{1,2}] = D[\tilde{\chi}^{0c}_D] = D[\tilde{\chi}^+_{D1}] = D[\tilde{\chi}^-_{D2}] = -1\,, && (105)\\ D[\tilde{q}^{1,2}_R] &= D[\tilde{\ell}^{1,2}_R] \qquad\qquad\quad = D[\tilde{\chi}^0_D] = D[\tilde{\chi}^-_{D1}] = D[\tilde{\chi}^+_{D2}] = +1\,. && (106) \end{aligned}$$

Antiparticles carry the corresponding opposite Dirac charges $-D$. The Dirac charges of all SM particles vanish. The squarks $\tilde{q}^{1,2}$, sleptons $\tilde{\ell}^{1,2}$, and sneutrinos $\tilde{\nu}^{1,2}$ belong to the first and second generation. L, R mixing and large couplings to higgsinos preclude the extension of this approximate scheme to the third generation. Nevertheless, the scheme proves useful for a quick overview of allowed and forbidden processes in the first two generations. For example, the production processes $e^-_L e^-_L \to \tilde{e}^-_L \tilde{e}^-_L$ and $e^-_R e^-_R \to \tilde{e}^-_R \tilde{e}^-_R$ with equal helicities are forbidden while the opposite-helicity process $e^-_L e^-_R \to \tilde{e}^-_L \tilde{e}^-_R$ is allowed.

Chargino production

Chargino pair production in e^+e^- annihilation will be taken as an example to illustrate the characteristic features, common, *mutatis mutandis*, also to neutralino production. The chargino reaction proceeds through s-channel γ, Z and t-channel $\tilde{\nu}_e$ exchanges. The cross sections in the general hybrid theory are given by

$$\begin{aligned} \frac{d\sigma}{d\cos\theta}[e^+e^- \to \tilde{\chi}^+_1\tilde{\chi}^-_1] = \frac{\pi\alpha^2\lambda^{1/2}_{11}}{16 s^4_W s}&\Bigg[\frac{[s^2 - 4s^2_W m^2_Z s + 8 s^4_W m^4_Z][2 + \lambda_{11}(\cos^2\theta - 1)]}{(s - m^2_Z)^2}\\ &- c^2_2\,\frac{s[s - 2s^2_W m^2_Z][1 - \lambda_{11} + (1 - \lambda^{1/2}_{11}\cos\theta)^2]}{(s - m^2_Z)(t - m^2_{\tilde{\nu}})} + c^4_2\,\frac{s^2(1 - \lambda^{1/2}_{11}\cos\theta)^2}{2(t - m^2_{\tilde{\nu}})^2}\Bigg], \end{aligned} \tag{107}$$

$$\begin{aligned} \frac{d\sigma}{d\cos\theta}[e^+e^- \to \tilde{\chi}^+_2\tilde{\chi}^-_2] = \frac{\pi\alpha^2\lambda^{1/2}_{22}}{16 s^4_W s}&\Bigg[\frac{[s^2 - 4s^2_W m^2_Z s + 8 s^4_W m^4_Z][2 + \lambda_{22}(\cos^2\theta - 1)]}{(s - m^2_Z)^2}\\ &- s^2_2\,\frac{s[s - 2s^2_W m^2_Z][1 - \lambda_{22} + (1 - \lambda^{1/2}_{22}\cos\theta)^2]}{(s - m^2_Z)(t - m^2_{\tilde{\nu}})} + s^4_2\,\frac{s^2(1 - \lambda^{1/2}_{22}\cos\theta)^2}{2(t - m^2_{\tilde{\nu}})^2}\Bigg], \end{aligned} \tag{108}$$

$$\frac{d\sigma}{d\cos\theta}[e^+e^- \to \tilde{\chi}^\pm_1\tilde{\chi}^\mp_2] = \frac{\pi\alpha^2\lambda^{1/2}_{12}}{16 s^4_W s}\, c^2_2 s^2_2\, \frac{s^2(1 - \lambda_{12}\cos\theta)^2 - (m^2_{\tilde{\chi}^\pm_1} - m^2_{\tilde{\chi}^\pm_2})^2}{(t - m^2_{\tilde{\nu}})^2}\,, \tag{109}$$

where $\lambda_{ij} = \lambda^{1/2}(1, m^2_{\tilde{\chi}^\pm_i}/s, m^2_{\tilde{\chi}^\pm_j}/s)$, and we ignore the Z boson width. As before, electroweak symmetry breaking effects in the chargino mixing matrix have been neglected.

The mixing angles c_2 and s_2, defined in Eq. 83, only modify the t-channel sneutrino amplitude, so that they can be determined from the angular distribution of $\tilde{\chi}_1^+\tilde{\chi}_1^-$ production in a straightforward manner. The MSSM limit corresponds to Eq. 107 with $c_2 = 1$ and $s_2 = 0$. In the Dirac limit, using the basis Eq. 108, Eq. 109 for the two degenerate Dirac charginos, one finds

$$\frac{d\sigma}{d\cos\theta}[e^+e^- \to \tilde{\chi}_{D1}^+\tilde{\chi}_{D1}^-] = \frac{\pi\alpha^2\lambda_{11}^{1/2}}{16 s_W^4 s}\left[\frac{[s^2 - 4s_W^2 m_Z^2 s + 8 s_W^4 m_Z^4][2 + \lambda_{11}(\cos^2\theta - 1)]}{(s - m_Z^2)^2}\right.$$
$$\left. - \frac{s[s - 2s_W^2 m_Z^2][1 - \lambda_{11} + (1 - \lambda_{11}^{1/2}\cos\theta)^2]}{(s - m_Z^2)(t - m_{\tilde{\nu}}^2)} + \frac{s^2(1 - \lambda_{11}^{1/2}\cos\theta)^2}{2(t - m_{\tilde{\nu}}^2)^2}\right], \tag{110}$$

$$\frac{d\sigma}{d\cos\theta}[e^+e^- \to \tilde{\chi}_{D2}^+\tilde{\chi}_{D2}^-] = \frac{\pi\alpha^2\lambda_{22}^{1/2}}{16 s_W^4 s}\,\frac{[s^2 - 4s_W^2 m_Z^2 s + 8 s_W^4 m_Z^4][2 + \lambda_{22}(\cos^2\theta - 1)]}{(s - m_Z^2)^2} \tag{111}$$

$$\frac{d\sigma}{d\cos\theta}[e^+e^- \to \tilde{\chi}_{D1}^\pm\tilde{\chi}_{D2}^\mp] = 0. \tag{112}$$

It is noteworthy that the cross sections for $\tilde{\chi}_1^+\tilde{\chi}_1^-$ production in the MSSM limit and for $\tilde{\chi}_{D1}^+\tilde{\chi}_{D1}^-$ production in the Dirac limit are identical. This is in obvious contrast to neutralino and gluino production, which are Majorana particles in one limit and Dirac particles in the other.

Signatures at the LHC: Squark cascade decays

Cascade decays are crucial for the analysis of the non-colored supersymmetry sector at LHC. Following the rules discussed earlier, we will study invariant masses of quark-jets with charged leptons in squark cascade decays:

$$\begin{array}{lll}
\text{Charginos:} & \text{MSSM:} & \tilde{u}_L \to d\,\tilde{\chi}_1^+, \to d\,\nu_l\,\tilde{l}_L^+,\; d\,l^+\,\tilde{\nu}_l \to d\,l^+\,\nu_l\,\tilde{\chi}_1^0 \\
 & & \tilde{d}_L \to u\,\tilde{\chi}_1^- \to u\,\bar{\nu}_l\,\tilde{l}_L^-,\; u\,l^-\,\tilde{\nu}_l^* \to u\,l^-\,\bar{\nu}_l\,\tilde{\chi}_1^0\,, \\
 & \text{Dirac:} & \tilde{u}_L \to d\,\tilde{\chi}_{D1}^+ \to d\,l^+\,\tilde{\nu}_l \to d\,l^+\,\nu_l\,\tilde{\chi}_{D1}^{0c}\,, \\
 & & \tilde{d}_L \to u\,\tilde{\chi}_{D2}^- \to u\,\bar{\nu}_l\,\tilde{l}_L^- \to u\,l^-\,\bar{\nu}_l\,\tilde{\chi}_{D1}^{0c}\,, \\
\text{Neutralinos:} & \text{MSSM:} & \tilde{q}_L \to q\,\tilde{\chi}_2^0 \to q\,l^\pm\,\tilde{l}_L^\mp \to q\,l^\pm\,l^\mp\,\tilde{\chi}_1^0\,, \\
 & \text{Dirac:} & \tilde{q}_L \to q\,\tilde{\chi}_{D2}^{c0} \to q\,l^+\,\tilde{l}_L^- \to q\,l^+\,l^-\,\tilde{\chi}_1^0\,.
\end{array}$$

Due to the CP invariance, the charge conjugated versions of these processes are simply obtained by flipping the gauge/Dirac charges and chiralities at each step.

As evident from the list above, the decay chains differ in their chirality structure between the MSSM and the Dirac theory, which will leave a characteristic imprint on the angular distributions of visible decay jets and leptons. For the squark-chargino cascades this is illustrated by the quark-lepton invariant mass distributions shown in Fig. 16.

Also shown in the figure is an example of the general 2-Majorana hyper-system away from the Dirac limit. In this case one obtains two wino-like charginos $\chi_{1,2}^\pm$ with distinct

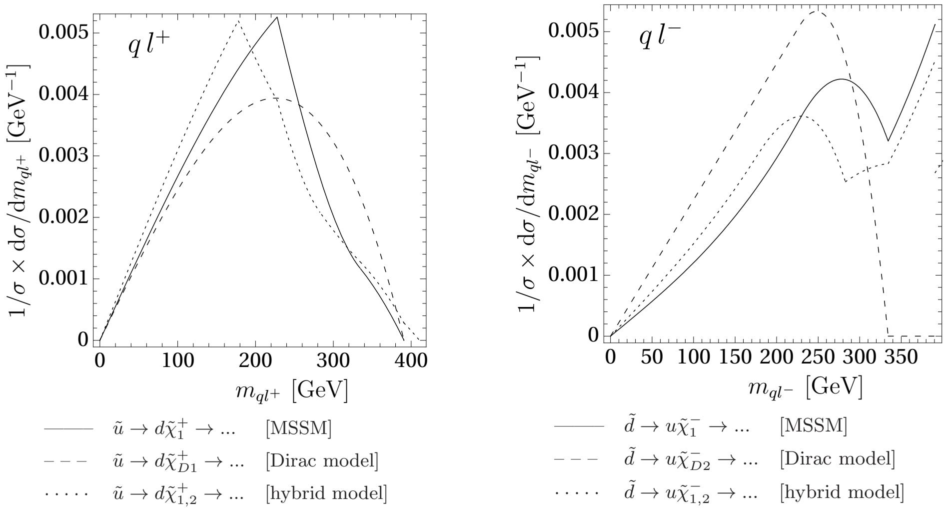

Figure 16: Quark-lepton invariant mass distributions for squark decay chains with intermediate charginos, comparing the $N = 1$ MSSM (solid lines) with the $N = 2$ Dirac gaugino theory (dashed lines) and the intermediate hybrid theory (dotted lines). Numerical inputs for the plots are $m_{\tilde q} = 565$ GeV, $m_{\tilde\chi_1^\pm} = m_{\tilde\chi_{D1}^\pm} = m_{\tilde\chi_{D2}^\pm} = 184$ GeV, $m_{\tilde l} = m_{\tilde\nu} = 125.3$ GeV, and $m_{\tilde\chi_1^0} = m_{\tilde\chi_{D1}^0} = 97.7$ GeV. For the case of the hybrid model, the second chargino mass is $m_{\tilde\chi_2^\pm} = 199$ GeV, corresponding to a mixing angle $\cos\theta_2 = 0.6$. Electroweak symmetry breaking effects on the chargino and neutralino mixing matrices have been neglected.

masses. The dotted lines in the plots corresponds to a scenario with relatively small departure from the Dirac limit, so that the two chargino masses are of the same order and the $\tilde{W}/\tilde{W}'$ mixing angle is close to maximal mixing.

Nevertheless, the distributions of the 2-Majorana hyper-system are closer to the MSSM in the plots, while the Dirac limit leads to drastically different distributions. This can be understood from the fact that the two independent charginos $\tilde{\chi}_1^{\pm}$ and $\tilde{\chi}_2^{\pm}$ in the hybrid model become degenerate in the exact Dirac limit. Interference effects lead to large mixing between the two states in this limit. However, a slight deviation from the Dirac limit is already sufficient to effectively turn off these interference contributions, since the widths of both charginos is relatively small.

The squark-neutralino cascades have been worked out in [48], and are reproduced in Fig. 16. Again, the plots show distinct differences between the MSSM and Dirac limits, which can be exploited to experimentally distinguish the two cases at the LHC.

Signatures at ILC: Selectron pair-production

Conservation of the Dirac charge D in the first generation forbids the production of selectrons in equal-helicity e^-e^- collisions but allows the production in opposite-helicity collisions in the Dirac theory while all three helicity combinations are non-trivially realized in Majorana theories:

$$\begin{aligned} e^-_L e^-_L &\to \tilde{e}^-_L \tilde{e}^-_L \,,\; e^-_R e^-_R \to \tilde{e}^-_R \tilde{e}^-_R \,, && (113) \\ e^-_L e^-_R &\to \tilde{e}^-_L \tilde{e}^-_R \,. && (114) \end{aligned}$$

Three other independent processes are possible in e^-e^+ collisions:

$$\begin{aligned} e^-_L e^+_L &\to \tilde{e}^-_L \tilde{e}^+_R \,, && (115) \\ e^-_L e^+_R &\to \tilde{e}^-_L \tilde{e}^+_L \,,\; e^-_R e^+_L \to \tilde{e}^-_R \tilde{e}^+_R \,. && (116) \end{aligned}$$

Noting that $(\psi_{L/R})^c = (\psi^c)_{R/L}$, the additional process $e^-_R e^+_R \to \tilde{e}^-_R \tilde{e}^+_L$ in the second group is the CP-conjugate of the first process and needs not be analyzed separately. Since non-zero s-channel γ, Z exchange requires opposite lepton helicities, the first electron/positron process is driven only by neutralino exchanges while the other two processes are mediated by both t-channel neutralino and s-channel vector-boson exchanges. Moreover, the first process violates conservation of the D charge and thus is forbidden in the Dirac theory.

1) e^-e^- collisions

In the general hybrid hyper-system on which we have based for the detailed analyses, the e^-e^- scattering amplitudes for selectron pair production can be written as

$$\begin{aligned} \mathcal{A}[e^-_L e^-_L \to \tilde{e}^-_L \tilde{e}^-_L] &= -2e^2 \left[\mathcal{M}_{LL}(s,t) + \mathcal{M}_{LL}(s,u)\right] \,, && (117) \\ \mathcal{A}[e^-_R e^-_R \to \tilde{e}^-_R \tilde{e}^-_R] &= 2e^2 \left[\mathcal{M}^*_{RR}(s,t) + \mathcal{M}^*_{RR}(s,u)\right] \,, && (118) \end{aligned}$$

for the same helicities and

$$\begin{aligned}
\mathcal{A}[e^-_L e^-_R \to \tilde{e}^-_L \tilde{e}^-_R] &= e^2 \lambda^{1/2}_{LR} \sin\theta \, \mathcal{D}_{LR}(s,t)\,, &(119)\\
\mathcal{A}[e^-_R e^-_L \to \tilde{e}^-_L \tilde{e}^-_R] &= -e^2 \lambda^{1/2}_{LR} \sin\theta \, \mathcal{D}_{RL}(s,u)\,, &(120)
\end{aligned}$$

for the opposite helicities, with the two-body final state kinematic factor $\lambda_{ab} = \lambda(1, m^2_{\tilde{e}_a}/s, m^2_{\tilde{e}_b}/s)$, with $a, b = L, R$, and

$$\lambda(1,x,y) = 1 + x^2 + y^2 - 2(x + y + xy). \tag{121}$$

Here θ is the scattering angle, and the dimensionless neutralino functions $\mathcal{M}_{ab}$ and $\mathcal{D}_{ab}$ $(a, b = L, R)$ are defined by

$$\mathcal{M}_{ab}(s,t/u) = \sum_{k=1}^{6} \frac{m_{\tilde{\chi}^0_k}}{\sqrt{s}} \mathcal{V}_{ak} \mathcal{V}_{bk} \, D_{kt/u}\,, \tag{122}$$

$$\mathcal{D}_{ab}(s,t/u) = \sum_{k=1}^{6} \mathcal{V}_{ak} \mathcal{V}^*_{bk} \, D_{kt/u}\,. \tag{123}$$

They are determined by the neutralino propagators $D_{kt} = s/(t - m^2_{\tilde{\chi}^0_k})$, and similar for D_{ku}, and the effective mixing coefficients

$$\mathcal{V}_{Lk} = U_{N2k}/(2c_W) + U_{N4k}/(2s_W)\,, \qquad \mathcal{V}_{Rk} = U_{N2k}/c_W\,. \tag{124}$$

The neutralino mixing matrix elements $U_{N\alpha k}$, introduced in Eq. 88, have a very simple structure if effects from electroweak symmetry breaking are neglected, see Eq. (90)

After calculating the polarization averaged squared matrix elements and including the phase space factor, the differential cross sections are

$$\begin{aligned}
\frac{d\sigma_{LL}}{d\cos\theta} &= \frac{\pi\alpha^2}{4s} \lambda^{1/2}_{LL} \, | \, \mathcal{M}_{LL}(s,t) + \mathcal{M}_{LL}(s,u) \, |^2\,, &(125)\\
\frac{d\sigma_{RR}}{d\cos\theta} &= \frac{\pi\alpha^2}{4s} \lambda^{1/2}_{RR} \, | \, \mathcal{M}_{RR}(s,t) + \mathcal{M}_{RR}(s,u) \, |^2\,, &(126)\\
\frac{d\sigma_{LR}}{d\cos\theta} &= \frac{\pi\alpha^2}{4s} \lambda^{3/2}_{LR} \sin^2\theta \left[|\mathcal{D}_{LR}(s,t)|^2 + |\mathcal{D}_{RL}(s,u)|^2 \right]. &(127)
\end{aligned}$$

Finally, the unpolarized total cross sections can be obtained by performing the remaining integration over the scattering angle θ. Note that σ_{LR} and σ_{RL} are not physically distinguishable in the e^-e^- case, unlike for e^+e^- annihilation. The cross sections reduce, on the one side, to the familiar MSSM form, see [59], while in the Dirac theory, on the other side, they simplify considerably to

$$\begin{aligned}
\sigma[e^-e^- \to \tilde{e}^-_L \tilde{e}^-_L] &= \sigma[e^-e^- \to \tilde{e}^-_R \tilde{e}^-_R] = 0\,, &(128)\\
\sigma[e^-e^- \to \tilde{e}^-_L \tilde{e}^-_R] &= \frac{\pi\alpha^2}{2c^4_W s} \left[(1 + 2m^2_{\tilde{\chi}^0_{D1}}/s - m^2_{\tilde{e}_L}/s - m^2_{\tilde{e}_R}/s) \, L'_{D1} - 2\beta' \right]. &(129)
\end{aligned}$$

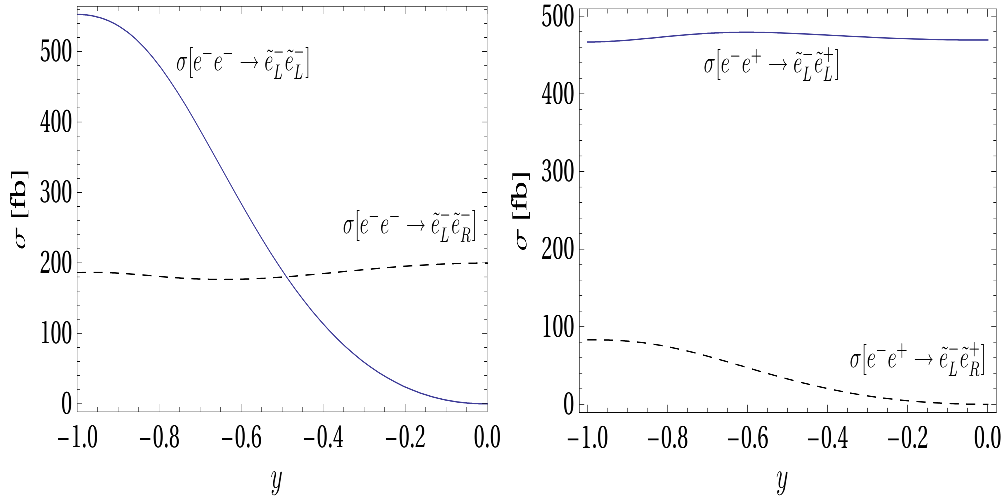

Figure 17: Dependence of the cross sections for same-sign (left) and opposite-sign (right) selectron production on the Dirac/Majorana control parameter y, for $\sqrt{s} = 500$ GeV and SPS1a$'$ parameters [54]. Not shown are the cross sections for $e^-e^\pm \to \tilde{e}_R^-\tilde{e}_R^\pm$, which, apart from the different normalization, shows a similar behavior as the cross section for $e^-e^- \to \tilde{e}_L^-\tilde{e}_L^\pm$.

with $\beta' = \lambda_{LR}^{1/2}$ and the logarithmic function defined by

$$L'_i = \log \frac{1+\beta' + (2m^2_{\tilde{\chi}^0_i} - m^2_{\tilde{e}_L} - m^2_{\tilde{e}_R})/s}{1-\beta' + (2m^2_{\tilde{\chi}^0_i} - m^2_{\tilde{e}_L} - m^2_{\tilde{e}_R})/s} \,. \tag{130}$$

The vanishing of the LL and RR cross sections is obvious from D-charge conservation. In the absence of higgsino exchanges only the bino-exchange can drive the LR process.

The evolution of the total cross section from the MSSM to the Dirac limit is illustrated for the two characteristic processes $e^-e^- \to \tilde{e}_L^-\tilde{e}_L^-$ and $e^-e^- \to \tilde{e}_L^-\tilde{e}_R^-$ in the left panel of Fig. 17, which demonstrates how the first process is switched off when the Dirac limit is approached.

2) e^+e^- collisions

The analysis of the e^-e^+ processes follows the same path. By introducing a dimensionless s-channel Z boson propagator $D_Z = s/(s - m_Z^2 + i m_Z \Gamma_Z)$ and four bilinear charges

$$Z^+_{LL} = 1 + \frac{s_W^2 - 1/2}{c_W^2} D_Z \,, \quad Z^-_{LL} = 1 + \frac{(s_W^2 - 1/2)^2}{c_W^2 s_W^2} D_Z \,, \tag{131}$$

$$Z^+_{RR} = 1 + \frac{s_W^2}{c_W^2} D_Z \,, \qquad Z^-_{RR} = 1 + \frac{s_W^2 - 1/2}{c_W^2} D_Z \,, \tag{132}$$

we obtain six non-vanishing helicity amplitudes

$$\mathcal{A}[e^-_L e^+_R \to \tilde{e}^-_L \tilde{e}^+_L] = -e^2 \lambda^{1/2}_{LL} \sin\theta \left[\mathcal{D}_{LL}(s,t) + Z^-_{LL}\right] \,, \tag{133}$$

$$\mathcal{A}[e^-_R e^+_L \to \tilde{e}^-_L \tilde{e}^+_L] = -e^2 \lambda^{1/2}_{LL} \sin\theta Z^+_{LL} \,, \tag{134}$$

$$\mathcal{A}[e^-_L e^+_R \to \tilde{e}^-_R \tilde{e}^+_R] = -e^2 \lambda^{1/2}_{RR} \sin\theta Z^-_{RR} \,, \tag{135}$$

$$\mathcal{A}[e^-_R e^+_L \to \tilde{e}^-_R \tilde{e}^+_R] = -e^2 \lambda^{1/2}_{RR} \sin\theta \left[\mathcal{D}_{RR}(s,t) + Z^+_{RR}\right] \,, \tag{136}$$

$$\mathcal{A}[e^-_L e^+_L \to \tilde{e}^-_L \tilde{e}^+_R] = 2e^2 \mathcal{M}_{LR}(s,t) \,, \tag{137}$$

$$\mathcal{A}[e^-_R e^+_R \to \tilde{e}^-_R \tilde{e}^+_L] = -2e^2 \mathcal{M}^*_{RL}(s,t) \,. \tag{138}$$

By squaring the helicity amplitudes, the differential cross sections can easily be derived. The squares are summed incoherently if the initial lepton helicities are not specified experimentally.

As before, the cross sections reduce to the familiar MSSM limit on one side, while in the Dirac limit, on the other side, the processes with LR/RL initial state helicities remain allowed, but the LL and RR processes are excluded by D-charge conservation. The D-charge of the pair $\tilde{e}^-_L \tilde{e}^-_R$ vanishes, thus allowing production in e^-e^- collisions, but the pair $\tilde{e}^-_L \tilde{e}^+_R$ carries the charge $D = 2$ so that production of this pair in e^-e^+ collisions is forbidden.

The continuous transition from the MSSM to the Dirac limit is illustrated in the right panel of Fig. 17, for the two representative total cross sections of $e^-e^+ \to \tilde{e}^-_L \tilde{e}^+_R$ and $e^-e^+ \to \tilde{e}^-_L \tilde{e}^+_L$.

2. Electroweak scalar bosons

Masses and mixing

The scalar/Higgs sector involves various components in the basic Lagrangian, terms derived from the $N = 2$ Higgs-Higgs-scalar interactions, the superpotential, the D-terms and the soft breaking terms. Expanding the scalar/Higgs potential about the vacuum expectation values of the neutral fields, $v_{u/d}, v_{Y/I}$, linear and bilinear terms of the physical fields associated with the masses are generated, while tri- and quadri-linear terms describe the self-interactions of the physical scalar/Higgs fields.

To stabilize the system, the coefficients of the linear terms must vanish; this condition connects the vacuum expectation values with the basic parameters of the Lagrangian:

$$\begin{aligned}
v_Y &= \frac{v^2}{4\tilde{m}_Y^2\tilde{m}_I^2-\lambda_Y^2\lambda_I^2v^4}\Big\{2\tilde{m}_I^2\Big[g'M_Y^Dc_{2\beta}-\sqrt{2}\lambda_Y\mu+(M_Y+A_Y)\lambda_Ys_{2\beta}/\sqrt{2}\Big]\\
&\qquad +\lambda_Y\lambda_Iv^2\Big[gM_I^Dc_{2\beta}+\sqrt{2}\lambda_I\mu-(M_I-A_I)\lambda_Is_{2\beta}/\sqrt{2}\Big]\Big\}\\
&\sim \frac{v^2}{2\tilde{m}_Y^2}\Big[g'M_Y^Dc_{2\beta}-\sqrt{2}\lambda_Y\mu+(M_Y+A_Y)\lambda_Ys_{2\beta}/\sqrt{2}\Big] \quad \text{for} \quad \tilde{m}_{Y,I}\gg\lambda_{Y,I}v, \qquad (139)\\
v_I &= \frac{v^2}{4\tilde{m}_Y^2\tilde{m}_I^2-\lambda_Y^2\lambda_I^2v^4}\Big\{2\tilde{m}_Y^2\Big[-gM_I^Dc_{2\beta}-\sqrt{2}\lambda_I\mu+(M_I-A_I)\lambda_Is_{2\beta}/\sqrt{2}\Big]\\
&\qquad -\lambda_Y\lambda_Iv^2\Big[g'M_Y^Dc_{2\beta}-\sqrt{2}\lambda_Y\mu+(M_Y+A_Y)\lambda_Ys_{2\beta}/\sqrt{2}\Big]\Big\}\\
&\sim -\frac{v^2}{2\tilde{m}_I^2}\Big[gM_I^Dc_{2\beta}+\sqrt{2}\lambda_I\mu-(M_I-A_I)\lambda_Is_{2\beta}/\sqrt{2}\Big] \quad \text{for} \quad \tilde{m}_{Y,I}\gg\lambda_{Y,I}v, \qquad (140)
\end{aligned}$$

with the abbreviations

$$\begin{aligned}
\tilde{m}_Y^2 &= m_Y^2+m_Y'^2+M_Y^2+4(M_Y^D)^2+\tfrac{1}{2}\lambda_Y^2v^2, \qquad (141)\\
\tilde{m}_I^2 &= m_I^2+m_I'^2+M_I^2+4(M_I^D)^2+\tfrac{1}{2}\lambda_I^2v^2. \qquad (142)
\end{aligned}$$

The Higgs vevs $v_{u,d}$ are determined by substituting for the vevs $v_{Y,I}$ in Eq. (140), *viz.*

$$\begin{aligned}
0 &= (m_{H_u}^2+\mu^2)v_u-B_\mu v_d+\frac{1}{8}(g'^2+g^2)(v_u^2-v_d^2)v_u+\frac{1}{2}(\lambda_Y^2+\lambda_I^2)v_uv_d^2\\
&\quad +(\sqrt{2}\lambda_Y\mu+g'M_Y^D)v_Yv_u+(\sqrt{2}\lambda_I\mu-gM_I^D)v_Iv_u\\
&\quad -\frac{1}{\sqrt{2}}(M_Y+A_Y)\lambda_Yv_Yv_d-\frac{1}{\sqrt{2}}(M_I+A_I)\lambda_Iv_Iv_d+\frac{1}{2}(\lambda_Yv_Y+\lambda_Iv_I)^2v_u, \qquad (143)\\
0 &= (m_{H_d}^2+\mu^2)v_d-B_\mu v_u-\frac{1}{8}(g'^2+g^2)(v_u^2-v_d^2)v_d+\frac{1}{2}(\lambda_Y^2+\lambda_I^2)v_u^2v_d\\
&\quad +(\sqrt{2}\lambda_Y\mu-g'M_Y^D)v_Yv_d+(\sqrt{2}\lambda_I\mu+gM_I^D)v_Iv_d\\
&\quad -\frac{1}{\sqrt{2}}(M_Y+A_Y)\lambda_Yv_Yv_u-\frac{1}{\sqrt{2}}(M_I+A_I)\lambda_Iv_Iv_u+\frac{1}{2}(\lambda_Yv_Y+\lambda_Iv_I)^2v_d, \qquad (144)
\end{aligned}$$

The values of $v_{u,d}$ and v_I can be determined phenomenologically in terms of the observables $\tan\beta$ and m_W^2, m_Z^2 *vide* Eqs. (76) and (77).

The terms in the Lagrangian which are bilinear in the fields build-up the scalar/Higgs mass matrices. Decomposing the neutral fields into ground-state values, real and imaginary parts,

$$\begin{aligned}
H_u^0 &= \frac{1}{\sqrt{2}}\left[s_\beta(v+h)+c_\beta H+i(c_\beta A-s_\beta a)\right], \qquad H_u^+=c_\beta\,H^+-s_\beta\,a^+, \qquad (145)\\
H_d^0 &= \frac{1}{\sqrt{2}}\left[c_\beta(v+h)-s_\beta H+i(s_\beta A+c_\beta a)\right], \qquad H_d^-=s_\beta\,H^-+c_\beta\,a^-, \qquad (146)
\end{aligned}$$

and

$$\begin{aligned}
\sigma_Y &= \frac{1}{\sqrt{2}}(v_Y+s_Y+ia_Y), \qquad (147)\\
\sigma_I^3 &= \frac{1}{\sqrt{2}}(v_I+s_I+ia_I), \quad \sigma_I^1=\frac{1}{\sqrt{2}}(\sigma_2^++\sigma_1^-), \quad \sigma_I^2=\frac{i}{\sqrt{2}}(\sigma_2^+-\sigma_1^-), \qquad (148)
\end{aligned}$$

it can be ascertained that the matrix of the imaginary fields involves a massless Goldstone field a, and likewise the charged fields involve $a_G^\pm = [va^\pm + \sqrt{2}v_I(\sigma_1^\pm + \sigma_2^\pm)]/\sqrt{v^2+4v_I^2}$. These are absorbed to provide masses to the neutral and charged gauge bosons. The remaining elements describe the pseudoscalar 3×3 mass matrix, the scalar 4×4 mass matrix and the charged 3×3 mass matrix:

1) Pseudoscalars

In the $\{A, a_Y, a_I\}$ basis, the 3×3 real and symmetric pseudoscalar mass matrix squared is given by

$$\mathcal{M}_P^2 = \begin{pmatrix} M_A^2 & -\frac{1}{\sqrt{2}}(M_Y - A_Y)\lambda_Y v & -\frac{1}{\sqrt{2}}(M_I - A_I)\lambda_I v \\ -\frac{1}{\sqrt{2}}(M_Y - A_Y)\lambda_Y v & \tilde{m}_Y'^2 & \frac{1}{2}\lambda_Y\lambda_I v^2 \\ -\frac{1}{\sqrt{2}}(M_I - A_I)\lambda_I v & \frac{1}{2}\lambda_Y\lambda_I v^2 & \tilde{m}_I'^2 \end{pmatrix}, \tag{149}$$

where

$$\tilde{m}_Y'^2 = m_Y^2 - m_Y'^2 + M_Y^2 + \tfrac{1}{2}\lambda_Y^2 v^2\,, \tag{150}$$

$$\tilde{m}_I'^2 = m_I^2 - m_I'^2 + M_I^2 + \tfrac{1}{2}\lambda_I^2 v^2\,. \tag{151}$$

The above can easily be diagonalized in approximate form in the limit of the genuine supersymmetry parameters, $m_{Y,I}$ being much larger than the electroweak scale v, i.e. $v/m_{Y,I} \ll 1$. This leaves us with an approximately unmixed state of mass

$$\overline{M}_{a_1}^2 \approx M_A^2 \tag{152}$$

and a 2×2 mass matrix in the $\{a_Y, a_I\}$ basis with two eigenvalues and the mixing angle given approximately by

$$\overline{M}_{a_2}^2 = \frac{1}{2}\left[\tilde{m}_Y'^2 + \tilde{m}_I'^2 - \sqrt{(\tilde{m}_Y'^2 - \tilde{m}_I'^2)^2 + \lambda_Y^2\lambda_I^2 v^4}\right] \approx \tilde{m}_Y'^2 - \frac{\lambda_Y^2\lambda_I^2 v^4}{4(\tilde{m}_I'^2 - \tilde{m}_Y'^2)}, \tag{153}$$

$$\overline{M}_{a_3}^2 = \frac{1}{2}\left[\tilde{m}_Y'^2 + \tilde{m}_I'^2 + \sqrt{(\tilde{m}_Y'^2 - \tilde{m}_I'^2)^2 + \lambda_Y^2\lambda_I^2 v^4}\right] \approx \tilde{m}_I'^2 + \frac{\lambda_Y^2\lambda_I^2 v^4}{4(\tilde{m}_I'^2 - \tilde{m}_Y'^2)}, \tag{154}$$

$$\tan\theta_a = \frac{2\,(\overline{M}_{a_2}^2 - \tilde{m}_Y'^2)}{\lambda_Y\lambda_I v^2}\,, \tag{155}$$

where the approximate relations hold whenever the off-diagonal terms are smaller than the difference of the diagonal ones.

2) Scalar

In the $\{h, H, s_Y, s_I\}$ basis, the real and symmetric 4×4 scalar mass matrix squared $\mathcal{M}_S^2$

is given by

$$\mathcal{M}_S^2 = \begin{pmatrix} m_Z^2+\delta_H s_{2\beta} & \delta_H c_{2\beta} & -\frac{v_Y}{v}(2\tilde{m}_Y^2-\lambda_Y^2 v^2) & -\frac{v_I}{v}(2\tilde{m}_I^2-\lambda_I^2 v^2) \\ \delta_H c_{2\beta} & M_A^2-\delta_H s_{2\beta} & \Delta_Y & \Delta_I \\ -\frac{v_Y}{v}(2\tilde{m}_Y^2-\lambda_Y^2 v^2) & \Delta_Y & \tilde{m}_Y^2 & \frac{1}{2}\lambda_Y\lambda_I v^2 \\ -\frac{v_I}{v}(2\tilde{m}_I^2-\lambda_I^2 v^2) & \Delta_I & \frac{1}{2}\lambda_Y\lambda_I v^2 & \tilde{m}_I^2 \end{pmatrix}, \tag{156}$$

where

$$\delta_H = (\lambda_Y^2+\lambda_I^2)v^2 - 2m_Z^2\,, \tag{157}$$

$$\Delta_Y = g' M_Y^D v\, s_{2\beta} - \tfrac{1}{\sqrt{2}}\lambda_Y(M_Y+A_Y)v\, c_{2\beta}\,, \tag{158}$$

$$\Delta_I = -g M_I^D v\, s_{2\beta} - \tfrac{1}{\sqrt{2}}\lambda_I(M_I+A_I)v\, c_{2\beta}\,. \tag{159}$$

Note that δ_H vanishes in the $N=2$ SUSY limit. Thus, in this limit, the eigenvalues of the Higgs submatrix $\{h,H\}$ are just m_Z^2 and M_A^2 [58], with no dependence on $\tan\beta$, a feature markedly different from the MSSM. This submatrix receives several radiative corrections, the most important one accruing from stop/top loops, a result of their large Yukawa couplings. The sigma couplings, on the other hand, remain of the order of the electroweak couplings. As a result, the Higgs submatrix is modified to

$$\begin{pmatrix} m_Z^2+\delta_H s_{2\beta} & \delta_H c_{2\beta} \\ \delta_H c_{2\beta} & M_A^2-\delta_H s_{2\beta} \end{pmatrix} \to \begin{pmatrix} m_Z^2+\delta_H s_{2\beta}+\epsilon_H & \delta_H c_{2\beta}+\epsilon_H/t_\beta \\ \delta_H c_{2\beta}+\epsilon_H/t_\beta^2 & M_A^2-\delta_H s_{2\beta}+\epsilon_H/t_\beta \end{pmatrix}, \tag{160}$$

where

$$\epsilon_H \simeq \frac{3G_F m_t^4}{\sqrt{2}\pi^2}\ln\frac{m_{\tilde{t}_1}m_{\tilde{t}_2}}{m_t^2}\,. \tag{161}$$

The transition from the current basis to the diagonal 2×2 Higgs matrix with eigenvalues

$$\overline{M}_{S_1}^2 \approx m_Z^2+\delta_H s_{2\beta}+\epsilon_H - \frac{(\delta_H c_{2\beta}+\epsilon_H/t_\beta)^2}{M_A^2-m_Z^2}\,, \tag{162}$$

$$\overline{M}_{S_2}^2 \approx M_A^2-\delta_H s_{2\beta}+\epsilon_H/t_\beta^2 + \frac{(\delta_H c_{2\beta}+\epsilon_H/t_\beta)^2}{M_A^2-m_Z^2}\,, \tag{163}$$

is carried out by the orthogonal transformation $\mathcal{O}_{hh}$ with the mixing element given by

$$\tan\alpha_h = \frac{\overline{M}_{S_1}^2 - m_Z^2-\delta_H s_{2\beta}-\epsilon_H}{\delta_H c_{2\beta}+\epsilon_H/t_\beta}\,. \tag{164}$$

Equally straightforward is the diagonalization of the $\{s_Y, s_I\}$ submatrix leading to the two eigenvalues

$$\overline{M}_{S_3}^2 \approx \tilde{m}_Y^2 - \frac{\lambda_Y^2\lambda_I^2 v^4}{4(\tilde{m}_I^2-\tilde{m}_Y^2)}\,, \tag{165}$$

$$\overline{M}_{S_4}^2 \approx \tilde{m}_I^2 + \frac{\lambda_Y^2\lambda_I^2 v^4}{4(\tilde{m}_I^2-\tilde{m}_Y^2)}\,, \tag{166}$$

the diagonalization carried out by an orthogonal transformation with the mixing element

$$\tan\alpha_s = \frac{2\,(\overline{M}^2_{S_3} - \tilde{m}^2_Y)}{\lambda_Y \lambda_I v^2}\,. \tag{167}$$

3) Charged scalars:
After the charged Goldstone bosons $a^\pm_G$ are absorbed into the charged gauge bosons, there remain three physical charged scalar states $\{H^\pm, s^\pm_1, s^\pm_2\}$ with the second and third states defined by

$$s^\pm_1 = (\sigma^\pm_1 - \sigma^\pm_2)/\sqrt{2} \quad \text{and} \quad s^\pm_2 = \frac{v(\sigma^\pm_1 + \sigma^\pm_2)/\sqrt{2} - 2v_I a^\pm}{\sqrt{v^2 + 4v^2_I}}\,. \tag{168}$$

The real symmetric 3×3 charged scalar mass matrix squared $\mathcal{M}^2_{H^\pm}$ is then given in the $\{H^\pm, s^\pm_1, s^\pm_2\}$ basis by

$$\mathcal{M}^2_{H^\pm} = \begin{pmatrix} \tilde{M}^2_{H^\pm} & \Delta_\pm & -\sqrt{\rho}\,\Delta_I \\ \Delta_\pm & \tilde{m}'^2_I + g^2 v^2_I & \frac{1}{2}\sqrt{\rho}\left(\lambda^2_I - \frac{1}{2}g^2\right) v^2 c_{2\beta} \\ -\sqrt{\rho}\,\Delta_I & \frac{1}{2}\sqrt{\rho}\left(\lambda^2_I - \frac{1}{2}g^2\right) v^2 c_{2\beta} & \rho\,\tilde{m}^2_I \end{pmatrix}, \tag{169}$$

where

$$\tilde{M}^2_{H^\pm} = M^2_A + m^2_W + \frac{1}{2}(\lambda^2_I - \lambda^2_Y)v^2 - 4\frac{v^2_I}{v^2}\tilde{m}^2_I + 4\lambda^2_I v^2_I - 4\sqrt{2}\mu_n \lambda_I v_I\,, \tag{170}$$

$$\Delta_\pm = \left(g^2/2 - \lambda^2_I\right) v_I v s_{2\beta} - (M_I - A_I)\lambda_I v/\sqrt{2}\,, \tag{171}$$

the rho parameter $\rho = 1 + 4v^2_I/v^2$ and Δ_I in Eq. (159).

Assuming that $\tilde{m}^2_I > \tilde{m}'^2_I > \tilde{M}^2_{H^\pm}$ and $M_I, A_I \sim M_A$, and observing that, again, the charged Higgs and scalar states are weakly coupled at the order of $v/\tilde{m}_I$ or $v/\tilde{m}'_I$, the block-diagonalization procedure provides approximate solutions.

The extension of the Higgs sector by the novel $\mathrm{SU}(2)_I \times \mathrm{U}(1)_Y$ adjoint sigma fields has two important consequences:

- Each of the pseudoscalar, scalar and charged sectors are extended by two new states with masses of the order of the characteristic scalar parameters M_Y and M_I. As a result, one of the new pseudoscalar/scalar states may acquire mass between a few hundred GeV up to a TeV, while the other will be heavy, i.e., $\mathcal{O}(\mathrm{TeV})$; both the new charged states will be heavy likewise.

- The mass matrix of the Higgs system is modified compared to the MSSM. As pointed out before, the tree-level Higgs masses are independent of the mixing parameter $\tan\beta$, and the lower bound on the (lightest) charged Higgs mass is not guaranteed to exceed the W mass anymore.

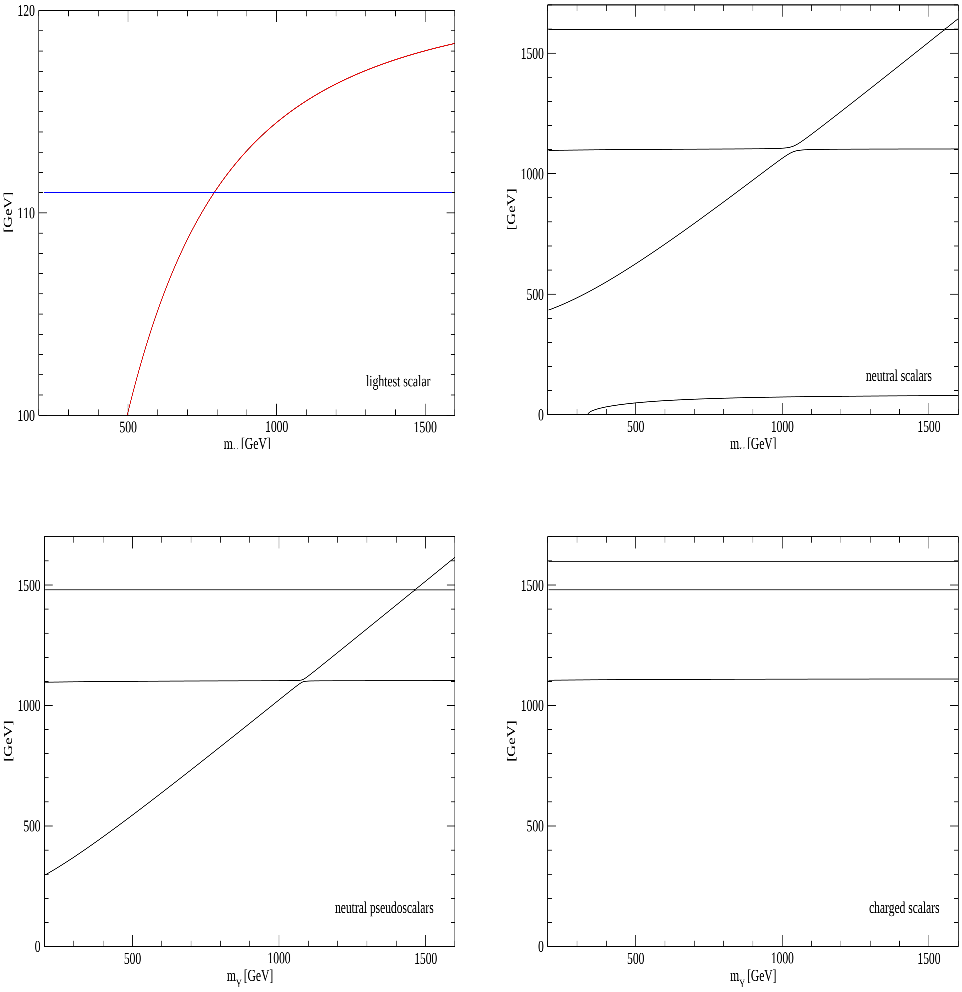

Figure 18: (a) The lightest neutral scalar boson including one-loop top/stop radiative corrections. The blue line indicates the present experimental lower bound (with the theoretical errors) on the mass $M_{S_1} \gtrsim 111$ GeV; (b) the neutral scalar masses; (c) the pseudoscalar masses; (d) the charged scalar masses, as a function of the hyper-charge soft scalar mass m_Y; the isospin soft scalar mass is set to $m_I = 6v$ to accommodate the small ρ-parameter. The other parameters are fixed to $\tan\beta = 5$, $m_{\tilde{t}_1} = 1\,TeV$, $\mu = 3v$, $m'_Y = M^D_Y = v/2$, $m'_I = M^D_I = v$, $A_Y = A_I = 2v$ and $M_Y = M_I = m_{H_u} = m_{H_d} = v$.

The Fig. 18 illustrates the evolution of the three pseudoscalar, four scalar, and three charged masses with the hyper-singlet mass parameter m_Y introduced on the third line of Eq. (36) while all other parameters are kept fixed. These parameters have been chosen as indicated in the figure caption.

σ production

1) Neutral adjoint scalar

(i) Stop decays

Sigma fields carry positive R-parity, but they couple preferentially to gaugino and squark/slepton pairs. Assuming, as before, that they are heavier than charginos and neutralinos, this leaves us with stop decays as a possible source for neutral sigma particles:

$$\tilde{t}_2 \quad \rightarrow \quad \tilde{t}_1 + s_Y \, , \tag{172}$$

while the s_I channel is likely too heavy to be open. The partial width for this decay mode is given by

$$\Gamma_{\tilde{t}_2} = \frac{g_{\tilde{t}}^2}{16\pi \, m_{\tilde{t}_2}} \lambda^{1/2}(1, m^2_{\tilde{t}_1}/m^2_{\tilde{t}_2}, M^2_{s_Y}/m^2_{\tilde{t}_2}) \, , \tag{173}$$

with λ denoting the usual phase space function defined in (121) and the coupling

$$g_{\tilde{t}} = \frac{5}{6\sqrt{2}} \, g' M_Y^D \, \sin 2\theta_{\tilde{t}}. \tag{174}$$

$\Gamma_{\tilde{t}}$ is typically of order GeV.

If the on-shell decay is not allowed kinematically, the next possible mode is the decay $\tilde{t}_2$ to a top quark, a lightest neutralino $\tilde{\chi}^0_1$ and s_Y, mediated by a virtual $\tilde{t}_1^\star$:

$$\tilde{t}_2 \quad \rightarrow \quad \tilde{t}_1^\star + s_Y \quad \rightarrow \quad t + \chi^0_1 + s_Y \, . \tag{175}$$

Denoting the chiral $\tilde{t}_1 t \tilde{\chi}^0_1$ couplings by g_L, g_R, i.e.,

$$g_L \quad = \quad -\sqrt{2} g \, [\, (\frac{1}{2} U^*_{N_{4j}} + \frac{1}{6} \tan\theta_W U^*_{N_{2j}}) \cos\theta_{\tilde{t}} + \frac{m_t}{2 m_W \sin\beta} U^*_{N_{6j}} \sin\theta_{\tilde{t}} \,] \, , \tag{176}$$

$$g_R \quad = \quad \sqrt{2} g \, [\, \frac{2}{3} \tan\theta_W U_{N_{2j}} \sin\theta_{\tilde{t}} - \frac{m_t}{2 m_W \sin\beta} U_{N_{6j}} \cos\theta_{\tilde{t}} \,] \, , \tag{177}$$

the partial width of the three-body decay (175) given by

$$\Gamma_{\tilde{t}_2} = \frac{g^2_{\tilde{t}}}{256\pi^3 m_{\tilde{t}_2}} \int_{(m_t + m_{\tilde{\chi}^0_1})^2}^{(m_{\tilde{t}_2} - M_{s_Y})^2} dM^2 \, \frac{K[M^2] \, \lambda(1, M^2/m^2_{\tilde{t}_2}, M^2_{s_Y}/m^2_{\tilde{t}_2}) \lambda(1, m_t^2/M^2, m^2_{\tilde{\chi}^0_1}/M^2)}{(M^2 - m^2_{\tilde{t}_1})^2 + m^2_{\tilde{t}_1} \Gamma^2_{\tilde{t}_1}} \, , \tag{178}$$

with $K[M^2] = (g_L^2 + g_R^2)(M^2 - m_t^2 - m^2_{\tilde{\chi}^0_1}) - 4 g_L g_R m_t m_{\tilde{\chi}^0_1}$ becomes rapidly much smaller than the standard $\tilde{t}_2$ decay width when M_{s_Y} exceeds the mass difference $m_{\tilde{t}_2} - m_{\tilde{t}_1}$ by an amount of a few times the total $\tilde{t}_2$ width. The branching ratio then becomes too small for $\tilde{t}_2$ decays to become a source of s_Y particles.

(ii) Gluon fusion

The neutral hyper-singlet and iso-triplet scalar particles s_Y and s_I can be generated singly in gluon fusion processes at the LHC:

$$pp \quad \to \quad gg \quad \to \quad s_{Y,I} \,. \tag{179}$$

The adjoint scalar coupling to the gluons are mediated by squark triangles, the D-terms providing the interactions of the squarks with the sigma fields. The partonic fusion cross section of s_Y production, with the Breit-Wigner function in units of $1/M^2_{s_Y}$ factored off,

$$\hat{\sigma}(gg \to s_Y) = \frac{\pi^2}{8M_{s_Y}} \Gamma(s_Y \to gg) \,, \tag{180}$$

can be expressed by the partial width for $s_Y \to gg$,

$$\Gamma(s_Y \to gg) = \frac{\alpha_Y \alpha_s^2}{8\pi^2} \frac{(M_a^D)^2}{M_{s_Y}} \left| \sum [Y_L \tau_L f(\tau_L) - Y_R \tau_R f(\tau_R)] \right|^2 \,. \tag{181}$$

with $\alpha_Y = g'^2/4\pi$. The standard triangular function is denoted by $f(\tau)$ defined in Eq. (65), with $\tau_{L,R} = 4M^2_{\tilde{q}_{L,R}}/M^2_{s_Y}$ and $Y_{L,R}$ being the hyper-charges of the L and R-squarks. It should be noted that the hyper-charges add up to zero for complete generations, but not individually for up- and down-type states for which the L/R hyper-charge difference amounts to ∓ 1. While for mass-degenerate complete generations the sum of the form factors in the partial width vanishes, the cancelation is lifted for stop states, in particular, with the non-zero difference enhanced by the different L/R hyper-charges.

The pp cross section is finally found by convoluting the parton cross section with the gg luminosity,

$$\sigma(pp \to s_Y) = \frac{\pi^2}{8s} \frac{\Gamma(s_Y \to gg)}{M_{sY}} \int_\tau^1 \frac{dx}{x}\, g(x; M^2_{sY})\, g(\tau/x; M^2_{sY}) \,, \tag{182}$$

in the usual notation. The cross section for s_Y production is shown in Fig. 19 as a function of the s_Y mass; similar results are obtained for s_I production. As expected, the size of the fusion cross section is small.

2) Charged adjoint scalar

(i) e^-e^- collisions

Single production of sigma particles in e^+e^- collisions is strongly suppressed as the production amplitude scales with the electron mass. Since the quantum numbers Q, I_3, Y of the neutral sigma states $\sigma^0_{I,Y}$ all vanish, these particles cannot be pair-produced in e^+e^- collisions. However, production channels open up for diagonal charged scalar pairs $s^\pm_{1,2}$ defined in Eq. (168),

$$e^+e^- \quad \to \quad s_n^+ s_n^- \quad , n = 1, 2 \,, \tag{183}$$

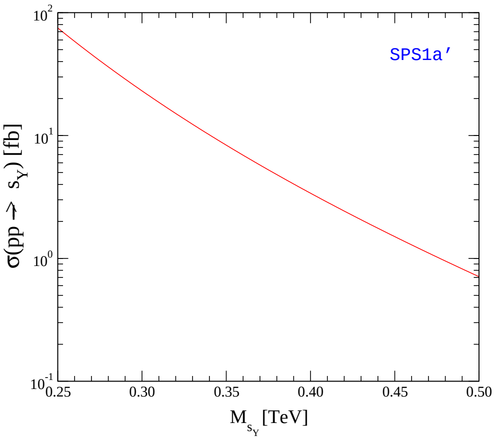

Figure 19: Cross sections for single s_Y production through gg fusion in pp collisions at LHC ($\sqrt{s} = 14$TeV). The MSSM benchmark point $SPS1a'$ is adopted for the numerical analysis.

through s-channel γ, Z exchanges. With effective charges

$$g_{L*}[s_n^\pm] = 1 - \frac{s_W^2 - 1/2}{s_W^2}\frac{s}{s - m_Z^2} \approx 2\,, \quad g_{R*}[s_n^\pm] = 1 - \frac{s}{s - m_Z^2} \approx 0\,, \tag{184}$$

$$g_{L*}[H^\pm] = 1 + \frac{(s_W^2 - 1/2)^2}{c_W^2 s_W^2}\frac{s}{s - m_Z^2} \approx \frac{4}{3}\,, \quad g_{R*}[H^\pm] = 1 + \frac{s_W^2 - 1/2}{c_W^2}\frac{s}{s - m_Z^2} \approx \frac{2}{3} \tag{185}$$

with $n = 1, 2$ for L and R-chiral electron pairs coupled to the $s_{1,2}^\pm$ pairs and equivalently to the $H^\pm$ pair, the cross section reads:

$$\sigma = \frac{\pi\alpha^2}{3s}\frac{g_{L*}^2 + g_{R*}^2}{2}\,\beta^3\,, \tag{186}$$

where s is the total c.m. energy squared and β the velocity of the particles $s_{1,2}^\pm$ and $H^\pm$; $s_W^2 = \sin^2\theta_W$ denotes the electroweak mixing parameter. The size of the three production cross sections, identical in form, is illustrated in Fig. 20 for the two different mass values $M_{s_1^\pm, H^\pm} = 0.5$TeV and $M_{s_2^\pm} = 1$TeV.

(ii) $\gamma\gamma$ collisions

Excellent instruments for searching for heavy scalar/pseudoscalar particles and studying their properties are $\gamma\gamma$ colliders [60]. About 80% of the incoming electron energy can be converted to a high-energy photon by Compton back-scattering of laser light, with the spectrum peaking at the maximal energy by choosing proper helicities.

Depending on the nature of the scalars/pseudoscalars their couplings to the two photons is mediated by charged W-bosons, charginos, and charged scalars and Higgs bosons. As before, the formation cross sections can be expressed by the $\gamma\gamma$ widths of the particles

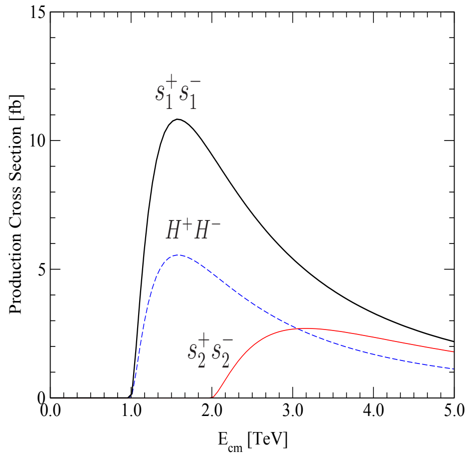

Figure 20: The cross sections for charged $s_{1,2}^{\pm}$ pair production in e^+e^- collisions at TeV energies. The charged scalar masses are assumed to be $M_{\tilde{s}_1^\pm} = 0.5$TeV and $M_{\tilde{s}_2^\pm} = 1$TeV. For comparison, the cross section for charged Higgs pair production is shown with its mass $M_{H^\pm} = 0.5$TeV.

and the $\gamma\gamma$ luminosity:

$$\langle \sigma(\gamma\gamma \to \phi) \rangle \;=\; 8\pi^2 \, \frac{\Gamma(\phi \to \gamma\gamma)}{M_\phi^3} \, \tau_\phi \frac{d\mathcal{L}_{\gamma\gamma}}{\tau_\phi} \;\equiv\; \sigma_0(\gamma\gamma \to \phi) \, \tau_\phi \frac{d\mathcal{L}_{\gamma\gamma}}{\tau_\phi} \, , \tag{187}$$

with $\tau_\phi = M_\phi^2/s$. For qualitative estimates the luminosity function $\tau d\mathcal{L}/d\tau$ can be approximated by unity after splitting off the overall e^+e^- luminosity[61].

The partial $\gamma\gamma$ widths are parameterized by couplings and loop functions,

$$\Gamma(s/a \to \gamma\gamma) = \frac{\alpha^2}{64\pi^3} \, M_{s/a} \left| \sum_i N_{c_i} e_i^2 g_i^{s/a} A_i^{s/a} \right|^2 . \tag{188}$$

The factor N_{c_i} denotes the color factor of the loop line; the couplings $g_i^{s/a}$ are expressed by the quantum numbers,

$$\begin{aligned}
& g^{s_Y}_{\tilde{H}_D^\pm} = \lambda_Y/\sqrt{2} \, , \quad g^{s_Y}_{\tilde{f}_{L,R}} = \pm Y_{f_{L,R}} M_Y^D / M_{s_Y} \, , \\
& g^{s_Y}_{H^\pm} = \left(\sqrt{2} \lambda_Y \mu_c - g' M_Y^D c_{2\beta} + \lambda_Y (M_Y + A_Y) s_{2\beta}/\sqrt{2} \right) / M_{s_Y} \, , && (189) \\
& g^{s_I}_{W^\pm} = 2 g^2 v_I / M_{s_I} \, , \quad g^{s_I}_{\tilde{H}_D^\pm} = \lambda_I/\sqrt{2} \, , \quad g^{s_I}_{\tilde{W}^\pm_{1,2}} = \mp g \, , \quad g^{s_I}_{\tilde{f}_{L,R}} = \pm g I_3^f M_I^D / M_{s_I} , \\
& g^{s_I}_{H^\pm} = - \left(\sqrt{2} \lambda_I \mu_c - g M_I^D c_{2\beta} + \lambda_I (M_I - A_I) s_{2\beta}/\sqrt{2} \right) / M_{s_I} , && (190)
\end{aligned}$$

for the hyper-singlet scalar s_Y, and

$$g^{a_Y}_{\tilde{H}_D^\pm} = -\lambda_Y/\sqrt{2}, \tag{191}$$

$$g^{a_I}_{\tilde{H}_D^\pm} = \lambda_I/\sqrt{2}, \quad g^{a_I}_{\tilde{W}^\pm_{1,2}} = \pm g \, , \tag{192}$$

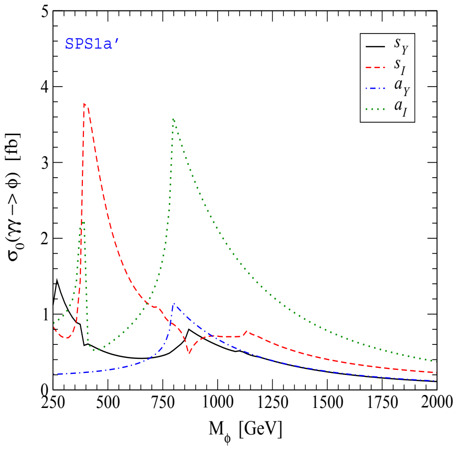

Figure 21: The reduced production cross sections $\sigma_0(\gamma\gamma \to \phi)$ for $\phi = s_{Y,I}$ and $a_{Y,I}$. The SPS1a′ parameter set [54] for the (s)particle masses, couplings and mixing parameters are adopted for the numerical analysis.

for the hyper-singlet pseudoscalar a_Y, while the loop functions $A_i^{s/a}$, identical in form for the particles of a given spin, include the standard triangular function $f(\tau)$ in Eq. (65) as:

$$A_0^s = 1 - \tau f(\tau)\,, \quad A_{1/2}^s = -2\sqrt{\tau}\,[1 + (1-\tau) f(\tau)]\ , \tag{193}$$

$$A_1^s = 2/\tau + 3 + 3(2-\tau) f(\tau)\,; \quad A_{1/2}^a = -2\sqrt{\tau} f(\tau)\,. \tag{194}$$

where the subscripts $0, 1/2$ and 1 stand for spin-0, spin-1/2 and spin-1 intermediate particles.

Adopting the SPS1a′ parameters in the SUSY sector [54], the reduced $\gamma\gamma$ cross section $\sigma_0(\gamma\gamma \to \phi)$ for $\phi = s_{Y,I}$ and $a_{Y,I}$, defined in Eq. (187), amounts to about 1 fb as shown in Fig. 21 so that for an overall luminosity of several hundred fb^{-1} a large sample of neutral scalars $s_{Y,I}$ and pseudoscalars $a_{Y,I}$ can be generated in $\gamma\gamma$ collisions.

σ *decays*

Expressed by the couplings $g_{B,F}$ in the Lagrangians $\mathcal{L} = g_B\, s\, B^* B$ and $\mathcal{L} = g_F\, s/a\, \bar{F}[i\gamma_5]F$, the partial decay widths can be derived generically for bosons B and fermions F as

$$\Gamma[s \to B\bar{B}] \quad = \quad \frac{g_B^2}{16\pi m_{s/a}}\beta \tag{195}$$

$$\Gamma[s/a \to F\bar{F}] \quad = \quad \frac{g_F^2 m_{s/a}}{8\pi}\beta^3/\beta\,, \tag{196}$$

with β denoting the velocity of the final state particles. The two standard coefficients β and β^3 correspond to S and P-wave decays.

For unspecified masses and couplings the following decays are the leading modes of the particles s_Y and a_Y:

$$s_Y \;\to\; hh,\; hH,\; HH,\; AA,\; H^+H^-;\; \tilde{f}\tilde{f}^*;\; \tilde{\chi}^+\tilde{\chi}^-,\; \tilde{\chi}^0\tilde{\chi}^{0(c)}\,, \tag{197}$$

$$a_Y \;\to\; \tilde{\chi}^+\tilde{\chi}^-,\; \tilde{\chi}^0\tilde{\chi}^{0(c)}\,. \tag{198}$$

The pseudoscalar particle a_Y decays only to (higgsino-type) neutralino or chargino pairs, with equal probability sufficiently above the threshold region. If 2-body decays are kinematically forbidden, 3-body decays to a (higgsino-type) neutralino, (bino-type) neutralino and Higgs boson, as well as loop-decays to $t\bar{t}$ pairs and photons are predicted. It should also be noted that the mass eigenstate, A_2, may decay through channels opened by the mixing with the pseudoscalar A Higgs boson. As the couplings are of size $\mathcal{O}(g' M_Y^D)$ and/or $\mathcal{O}(\lambda_Y \mu, \lambda_Y M_Y, \lambda_Y A_Y)$, the ensuing partial widths are typically of electroweak size above the 2-body threshold regions.

A detailed set of leading decay branching ratios is shown for the hyper-singlet scalar particle s_Y in Fig. 22. The relevant couplings g_B and g_F for the scalar s_Y to Higgs bosons are:

$$g_B[s_Y hh] = -\sqrt{2}\lambda_Y \mu_n + g' M_Y^D c_{2\beta} + (M_Y + A_Y)\lambda_Y s_{2\beta}/\sqrt{2}\,, \tag{199}$$

$$g_B[s_Y hH] = -g' M_Y^D s_{2\beta} + (M_Y + A_Y)\lambda_Y c_{2\beta}/\sqrt{2}\,, \tag{200}$$

$$g_B[s_Y HH] = g_B[s_Y AA] = -\sqrt{2}\lambda_Y \mu_n - g' M_Y^D c_{2\beta} - (M_Y + A_Y)\lambda_Y s_{2\beta}/\sqrt{2} \tag{201}$$

$$g_B[s_Y H^+H^-] = -\sqrt{2}\lambda_Y \mu_c + g' M_Y^D c_{2\beta} - (M_Y + A_Y)\lambda_Y s_{2\beta}/\sqrt{2}\,, \tag{202}$$

and those to supersymmetric particles are:

$$g_B[s_Y \tilde{f}_L \tilde{f}_L^*] = -2g' M_Y^D Y_{f_L}\,, \tag{203}$$

$$g_B[s_Y \tilde{f}_R \tilde{f}_R^*] = 2g' M_Y^D Y_{f_R}\,, \tag{204}$$

$$g_F[s_Y \tilde{H}_u^+ \tilde{H}_d^-] = g_F[s_Y \tilde{\chi}_{D3}^+ \tilde{\chi}_{D3}^-] = -\lambda_Y/\sqrt{2}\,, \tag{205}$$

$$g_F[s_Y \tilde{H}_u^0 \tilde{H}_d^0] = -g_F[s_Y \tilde{\chi}_{D3}^0 \tilde{\chi}_{D3}^{0c}] = \lambda_Y/\sqrt{2}\,, \tag{206}$$

and the relevant couplings for the pseudoscalar a_Y are:

$$g_F[a_Y \tilde{H}_u^+ \tilde{H}_d^-] = g_F[a_Y \tilde{\chi}_{D3}^+ \tilde{\chi}_{D3}^-] = \lambda_Y/\sqrt{2}\,, \tag{207}$$

$$g_F[a_Y\, \tilde{H}_u^0\, \tilde{H}_d^0\,] = -g_F[a_Y \tilde{\chi}_{D3}^0 \tilde{\chi}_{D3}^{0c}] = -\lambda_Y/\sqrt{2}\,. \tag{208}$$

The Dirac chargino and neutralino, $\tilde{\chi}_{D3}^\pm$ and $\tilde{\chi}_{D3}^0$, are defined in terms of higgsinos in Eqs. (96) and (99), respectively. For the specific set of parameters the hyper-singlet scalar s_Y decays dominantly to Higgs bosons and sleptons. The decays to gaugino-like neutralinos are forbidden due to gauge symmetry and the decays to higgsino-like neutralinos and charginos are kinematically allowed only when the particle is very heavy.

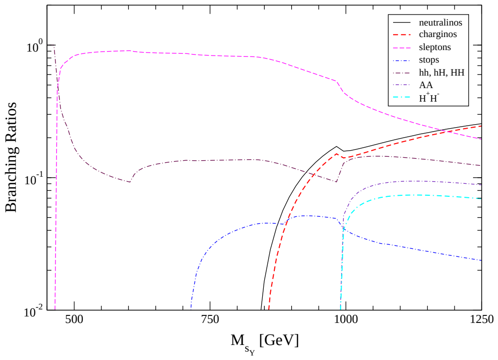

Figure 22: Dependence of the decay ranching ratios for the s_Y state on its mass M_{s_Y}. The values of the relevant SUSY parameters are taken to be tanβ=5, $\mu = 400$GeV, $m'_Y = M^D_Y = v/2$, $m'_I = M^D_I = v$, $A_Y = A_I = 2v$, together with $m_{\tilde{l}} = v$, $m_{\tilde{e}_R} = 0.95 m_{\tilde{l}}$, $m_{\tilde{q}} = 2v$, $m_{\tilde{q}_R} = 0.95 m_{\tilde{q}}$, $m_{\tilde{t}_R} = 0.8 m_{\tilde{q}}$, $m_{\tilde{t}_L} = X_t = 0.9 m_{\tilde{q}}$, $m_H = m_A = m^{\pm}_H = 2v$, $m_h = 114$GeV. For the charginos and neutralinos the Dirac limit with $M^{(\prime)}_{1,2} = 0$ is assumed.

The iso-triplet scalar states, s_I, a_I and $s^{\pm}_{1,2}$, have been assumed very heavy. Several features of the iso-triplet scalar interactions determine the potential of their decay modes. In parallel to the hyper-charge states, they do not couple to quarks and leptons, but they couple to higgsinos, gauginos and scalar pairs, sfermions as well as Higgs bosons and/or gauge bosons. Thus, if kinematically allowed, the gauge/Higgs bosons, sfermions, charginos and neutralinos constitute the dominant decay channels for the s_I, a_I and $s^{\pm}_{1,2}$ states:

$$s_I \;\rightarrow\; W^+W^-;\;\; hh,\;\; hH,\;\; HH,\;\; AA,\;\; H^+H^-;\;\; \tilde{f}\tilde{f}^*;\;\; \tilde{\chi}^+\tilde{\chi}^-,\;\; \tilde{\chi}^0\tilde{\chi}^{0(c)}\,, \tag{209}$$

$$a_I \;\rightarrow\; \tilde{\chi}^+\tilde{\chi}^-,\;\; \tilde{\chi}^0\tilde{\chi}^{0(c)}\,, \tag{210}$$

$$s^{\pm}_{1,2} \;\rightarrow\; H^{\pm}h,\;\; H^{\pm}H,\;\; H^{\pm}A;\;\; \tilde{f}\tilde{f}'^*;\;\; \tilde{\chi}^+\tilde{\chi}^0/\tilde{\chi}^-\tilde{\chi}^{0c}\,, \tag{211}$$

with partial widths of the electroweak scale. Furthermore, if all these decays were kinematically forbidden, the iso-triplet scalar states may still decay to gluons, photons, quarks and leptons mediated by sfermion and chargino/neutralino loops.

3 Dark Matter

As already mentioned in the Introduction, the lightest neutalino is often the LSP in the MSSM, a good candidate for the Dark Matter. It is electrically neutral, stable (protected from decays to the SM particles by the R-parity), and weakly interacting. Note that the last property is crucial for it to be produced in the thermal bath in the early Universe. Thus, we can compute its relic density as a function of its mass and couplings to the other particles, and compare it with the observation. Actually, even though the LSP is the best candidate for the Dark Matter, this is true for all weakly interacting massive particles (WIMPs).

In the first subsection, we show how to perform this calculation for the general WIMPs, firstly to the tree-level, and then including the one-loop corrections. The latter is required, as the precision of present cosmological data soon improves to a percent level, and in order to exploit it, the theoretical error on the prediction for the WIMP relic density should not exceed the error inferred from observations.

On the other hand, since the LSP is weakly interacting with the SM particles, using the specialized detectors, we might hope to obtain signals coming from them. This will be our topic in the Sec. 3.2. We will begin with the brief reviews on the general aspects of direct and indirect Dark Matter search experiments. Then we discuss the detectability of the neutralino Dark matter candidate by the near-future as well as current direct and indirect searches.

3.1 Dark Matter Relic Density

3.1.1 Standard Computation

In the early Universe, most of the particles had been in thermal equilibrium. Were they so to the present, there would be essentially no relics. Fortunately, the particle species decoupled from the thermal plasma at some point, i.e. the process that keeps the species in the thermal equilibrium started not to be frequent enough to overcome the expansion of the Universe ("freeze out"):

$$\Gamma \lesssim H, \tag{212}$$

where Γ is the interaction rate, and H is the Hubble parameter. In order to calculate the relic density of the LSP, we will use the Boltzmann equation with the Friedmann-Robertson-Walker metric:

$$\frac{dn}{dt} + 3\frac{\dot{R}}{R}n = \frac{g}{(2\pi)^3}\int C[f]\frac{d^3}{p}E, \tag{213}$$

where n is the number density of the relic, C is the collision operator and g is the degrees of freedom. With the assumption of CP invariance and Maxwell-Boltzmann statistics instead of Fermi-Dirac or Bose-Einstein, as well as of no asymmetry on charge conjugation, and the thermal distribution with zero chemical potential, the Boltzmann equation gets simplified as follows:

$$\frac{dn}{dt} + 3Hn = -\langle \sigma v \rangle [n^2 - (n^{eq})^2], \tag{214}$$

Here H is the Hubble parameter describing the expansion of the Universe, σ is the total WIMP annihilation cross section, v is again the relative velocity between the annihilating WIMPs in their center of mass frame, $n_{\chi,\mathrm{eq}}$ is the WIMP number density in thermal equilibrium, and $\langle \cdots \rangle$ denotes thermal averaging. The second term in the left hand side in the Eq. (214) comes from the dilution of the number density due to the expansion of the Universe.

For non–relativistic kinematics, the latter is given by

$$\langle \sigma v \rangle = \frac{2x^{3/2}}{\sqrt{\pi}} \int_0^\infty (\sigma v) \frac{v^2}{4} e^{-xv^2/4} dv \,, \tag{215}$$

where $x = m_\chi / T$, T being the temperature of the thermal bath.

As long as the WIMP annihilation (or creation) rate is larger than the Hubble expansion rate, the WIMPs are (almost) in thermal equilibrium. However, once the annihilation rate falls below the expansion rate, WIMPs nearly decouple. Their present relic density is then to very good approximation given by [67]

$$\Omega_\chi h^2 = \frac{8.5 \times 10^{-11} \, x_F \ \mathrm{GeV}^{-2}}{\sqrt{g_*(x_F)} J(x_F)} \,. \tag{216}$$

Here $x_F = m_\chi / T_F$, where T_F is the freeze–out temperature of the WIMPs, g_* is the number of relativistic degrees of freedom, and the annihilation integral $J(x_F)$ is defined as [67]

$$J(x_F) = \int_{x_F}^\infty dx \frac{\langle \sigma v \rangle}{x^2} \,. \tag{217}$$

The freeze–out temperature of typical WIMPs is rather small, $T_F \simeq m_\chi/20$, hence WIMPs are non–relativistic when they freeze out. This suggests an expansion of $\sigma_0 v$ in powers v [67]:

$$\sigma_0 v \simeq \mathscr{A} + \mathscr{B} v^2 + \cdots \,, \tag{218}$$

where $\mathscr{A}$ and $\mathscr{B}$ are independent of v. Note that $\mathscr{A}$ contains only $S-$wave contributions, while $\mathscr{B}$ contains both $S-$ and $P-$wave contributions.

The thermal average over the tree–level cross section, expanded according to Eq. (218), can be computed easily [67]:

$$\langle \sigma_0 v \rangle (x) \simeq \mathscr{A} + \frac{6\mathscr{B}}{x} \,. \tag{219}$$

When there is a particle whose mass is almost degenerate with that of the Dark matter, for instance, the NLSP in SUSY, then the annihilations with which that particle participate play an important role in calculating the relic density of Dark Matter.[62] With the constaints by some assumed symmetry such as the R-parity, the types of reactions which determine the abundances are as follows:

$$\begin{aligned} \chi_i\chi_j &\leftrightarrow ff' \quad (220)\\ \chi_i f &\leftrightarrow \chi_j f' \quad (221)\\ \chi_j &\leftrightarrow \chi_i f f', \quad (222)\end{aligned}$$

where χ_i's are the relics, with $m_i < m_j$, when $i < j$, and f, f' denote the SM particles. Summing over reactions of all particles to obtain the abundance of Dark Matter, and assuming that the ratio of the χ_i density to that of total χ maintains its equilibrium value,[13] the Eq. (214) becomes,

$$\frac{dn}{dt} = -3Hn - \langle \sigma_{eff} v \rangle (n^2 - n_{eq}^2), \quad (223)$$

with the effective cross section,

$$\sigma_{eff} = \sum_{i,j}^{N} \sigma_{ij} \frac{n_i^{eq} n_j^{eq}}{(n^{eq})^2}. \quad (224)$$

Often the significant modification occurs as long as the mass of the NLSP is within around 10% of that of LSP.

3.1.2 One-loop Corrections

In this subsection, we compute the relic density of cold Dark Matter including the one-loop corrections due to the exchange of a boson in the initial state. First we introduce the formalism, followed by the thermal averaging of the corrected cross section. Then we will show the examples.

1. Correction to the annihilation amplitudes

Consider the annihilation of two WIMPs χ into two SM particles:

$$\chi(p_1) + \chi(p_2) \to X_1(p_1') + X_2(p_2')\,. \quad (225)$$

Generic tree–level diagrams contributing to this process have the form shown in Fig. 23(a). We want to compute one–loop corrections of the kind shown in Fig. 23(b), where a boson φ is exchanged between the WIMPs before they annihilate, by adapting the formalism of Iengo [63, 64]. We assume that χ is a Majorana fermion; however, in the non–relativistic limit this will be relevant only for the case where the exchanged boson has axial vector couplings (see below).

---

[13] This is true when the first equation of the Eq. (220), which determines the freeze-out, is the slowest.

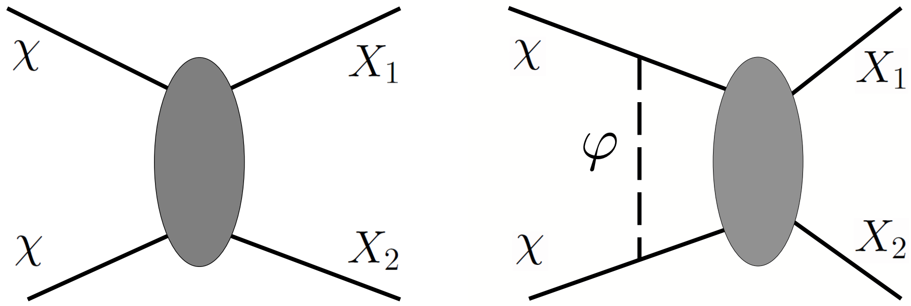

Figure 23: (a) Tree–level WIMP annihilation, (b) The one–loop corrections we consider. The grey blob represents the exchange of some particle in the $s-$, $t-$ or $u-$channel.

In this formalism φ exchange and χ annihilation are factorized; the former can then also be understood as re–scattering of the incoming WIMPs prior to their annihilation. This factorization (φ exchange before χ annihilation) is only expected to work in the non–relativistic limit. Moreover, it requires the virtuality of the φ propagator to be (much) smaller than that of the particle exchanged in χ annihilation. The latter can always be satisfied for $\mu \ll m_\chi$, where μ is the mass of the exchanged boson, but it can also be satisfied for $\mu \sim m_\chi$ if the WIMPs annihilate through the exchange of a particle Y with mass $M_Y \gg m_\chi$. However, we will see that the corrections become small if $\mu \gtrsim m_\chi$. Note also that these corrections do *not* capture UV effects like the renormalization of the tree–level couplings of χ.

Let $P = (p_1 + p_2)/2 = (p_1' + p_2')/2$, $p = (p_1 - p_2)/2$ and $p' = (p_1' - p_2')/2$; recall that p_1, p_2 and p_1', p_2' are the four–momenta in the initial and final state, respectively. In the cms we have $P_0 = \sqrt{\vec{p}^2 + m_\chi^2}, \vec{P} = 0$ and $p_0 = 0$. The initial state kinematics is thus fixed by $\vec{p}$. We write the one–loop corrected amplitude for annihilation from the partial wave denoted by L as

$$A_L(|\vec{p}|, p') = A_{0,L}(|\vec{p}|, p') + \delta A_L(|\vec{p}|, p')\,, \tag{226}$$

where $A_{0,L}$ and δA_L denote the tree–level amplitude and the one–loop correction term, respectively. We are only interested in the cases $L = S$ and $L = P$. The contribution of higher partial waves is strongly suppressed during WIMP freeze–out.

The corrections can be calculated starting from the observation that annihilation from an $S-$ ($P-$)wave initial state can be described by a pseudoscalar (scalar) χ current [36]. This allows to write the correction as a standard vertex (three–point function) correction.

Let us begin with the simple case of scalar boson exchange:

$$\begin{aligned}\delta A_L(|\vec{p}|,p') &= ig^2\bar{v}(p_2)\int\frac{d^4q}{(2\pi)^4}\frac{\not{q}-\not{P}+m_\chi}{(q-P)^2-m_\chi^2+i\epsilon}(\gamma_5)^{n_L}\frac{\not{q}+\not{P}+m_\chi}{(q+P)^2-m_\chi^2+i\epsilon}\\ &\quad\times\frac{1}{(p-q)^2-\mu^2+i\epsilon}\tilde{A}_{0,L}(|\vec{q}|,p')\,u(p_1)\,. \qquad (227)\end{aligned}$$

Here g is the strength of the coupling between the boson and the WIMP, $n_L = 1$ (0) for annihilation from an $S-$ $(P-)$wave initial state, and the reduced tree-level amplitude $\tilde{A}_{0,L}$ describes the blob in Fig.23 (except for the factor γ_5 in case of $S-$wave annihilation, which appears explicitly in Eq. (227)) as well as the final state.[14] We will later show how to treat the exchange of spin–1 bosons.

As a first simplification, one then uses the fact that the full relativistic boson propagator satisfies $1/(k^2-\mu^2) = -1/(\vec{k}^2+\mu^2)\left[1-k_0^2/(k^2-\mu^2)\right]$; the second term can be omitted in the non–relativistic limit, where the energy exchange is much smaller than the three–momentum exchange. Moreover, to leading order in the non–relativistic expansion, the $\vec{q}-$dependence of the reduced amplitude can be neglected, i.e. the factor $\tilde{A}_{0,L}$ can be pulled out of the integral.[15] We then perform the integrals in Eq. (227) starting from the q_0 integration. We are looking for poles in the lower half–plane, with residues that diverge in the limit $\vec{q},\vec{p}\to 0$ [63]. This gives

$$\delta A_L(|\vec{p}|,p') \simeq g^2\bar{v}(p_2)\int\frac{d^3q}{(2\pi)^3}\frac{(\not{q}-\not{P}+m_\chi)\,(\gamma_5)^{n_L}\,(\not{q}+\not{P}+m_\chi)}{8\omega P_0\,(\omega-P_0)\left[(\vec{p}-\vec{q})^2+\mu^2\right]}\tilde{A}_{0,L}(\vec{p}')\,u(p_1)\,, \quad (228)$$

where $\omega = \sqrt{\vec{q}^2+m_\chi^2}$; in the numerator one should take $q_0 = \omega - P_0$. For small 3–momenta, we have

$$\omega - P_0 \simeq \frac{\vec{q}^2-\vec{p}^2}{2m_\chi}\,; \quad (229)$$

note that this vanishes for $\vec{p},\vec{q}\to 0$, as advertised.

To zeroth order in the non–relativistic expansion we can set $\vec{q}\to 0$ in the numerator of Eq. (228). We see that this gives a non–vanishing result only if $n_L = 1$, i.e. if a γ_5 matrix is present; recall that this corresponds to annihilation from an $S-$wave. To this order we can replace $\not{P} = P_0\gamma^0$ acting to the right (on the $u-$spinor) by m_χ. The numerator of

---

[14] Note that Eq. (227) is one–loop exact, if the $\vec{q}$ dependence of $\tilde{A}_{0,L}$ is kept. For a full non–perturbative treatment the complete reduced amplitude $\tilde{A}_L$ should appear again in the integral on the right–hand side [63]. Recall, however, that we are only interested in one–loop corrections, in which case we may use $\tilde{A}_{0,L}$ in the integrand.

[15] In the $P-$wave case, the nontrivial dependence on the initial state three–momentum stems from the spinors describing the initial state and the Dirac structures shown explicitly in Eq. (227), not from the reduced amplitude. $\tilde{A}_{0,L}$ in fact does not depend on $|\vec{q}|$ if $\chi\chi$ annihilation proceeds through an $s-$channel diagram. For $t-$ or $u-$channel annihilation we have to assume that the particle exchanged in the annihilation process is significantly more off–shell than $|\vec{q}|\sim|\vec{p}|$.

Eq. (228) then reduces to $4\gamma_5 m_\chi^2$. Note that the factor of γ_5 is required in order to be able to access the large component of $\bar{v}(p_2)$; this is most easily seen in the Dirac representation. Moreover, the factor ωP_0 in the denominator of Eq. (228) can be replaced by m_χ^2, up to corrections which are of second order in three–momenta.

To summarize, we have made three approximations:

- We ingored the energy dependence of the φ propagator.
- In the q_0 integral we only kept the pole with the leading residue (in the non–relativistic limit).
- We ignore all $\vec{q}$ dependence in the numerator (for annihilation from the $S-$wave).

Note that these approximations have to be taken simultaneously in order to get a UV–finite result. One may worry that this gives a rather poor approximation of the exact vertex correction even in cases where the latter are finite, as in a purely scalar theory. In Appendix B we show that this approximation can indeed differ substantially from the exact vertex correction if $\mu \ll m_\chi$. Note that the exact vertex correction by itself becomes IR–divergent for $\mu = 0$. This leads to terms $\propto \log(m_\chi/\mu)$ which appear in the exact vertex correction, but not in our approximation. However, these terms are canceled by real emission diagrams and wave function corrections, which have to be included in order to obtain an IR–finite result for $\mu = 0$. In Appendix B we show that, at least for a simple scalar model, our approximation *does* accurately reproduce the *exact* radiative correction associated with the initial state, whenever these corrections are large.

Let us therefore proceed with our calculation, which does not require additional approximations. The angular integrations are straightforward. One is then left with a single integral to describe the correction to $S-$wave annihilation:

$$\delta A_S(|\vec{p}|, p') = \frac{g^2}{(2\pi)^3} \frac{\pi m_\chi}{|\vec{p}|} A_{0,S} \int_0^\infty d|\vec{q}| \frac{|\vec{q}|}{\vec{q}^2 - \vec{p}^2} \ln \frac{(|\vec{p}| + |\vec{q}|)^2 + \mu^2}{(|\vec{p}| - |\vec{q}|)^2 + \mu^2} \,. \tag{230}$$

Note that we have absorbed the spinors into the full tree–level amplitude $A_{0,S}$. The one–loop correction to the cross section emerges from the interference between the correction δA_S and the tree–level term $A_{0,S}$. We can thus write

$$\delta A_S(|\vec{p}|, p')\big|_{1-\text{loop}} = \frac{g^2}{4\pi^2} \frac{1}{v} A_0(|\vec{p}|, p') I_S(r) \,, \tag{231}$$

where v is the relative velocity between the two annihilating WIMPs in their center of mass frame (i.e., $|\vec{p}| = m_\chi v/2$), and we have defined the function

$$I_S(r) = \Re\text{e} \left[\int_0^\infty dx \frac{x}{x^2 - 1} \ln \frac{(1+x)^2 + r}{(1-x)^2 + r} \right] \,. \tag{232}$$

Here $x = |\vec{q}|/|\vec{p}|$ and $r = \mu^2/\vec{p}^2$.

So far we have assumed that a spin–0 boson with scalar coupling is exchanged between the annihilating WIMPs. In order to treat more general cases, we rewrite the numerator of Eq. (228) as

$$\mathcal{N} = \Gamma \left(\not{q} - \not{P} + m_\chi \right) (\gamma_5)^{n_L} \left(\not{q} + \not{P} + m_\chi \right) \bar{\Gamma} \, , \tag{233}$$

where Γ describes the Dirac structure of the $\varphi\chi\chi$ coupling and $\bar{\Gamma} = \gamma^0 \Gamma^\dagger \gamma^0$ its Dirac conjugate. Scalar exchange corresponds to $\Gamma = \bar{\Gamma} = 1$.

It is easy to see that pseudoscalar exchange, $\Gamma = -\bar{\Gamma} = \gamma_5$, does not lead to enhanced contributions. For example, for $n_L = 1$ and $q \to 0$ one finds a result $\propto \gamma_5 \left(m_\chi - \not{P} \right)^2$, which is $\mathcal{O}(\vec{p}^2)$.

Vector exchange corresponds to $\Gamma = \gamma^\nu, \ \bar{\Gamma} = \gamma_\nu$, where the Lorentz index ν has to be summed. For $n_L = 1$ and $q \to 0$ this gives

$$\mathcal{N}_{\text{vector}} = -2 m_\chi \gamma_5 \gamma^\nu \left(m_\chi + \not{P} \right) \gamma_\nu = -4 m_\chi \gamma_5 \left(2 m_\chi - \not{P} \right) \, .$$

Again replacing $\not{P}$ by m_χ this leads to the *same* result as for scalar exchange, except for an overall sign. However, this sign is compensated by the extra minus sign in the vector boson propagator. We thus reproduce the well–known result that in the non–relativistic limit, the exchange of a vector boson has the same effect as that of a scalar boson.

Finally, axial vector exchange is described by setting $\Gamma = \gamma^\nu \gamma_5, \ \bar{\Gamma} = \gamma_\nu \gamma_5$, where summation over ν is again implied. In the $S-$wave case, where $n_L = 1$ and $q \to 0$ in the numerator, this gives

$$\mathcal{N}_{\text{axial vector}} = \gamma_5 \gamma^\nu \left(\not{P} - m_\chi \right)^2 \gamma_\nu = 4 m_\chi \gamma_5 \left(2 m_\chi + \not{P} \right) \, .$$

Again replacing $\not{P}$ by m_χ, and accounting for the minus sign in the spin–1 propagator, we find that axial vector exchange differs from scalar or vector exchange by a factor of -3.

This does not seem to have been noticed in the recent literature. We therefore checked it in the limit where φ exchange can be treated as re–scattering of the incoming WIMPs, leading again to two on–shell WIMPs. To leading order in velocity expansion we are interested in the limit of vanishing momentum exchange. However, we have to keep in mind that the two WIMPs will have to annihilate through a γ_5 vertex (for the $S-$wave case). This requires that the non–relativistic u and v spinors have the same spin. The rescattering process is then described by the quantity (we omit the bosonic propagator and all couplings)

$$A_{\text{res}} = \sum_{s'} \bar{v}(p_2, s) \bar{\Gamma} v(p_2, s') \bar{u}(p_1, s') \Gamma u(p_1, s) \, , \tag{234}$$

where s, s' describe the spin. Scalar boson exchange again corresponds to $\Gamma = \bar{\Gamma} = 1$. In this case only $s' = s$ contributes in the non–relativistic limit, where (in the cms) $p_1 =$

$p_2 \simeq (m_\chi, \vec{0})$, and one has $A_{\text{res, scalar}} = -4m_\chi^2$. One immediately sees that pseudoscalar exchange only contributes at $\mathcal{O}(\vec{p}^2)$.

In case of vector exchange, only $\Gamma = \gamma^0$ contributes to $\mathcal{O}(\vec{p}^0)$ [63]. This then again requires $s = s'$ in Eq. (234), giving $A_{\text{res, vector}} = 4m_\chi^2$. Remembering the additional minus sign in the spin–1 propagator we therefore again find that vector boson exchange contributes the same way as scalar exchange.

Finally, for axial vector exchange, only $\Gamma = \gamma_i \gamma_5$ $(i = 1, 2, 3)$ contribute to $\mathcal{O}(\vec{p}^0)$. In this case A_{res} receives non–vanishing contributions both from $s = s'$ and from $s = -s'$, so that $A_{\text{res, axial vector}} = -12m_\chi^2$. Again including the minus sign from the propagator, we reproduce our earlier result that axial vector exchange differs from scalar or vector exchange by a factor of -3. Note also that axial vector exchange describes an interaction between the spins of the two WIMPs. Such interactions are not suppressed at low velocities.

Now let us discuss $P-$wave annihilation, which corresponds to $n_L = 0$ in Eq. (228). In this case setting $\vec{q} = 0$ would lead to a result which is of $\mathcal{O}(\vec{p}^2)$, i.e. of *second* order in the non–relativistic expansion. The leading term is the one linear in $\vec{q}$; the numerator of Eq. (228) then becomes $-4m_\chi \vec{q} \cdot \vec{\gamma}$. Note that the γ_i again allow to access the large component of $\bar{v}(p_2)$. The proper form of the correction term can then most easily be obtained using trace techniques, by dividing the 1–loop correction term $\delta A_P A_{0,P}^\dagger$ by the tree–level result $|A_{0,P}|^2$. We find that the $P-$wave correction term differs from the $S-$wave term by a factor $\vec{p} \cdot \vec{q}/\vec{p}^2$ inside the momentum integral. Performing the angular integrals, we can write this in the form of Eq. (231), with a new function describing the correction for annihilation from a $P-$wave initial state:

$$I_P = \Re\text{e} \left\{ \int_0^\infty dx \frac{2x^2}{x^2 - 1} \left[-1 + \frac{x^2 + 1 + r}{4x} \ln \frac{(x+1)^2 + r}{(x-1)^2 + r} \right] \right\} , \tag{235}$$

where $r = \mu^2/\vec{p}^2$ as above.

In order to treat the exchange of other bosons, non–trivial Dirac structures Γ, $\bar{\Gamma}$ again have to be introduced in Eq. (228), now for the case $n_L = 0$. Proceeding as above, we find that pseudoscalar exchange does not lead to a large correction, while vector and axial vector exchange give the *same* correction as the exchange of a scalar boson. At first glance it may seem surprising that now axial vector exchange gives the same, positive, contribution; recall that in case of annihilation from an $S-$wave, axial vector exchange differed by a factor of -3. The difference can be understood from the observation that axial vector exchange leads to a spin–spin interaction of the form $4\vec{s}_1 \cdot \vec{s}_2$, where $\vec{s}_{1,2}$ are the spins of the two WIMPs. This can be evaluated using $2\vec{s}_1 \cdot \vec{s}_2 = S^2 - s_1^2 - s_2^2$, where $\vec{S} = \vec{s}_1 + \vec{s}_2$ is the total spin. In case of Majorana WIMPs, annihilation from an $S-$wave requires [36] $S = 0$, leading to $4\vec{s}_1 \cdot \vec{s}_2 = -3$. For $P-$wave annihilation, we need [36] $S = 1$, giving $4\vec{s}_1 \cdot \vec{s}_2 = 1$. Note the relative factor of -3 between these two results.

At this point a comment on other WIMPs (than Majorana fermions) is in order. For a Dirac fermion–antifermion pair, there is no strict correspondence between the total spin and the orbital angular momentum. There will also be $S-$wave states with $S = 1$ (as the J/ψ family of quarkonia), as well as $P-$wave states with $S = 0$. In this case the proper factor in front of the axial vector correction will depend on the spin state, i.e. it will no longer be completely process independent in this case. However, results for scalar, pseudoscalar and vector exchange are the same as for Majorana WIMPs.[16] Finally, there is no such thing as an axial vector coupling to scalars, but our results for vector exchange apply to scalar WIMPs as well.[17] Scalar exchange now involves a trilinear scalar interaction f, which has dimension of mass. Our results can describe this situation as well, with $g = f/(2m_\chi)$.

The integrals in Eqs. (232) and (235) should be understood as principal value integrals, in order to treat the pole at $x = 1$. In case $r \gg 1$ the integrals can be computed analytically, by expanding the logarithms in inverse powers of r. Moreover, in the limit $r \to 0$ both I_S and I_P approach $\pi^2/2$, thereby reproducing the well–known result [65] that the one–loop "Sommerfeld factor" for massless boson exchange is the same for $S-$ and $P-$partial waves. We also found accurate numerical expressions for small and moderate r. Altogether, the correction factors can be described by

$$I_S(r) \simeq \begin{cases} \frac{2\pi}{\sqrt{r+1}}\left(1 - \frac{1}{r+2}\right) & \text{(large } r\text{)} \\ \frac{\pi^2/2}{1+\frac{\sqrt{r}}{\pi}+\frac{r}{\pi^2}} & \text{(small } r\text{)} \end{cases}$$
$$I_P(r) \simeq \begin{cases} \frac{2\pi}{3\sqrt{r+1}}\left(1 + \frac{1.3}{r+1}\right) & \text{(large } r\text{)} \\ \frac{\pi^2/2}{1+\frac{3\sqrt{r}}{\pi}+\frac{r}{\pi}} & \text{(small } r\text{)} \end{cases} \qquad (236)$$

The approximations for large and small r intersect at $r \simeq 5.6$ (4.2) for I_S (I_P); the two approximations for I_P intersect a second time at $r \simeq 6.3$.

In Fig. 24, the exact function I_S and its approximations are shown. By switching from the low$-r$ to the high$-r$ expression at the intersection point one reproduces the exact numerical result to better than 4% for all values of r. In case of I_P (not shown) the large$-r$ approximation overshoots rather than undershoots the exact result for $10^{-3} \lesssim r \lesssim 1$. This leads to slightly larger discrepancies, of up to 6%, between the exact I_P and its approximations at $r \sim 5$ where the two approximations intersect. For the purpose of calculating the WIMP relic density a relative error on the *correction* of 6% is quite acceptable.

---

[16] Strictly speaking, Majorana fermions do not have diagonal vector couplings. They can, however, have vector couplings to other Majorana states. Our result is applicable to this situation in the limit where the mass of the second Majorana fermion approaches that of the annihilating WIMP.

[17] A vector coupling exists only for a complex scalar, which can carry a charge.

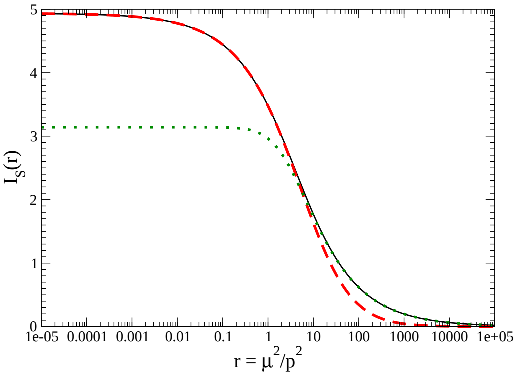

Figure 24: Comparison between the exact I_S (solid, black) and its approximations for large r (dotted, green) and small r (dashed, red).

In Fig. 25 we show $I_S(r)$ and $I_P(r)$ as black and red (grey) lines, respectively. As noted earlier, the two functions coincide for massless exchange bosons, $r = 0$. For nonvanishing boson mass, $r > 0$, the $S-$wave contribution is larger than the $P-$wave one, by up to a factor of 3 at large r; see Eqs. (236). Note that for any finite mass of the exchanged boson, $\mu \neq 0$, the zero–velocity limit $|\vec{p}| \to 0$ corresponds to $r \to \infty$. Eqs. (236) show that asymptotically $I_{S,P}(r \to \infty) \propto 1/\sqrt{r} = |\vec{p}|/\mu$. Eq. (231) then shows that the corrections approach constant values of order $g^2 m_\chi/(4\pi\mu)$ for $|\vec{p}| \to 0$, if $\mu \neq 0$. Such corrections will threaten the convergence of perturbation theory only if the WIMP and boson masses differ by a loop factor; in the technically more natural case where the boson mass lies a factor of a few below that of the WIMP, we still find a significant enhancement relative to the naive expectation that corrections should be of order $g^2/(16\pi^2)$. We finally note that our numerical results are consistent with those in [66].

2. Dark Matter relic density

Let us describe how to calculate the loop–corrected WIMP relic density from the loop–corrected WIMP annihilation cross section.

The one–loop corrected WIMP annihilation cross section for partial wave labeled by L can be written as

$$\sigma_L = \sigma_{0,L} + \delta\sigma_L \,. \tag{237}$$

Eq. (231) and the analogous expression for annihilation from the $P-$wave imply that

$$\begin{aligned} \delta\sigma_S &= \frac{g^2}{2\pi^2 v} I_S(r)\sigma_{0,S}\,; \\ \delta\sigma_P &= \frac{g^2}{2\pi^2 v} I_P(r)\sigma_{0,P}\,. \end{aligned} \tag{238}$$

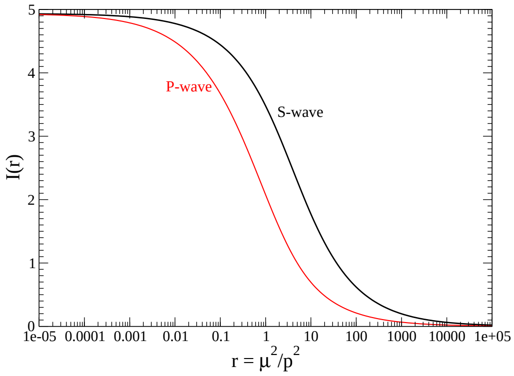

Figure 25: Comparison between I_S describing the correction for annihilation from an $S-$wave (black) and I_P describing the correction for annihilation from a $P-$wave (red).

Recall that the thermally averaged cross section times relative velocity can be written as follows:

$$\langle \sigma v \rangle = \frac{2x^{3/2}}{\sqrt{\pi}} \int_0^\infty (\sigma v) \frac{v^2}{4} e^{-xv^2/4} dv \,, \tag{239}$$

In order to calculate the thermal averages over the correction terms, we rewrite the integral in Eq. (239) in terms of the integration variable $t = v\sqrt{x}$:

$$\langle \delta\sigma_L v \rangle = \frac{1}{2\sqrt{\pi}} \int_0^\infty dt \, t^2 (\delta\sigma_L v) \mathrm{e}^{-t^2/4} \,. \tag{240}$$

Eqs. (238) imply that the $t-$dependence of $\delta\sigma_L v$ takes the form $v^n I_L(r) = (t/\sqrt{x})^n I_L \left(\frac{4\mu^2 x}{m_\chi^2 t^2} \right)$, with $n = -1$ $(+1)$ for annihilation from an $S-$ $(P-)$wave initial state. This implies that the thermal average over the correction terms to the WIMP annihilation cross section can be written as $x^{-n/2}$ times a function of $z = 2\mu\sqrt{x}/m_\chi$.

While the expansion of $\sigma_0 v$ in powers v in Eq. (218) works rather well for the tree–level cross section σ_0, the loop corrections we computed in the previous Section cannot be parameterized in this way. We saw in Fig. 25 that the correction factors I_S and I_P depend strongly on v via the quantity $\sqrt{r} = \mu/|\vec{p}| = 2\mu/(m_\chi v)$. We thus have to re–compute $\langle \sigma v \rangle$, which can then be used in Eq. (217) to derive the Dark Matter relic density using Eq. (216).

In Appendix A we describe how we parameterize the resulting functions for $S-$ and $P-$wave annihilation. The one–loop corrections to the "annihilation integrals" can then be written as

$$\begin{aligned} \delta J_S(x_f) &= \frac{g^2 \mathscr{A}}{\pi^{5/2}} \frac{\mu}{m_\chi} \int_{z_F}^\infty \frac{dz}{z^2} \left(\frac{1}{a_S z^2 + b_S z + c_S} + d_S \right) \,, \\ \delta J_P(x_f) &= \frac{64 g^2 \mathscr{B}}{\pi^{5/2}} \left(\frac{\mu}{m_\chi} \right)^3 \int_{z_F}^\infty \frac{dz}{z^4} \left[\exp(-a_P z + b_P) + \frac{1}{c_P z + d_P} \right] \,. \end{aligned} \tag{241}$$

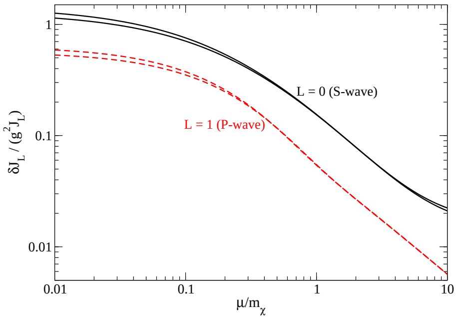

Figure 26: Corrections to the annihilation integrals for annihilation from the $S-$ wave (solid, black) and $P-$wave (dashed, red or grey), normalized to the tree–level results, and divided by the square of the WIMP coupling to the exchanged boson g. The upper (lower) curves are for inverse scaled freeze–out temperature $x_F = m_\chi/T_F = 25$ (20).

Here $z_F = (2\mu/m_\chi)\sqrt{x_F}$, and the coefficients a_S, b_S, c_S, d_S and a_P, b_P, c_P, d_P are given in Eqs. (A.4) and (A.8), respectively. We have made the simplifying assumption that $\mathscr{B}$ is dominated by $P-$wave contributions. This is true whenever the contribution $\propto \mathscr{B}$ to the annihilation integral is comparable to, or dominates over, the one $\propto \mathscr{A}$. In the opposite case the *correction* to the $\mathscr{B}-$term will in any case be insignificant.[18]

Not surprisingly, the corrections are quadratic in the coupling of the exchanged boson to the WIMP. Moreover, they depend on the boson mass *only* through the ratio μ/m_χ. Recall finally that I_S has to be multiplied with -3 if the exchanged boson has axial vector couplings; the same factor has to be included in $\delta J_S(x_F)$.

In Fig. 26 we show the *relative* size of the loop corrections to the annihilation integrals for $S-$ and $P-$wave annihilation, divided by the square of the WIMP–boson coupling g. Eq. (216) shows that this also gives the relative change of the relic density due to our loop corrections, as long as the corrections are small, in which case x_F remains essentially unchanged by these corrections; note that x_F depends only logarithmically on the annihilation cross section. This is the main model–independent result in this subsection. The size of the corrections to the relic density can be read off directly, by simply inserting the values of masses μ and m_χ and coupling g given in a concrete model.

We see that the corrections are less important for $P-$wave annihilation. This is true even for $\mu \ll m_\chi$, where the loop functions I_S and I_P become equal. In this limit $v\delta\sigma_S \propto 1/v$ while $v\delta\sigma_P \propto v$. Performing the integrals for the thermal averaging, Eq. (239), and inserting the results into the definition of the annihilation integral, Eq. (217), one

---

[18] The one–loop correction to the $\mathcal{O}(v^2)$ contribution to the $S-$wave annihilation cross section involves the sum of two terms: the product of the $\mathcal{O}(v^0)$ one–loop correction and the $\mathcal{O}(v^2)$ tree–level amplitude, and the product of the $\mathcal{O}(v^2)$ one–loop correction and the $\mathcal{O}(v^0)$ tree–level amplitude. Only the first of these terms can be computed using the results in this subsection.

finds

$$\frac{\delta J_P/J_P}{\delta J_S/J_S} = \frac{4}{9} \quad \text{for } \mu \to 0\,. \tag{242}$$

The ratio becomes even smaller for nonvanishing μ, because then $J_P < J_S$.

Fig. 26 shows the results for $x_F = 25$ (upper curves) and $x_F = 20$ (lower curves); this spans the range of decoupling temperatures in usual WIMP models. One can easily show analytically that in the limit $\mu \to 0$, $\delta J_L/J_L \propto \sqrt{x_F}$ for both $L = 0$ ($S-$wave) [69] and $L = 1$ ($P-$wave). On the other hand, Fig. 26 shows that the *relative* correction to the annihilation integral becomes independent of x_F once $\mu \gtrsim 0.3 m_\chi$. This figure also shows that for the most plausible scenarios with electroweak strength couplings, possibly suppressed by mixing effects, where $g^2 \lesssim 0.5$, the loop corrections are significant only for $\mu \lesssim m_\chi$, as stated in the beginning of this subsection.

Two comments are in order before concluding this Section. First, Fig. 26 seems to imply that, especially for $P-$wave annihilation, the corrections are never very large. This is misleading. A simple one–loop calculation can be trusted only if $\delta\sigma < \sigma$ for *all* relevant velocities v. This requires $g^2 I_{S,P}/(v\pi^2) < 1$. For $\mu \to 0$ this will always be violated at sufficiently small v, requiring summation of higher orders. In the standard treatment [70, 63, 66] this leads to $\delta\sigma \propto 1/v$ even for annihilation from a $P-$wave initial state. We saw at the end of Sec. 3.1.2. that for finite μ the maximal size of the correction to the cross section is of relative size $g^2 m_\chi/(4\pi\mu)$. Our one–loop calculation can be trusted as long as this quantity is well below 1.

Secondly, it has very recently been pointed out [71] that Eq. (217) becomes inadequate for very small μ. In this case the annihilation integral receives sizable contributions from quite large x, i.e. from low temperatures. Eq. (217) assumes that the WIMPs are in kinetic equilibrium while they are annihilating. It has to be modified for temperatures below the kinetic decoupling temperature, which is typically a few (tens of) MeV [72]. This modification can have sizable effects for very small μ [71]. However, we just saw that our strictly perturbative treatment is not reliable in this case anyway. Recall that $v\delta\sigma$ becomes constant, rather than scaling like $1/v$, for velocities below $v_{\text{crit}} = \mu/m_\chi$. Our perturbative treatment will be reliable only if $\mu/m_\chi \gg g^2/(4\pi) \sim 0.01$. This implies that WIMP annihilation will quickly become irrelevant for $x > 1/v_{\text{crit}}^2 \sim 10^4$, well before kinetic decoupling occurs.

3. Applications

In the following, we apply our results to existing WIMP models. We start with two simple models with scalar or fermionic SM singlets. Finally, we discuss the more widely studied case of the MSSM neutralino.

Scalar singlet WIMP

This is the simplest WIMP model [73]. One only needs to introduce a single real scalar field χ to describe Dark Matter. If one forbids terms linear in χ by some (possibly discrete) symmetry in order to prevent χ decays, the only renormalizable coupling to SM fields allowed by all symmetries is of the form $\chi^2|h|^2$, where h is the scalar Higgs doublet. Upon weak symmetry breaking this gives rise to a trilinear scalar interaction of the form $V\chi^2\phi$, where ϕ is the physical Higgs scalar of the SM and $V = 246$ GeV the vacuum expectation value (vev) of the Higgs.

These interactions allow χ to annihilate via ϕ exchange in the $s-$channel; annihilation into two ϕ bosons is also allowed for $m_\chi > m_\phi$. An accurate tree–level calculation of the resulting relic density has been performed in [74]. Writing the coefficient of the $\chi^2|h|^2$ term in the Lagrangian as $-k/2$, they find that the correct relic density (4) is obtained for $k \simeq 0.28 m_\chi/(1 \text{ TeV})$, unless $m_\chi \sim m_\phi/2$, in which case an even smaller k is required. We can use our formalism to compute corrections to this result from ϕ exchange prior to annihilation, i.e. $\varphi = \phi$ in this case. This gives a coupling factor[19] $k^2V^2/(4m_\chi^2) \simeq 0.0012$, (almost) independent of m_χ. Fig. 26 shows that the corrections due to ϕ exchange in the initial state will then at best be at the permille level. In this model we therefore do not find any significant radiative corrections involving the initial state only. This should also hold for the inert doublet model [75], since the coupling between the inert WIMP doublet and the SM Higgs boson will have to satisfy a similar relation.

Fermionic singlet WIMP

The next simplest WIMP model [76] contains a Dirac fermion SM singlet χ as well as a real scalar singlet φ, with couplings $g\bar{\chi}\chi\varphi + A\varphi|h|^2$, where h is again the Higgs doublet of the SM. The latter term induces mixing between the singlet φ and the SM Higgs boson, allowing φ to decay. If this mixing is small and $m_\varphi < m_\chi$, the dominant $\bar{\chi}\chi$ annihilation channel is into two φ bosons, via $t-$ and $u-$channel diagrams. In the non–relativistic limit this is a pure $P-$wave process, with tree–level cross section

$$v\sigma(\bar{\chi}\chi \to \varphi\varphi) = \frac{g^4 v^2 \beta}{24\pi} \frac{m_\chi^2 \left(9m_\chi^4 - 8m_\chi^2 m_\varphi^2 + 2m_\varphi^4\right)}{\left(2m_\chi^2 - m_\varphi^2\right)^4} + \mathcal{O}(v^4)\,, \tag{243}$$

where $\beta = \sqrt{1 - m_\varphi^2/m_\chi^2}$. In the limit $m_\chi^2 \gg m_\varphi^2$ this simplifies to

$$v\sigma(\bar{\chi}\chi \to \varphi\varphi) = \frac{3g^4v^2}{128\pi m_\chi^2}\,.$$

The tree–level calculation therefore predicts the correct relic density (4) for coupling

$$g^2 \simeq 0.2 \frac{m_\chi}{100 \text{ GeV}}\,.$$

---

[19] Recall from our discussion near the end of Sec. 3.1.2. that the relevant quantity for a purely scalar theory is the trilinear scalar coupling divided by $2m_\chi$, i.e. in the case at hand, $g = kV/(2m_\chi)$.

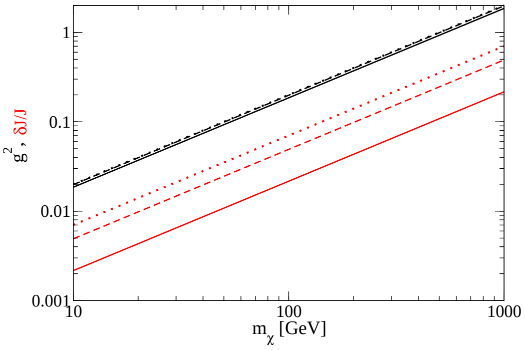

Figure 27: Strength of the $\bar{\chi}\chi\varphi$ coupling g (black), as well as the resulting one–loop correction to the annihilation integral (red), in a model with Dirac fermion singlet DM. g has been computed from the requirement that $\bar{\chi}\chi \to \varphi\varphi$ annihilation produces the correct χ relic density at tree level. The solid (dashed, dotted) curves are for $\mu/m_\chi = 0.5\ (0.2,\ 0.1)$, where $\mu \equiv m_\varphi$.

This can then be used to read off the correction due to φ exchange in the initial state from Fig. 26, with $\mu = m_\varphi$. The result is shown in Fig. 27, where we have used the exact (tree–level) result Eq. (243) to derive the required coupling strength. The black curves show that this coupling strength depends only very weakly on the mass of the scalar for $\mu \equiv m_\varphi \lesssim 0.5 m_\chi$. Note that the cross section slightly *increases* with increasing m_φ as long as $m_\varphi < 0.85 m_\chi$. The reason is that increasing m_φ allows the $t-$ and $u-$channel propagators to be less off–shell, as shown by the denominator in Eq. (243). As a result, the required coupling strength slightly decreases with increasing m_φ.

However, the red curves show that this effect is much smaller than the strong dependence of $\delta J_P/J_P$ on μ/m_χ illustrated in Fig. 26. More importantly, we see that the corrections due to φ exchange in the initial state can easily exceed the uncertainty of the observational determination of the DM relic density; for $\mu/m_\chi = 0.5\ (0.2,\ 0.1)$ they even reach the 10% level for $m_\chi > 450\ (210,\ 130)$ GeV. Since the correction is positive, one would have to reduce the coupling in order to obtain the correct relic density after inclusion of one–loop corrections. This would correspondingly reduce all interactions between the WIMP χ and the SM particles, all of which are mediated by φ exchange.

The lightest neutralino in the MSSM

We finally want to apply our formalism to the lightest neutralino in the minimal supersymmetric extension of the Standard Model (MSSM), which is the probably best motivated WIMP, and certainly the most widely studied [16, 77] one. For simplicity we will assume that sfermions are heavy. Given experimental lower bounds on the masses of sfermions and Higgs bosons, relatively light sfermions by themselves typically only lead to an acceptable neutralino relic density in the presence of significant co–annihilation [78]. This involves several particles, with mass splittings of order of the absolute value of the 3–momentum in the initial state. These more complicated scenarios cannot be treated with the formalism presented in this thesis.[20]

Recall that in the MSSM the neutralinos are mixtures of the $U(1)_Y$ gaugino $\tilde{B}$, the neutral $SU(2)$ gaugino $\widetilde{W}_3$, and of the two neutral higgsinos $\tilde{h}_1^0,\ \tilde{h}_2^0$:

$$\tilde{\chi}_i^0 = N_{i1}\tilde{B} + N_{i2}\widetilde{W}_3 + N_{i3}\tilde{h}_1^0 + N_{i4}\tilde{h}_2^0 \ \ (i = 1, \cdots, 4). \tag{244}$$

The coefficients N_{ik} satisfy the sum rule $\sum_{k=1}^{4} |N_{ik}|^2 = 1\ \forall i$. Most phenomenological analyses of the MSSM assume that the soft SUSY breaking gaugino masses unify at or near the scale of Grand Unification [77]. This implies that the $U(1)_Y$ gaugino mass is about half the $SU(2)$ gaugino mass near the TeV scale. As a result, the wino component of our candidate WIMP, the lightest neutralino ($\chi \equiv \tilde{\chi}_1^0$), is subdominant, i.e. $|N_{11}|^2 \gg |N_{12}|^2$. If sfermions are heavy, χ annihilation involves couplings of the lightest neutralino to gauge or Higgs bosons, which vanish in the pure Bino limit ($|N_{11}| \to 1$). In models with gaugino mass unification and heavy sfermions, the annihilation cross section can thus only be sufficiently large if χ has significant higgsino components.

On the other hand, for a nearly pure higgsino, where $|N_{11}|^2 + |N_{12}|^2 \ll 1$, the cross section for annihilation into W^+W^- and Z^0Z^0 pairs is so large that a mass $m_\chi \simeq 1$TeV is required to obtain the correct relic density Eq. (4) [80]. Such a large mass for the lightest superparticle is at odds with the primary motivation for postulating the existence of superparticles, which is the stabilization of the weak scale against quadratically divergent quantum corrections.

Assuming gaugino mass unification, the most natural neutralino satisfying the constraint Eq. (4) is therefore a bino–higgsino mixture, dubbed a “well–tempered neutralino” in [81]. Note that the neutralino couplings to Higgs bosons involves products of a combination of gaugino components ($N_{i2} - \tan\theta_W N_{i1}$, where θ_W is the weak mixing angle) with one of the higgsino components ($N_{i3},\ N_{i4}$). These couplings are maximal in the region of strong gaugino–higgsino mixing, and should thus be sizable for the “well–tempered” neutralino. Moreover, as well known, at least one of the neutral MSSM Higgs bosons is rather light, with mass below 130 GeV. This leads one to expect potentially sizable 1–loop corrections due to the exchange of a Higgs boson prior to WIMP annihilation.

We checked this with the help of the the code `micrOMEGAs 2.2` [31]. Among other things, this program computes the complete tree–level neutralino annihilation cross sec-

---

[20] Very recently the summation of “Sommerfeld corrections” for the case of nearly degenerate states was discussed in [79].

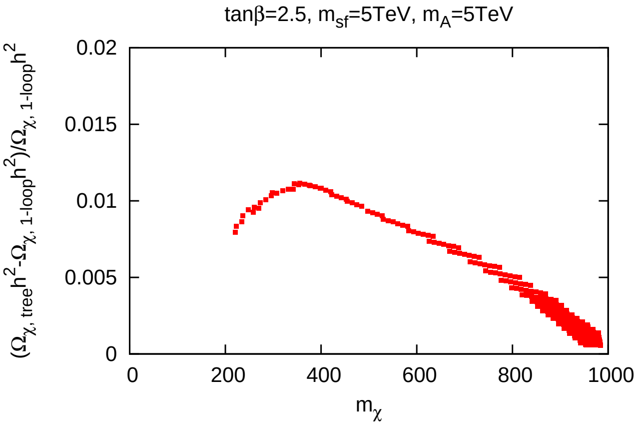

Figure 28: The relative size of one-loop correction to the relic density of a "well-tempered" neutralino. The ratio between M_1 and μ is fixed such that the relic density satisfies the constraint (4) within two standard deviations. We take $M_2 = 2M_1$, consistent with gaugino mass unification, $\tan\beta = 2.5$, and assume sfermions and most Higgs bosons to be very heavy. Scenarios with $m_\chi < 200$ GeV are excluded by Higgs boson searches.

tions for all two–body final states. It does not resort to the non–relativistic expansion Eq. (218), but one can easily determine the coefficients $\mathscr{A}$ and $\mathscr{B}$ by calculating the annihilation cross section at two different values of v, i.e. for two (slightly) different cms energies $\sqrt{s}$. These coefficients are then used in Eqs. (241) to compute the *corrections* to the annihilation integral; we emphasize that we continue to use the full cross sections, not their non–relativistic expansions, for the calculation of the tree–level contribution to the annihilation integral. We also take x_F from the program. The one–loop corrected χ relic density can then be expressed as

$$\Omega_\chi h^2 = \Omega_{\chi,0} h^2 \frac{J_0(x_F)}{J_0(x_F) + \delta J(x_F)} \tag{245}$$

where $\delta J = \delta J_S + \delta J_P$, and the tree–level value $J_0(x_F)$ can be calculated from the program's tree–level prediction $\Omega_{\chi,0} h^2$ using Eq. (216).

The result is shown in Fig. 28. It has been generated using `micrOMEGAs` [31], using `SOFTSUSY` [30] to calculate the superparticle and Higgs boson spectrum; we specify the input directly at the weak scale. All points satisfy the relic density constraint (4) within two standard deviations. For simplicity we take (unnaturally) large values for the masses of all sfermions and of the CP–odd Higgs boson A, but the results would not change significantly as long as $m_{\rm sf} \gtrsim 2m_\chi$ and $m_A \gtrsim 3m_\chi$. We include loop corrections due to exchange of the $Z-$boson as well as both CP–even neutral Higgs boson, but the contribution from the heavier Higgs boson is totally negligible due to its large mass.

We see that the corrections are most important for m_χ near 350 GeV. For smaller

WIMP mass the corrections are reduced because the higgsino component of χ becomes smaller, and because the ratio of light Higgs and WIMP masses becomes smaller, which reduces the loop functions. The latter effect would tend to increase the correction for heavier WIMPs. However, for $m_\chi > 350$ GeV the gaugino components of χ decrease quickly; this reduces its coupling to the light Higgs boson, which is most important here. Moreover, for $m_\chi \gtrsim 900$ GeV, co–annihilation with $\tilde{\chi}_1^\pm$ and $\tilde{\chi}_2^0$ become important [36, 82, 80]. The effect of light boson exchange corrections to co–annihilation is beyond the scope of this thesis, and has not been included in Fig. 28. As a result, the correction becomes comparable to the anticipated post–PLANCK precision of the observational determination of $\Omega_\chi h^2$ only for a rather narrow range of $m_\chi \sim 350$ GeV. This is consistent with the results of Fig. 26, given the fact that the coupling of our "well–tempered" neutralino to the lightest Higgs boson does not exceed 0.2.

The small size of the corrections due to boson exchange in the initial state indicate that these may well *not* be the leading radiative corrections in the MSSM. In fact, full electroweak one–loop calculations [69, 83] found much larger corrections in some cases. These are presumably due to UV–sensitive effects, which cannot be treated using our formalism. Moreover, QCD corrections can significantly affect the annihilation cross section into quarks [69, 85].

3.2 Direct and Indirect Dark Matter Detection

3.2.1 Theoretical Basis

The discussions in this subsection are based on [5, 77], and the references therein.

1. Direct WIMP search

As the Earth moves inside our Galaxy, the WIMPs pass through the Earth. The direct detection of WIMPs is based on the nuclear recoil from the elasitic scattering of WIMP and the nucleus.

The interaction rate can be qualitatively written as,

$$R \approx n\sigma\langle v\rangle/m_N, \tag{246}$$

where $n(=\rho_0/m_\chi)$ is the local WIMP number density (ρ_0, m_χ are the local energy density and the mass of WIMP, respectively.), σ is the WIMP-nucleus interaction cross section, $\langle v\rangle$ is the averaged speed of WIMP to the target, and m_N is the mass of nucleus. Since the local energy density (~ 0.3GeV) and the velocity (~ 220km/s) can be estimated from the astrophysical observations, the experimental constraints on the cross section are given for the corresponding mass of the WIMP. For the WIMP with cross section and the mass typical in MSSM, the interaction rate is roughly 1 event per day and per kg of detector mass, much lower than the radioactive background.

The σ depends on the WIMP-quark interaction strength. Once the cross section is computed, it must be convoluted to the WIMP-nucleon interactions. To the non–relativistic limit (valid for the cold Dark Matter), the spin–independent and spin–dependent interactions are distinguished, and the target nuclei should be chosen accordingly.

For the low mass WIMP, the detection sensitivity is constrained by the dectector energy threshold, for the mean value in the nuclear recoil spectrum is higher for the higer WIMP mass. On the other hand, the local WIMP flux, hence the interaction rate, is inversely proportional to the WIMP mass.

The signals from WIMPs have two distinct features:

- *Annual modulation* The velocity of WIMP in the earth frame is obtained by subtracting the earth velocity from the WIMP velocity in the galactic frame. Therefore, the interaction rate varies as Earth moves around Sun. The effect causes only a few percent difference in the interaction rates.

- *Diurnal variation* As Earth spins, the average direction of WIMP wind with respect to a Dark Matter detector changes. Detectors by which the nuclear recoil direction can be measured to the angular resolution of 20-30 degrees are required.

2. Indirect WIMP search

The most reliable way to detect the WIMPs indirectly is to observe energetic neutrinos from the annihilation of WIMPs accumulated in the Sun or Earth by gravitational interaction. Eventually capture and annihilation of WIMPs in the Sun reach equilibrium. The only annihilation products that can escape the Sun are neutrinos. In particular, muon neutrinos produce muons via charged current interactions; these muons can be searched for by “neutrino telescopes”.

The WIMPs in the Galactic halo annihilates into ordinary matters, which hadronize and produce antiprotons. The low energy ($\lesssim$ 1GeV) antiprotons can be produced, in contrast to the cosmic ray antiprotons with a high energy, produced by spallation of primary cosmic rays.

If the WIMPs can annihilate directly into electron–positron pairs, or into the W boson pairs, the observed positron energy spectrum will have a distinct peak, while it is expected to decrease with increasing energies in the standard cosmic rays propagation model.

WIMP annihilation in the halo may give a continuous and monochromatic gamma rays. Although the WIMPs have no tree–level coupling to the photon, they can annihilate to photons via loop diagrams. The photons produced will be monochromatic at an energy equal to the WIMP mass. On the ther hand, the intensity of gamma ray depends on the angle between the Galactic center and the line of sight; from the gamma ray excess with respect to the background in the various directions in the sky, we can obtain the halo profile [84].

There are many direct and indirect WIMP search experiments on-going or prospected. A overview on the current experimenatal status can be found in [5].

3.2.2 An Example: Neutralino Dark Matter in an SO(10) Model

All results presented in this subsection are obtained using a modified version [18] of `SOFTSUSY 2.0` [30] to evaluate the mass spectra at the weak scale. These are then fed into `micrOMEGAs 2.2` [31] to calculate the LSP relic density. If this is found acceptable, we feed the same low–energy spectrum into `DarkSUSY 5.0.2` [87] for the calculation of various Dark Matter detection rates [77].

Specifically, we compute: elastic LSP–proton scattering cross sections due to spin–independent as well as spin–dependent interactions; the muon flux resulting from LSP annihilation in the Sun; and the antiproton flux from LSP annihilation in the halo of our galaxy. In all cases we compare with the sensitivities of the best current and/or near–future experiments listed in the previous subsection. In most cases, we only consider parameter sets leading to a relic density within two standard deviations of the value found by combining WMAP data with other cosmological observations. Recall Eq. (4):

$$\Omega_{CDM}h^2 = 0.1131 \pm 0.0068. \tag{247}$$

We begin our discussion by analyzing the impact of reducing M_X, i.e. "switching on" the intermediate scales, on the elastic LSP–proton scattering cross section. Figure 29 shows the spin–independent (SI; left frame) and spin–dependent (SD; right frame) contributions to this cross sections as we vary M_X while most soft breaking parameters as well as the light neutrino masses are kept fixed. The scalar mass m_0 is varied along with M_X such that the relic density lies in the range of Eq. (247). Note that $m_0^2 \gg M_{1/2}^2$ in this plot, i.e. we are in the region of significant higgsino–neutralino mixing, which is most favorable for direct neutralino Dark Matter searches. As a result, the spin–independent cross section is always well above the projected sensitivity of the XENON100 experiment [88], while the spin–dependent cross section lies above the projected sensitivity of the DMTPC experiment [88].

While these gross features remain unchanged, we see that, as M_X decreases, i.e. as the deviation from mSUGRA becomes larger, the cross section is enhanced, so that for the lowest M_X, the spin–independent cross section slightly exceeds the limit set by the CDMS II experiment [17]. This is mostly due to the reduction of the LSP mass for fixed $M_{1/2}$

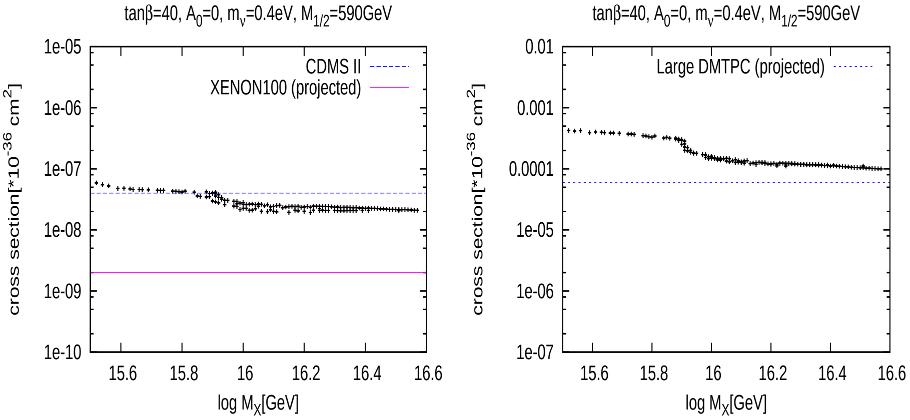

Figure 29: The M_X dependence of the SI (a) and SD (b) neutralino–proton scattering cross section. m_0 is varied such that the relic density satisfies the 247. The neutralino mass $m_\chi = 124$ GeV, for $M_X = 10^{15.5}$ GeV, increases to 235 GeV for $M_X = 10^{16.6}$ GeV. The experimental constraints are taken for the $m_\chi = 120$ GeV.

in the model with intermediate scales. In particular, for $M_X \leq 8 \cdot 10^{15}$ GeV, $m_{\tilde{\chi}_1^0} < m_t$, so that $\tilde{\chi}_1^0 \tilde{\chi}_1^0 \to t\bar{t}$ annihilation is forbidden. The loss of this important annihilation channel has to be compensated by increasing bino–higgsino mixing, i.e. by decreasing μ, which in turn is accomplished by increasing m_0. This leads to increased couplings of the lightest neutralino to neutral Higgs bosons as well as to the Z^0 boson. Note that in scenarios with gaugino mass unification, first generation squarks are always much heavier than the lightest neutralino, suppressing their contributions to LSP–nucleon scattering. Chosing $m_0^2 \gg M_{1/2}^2$, as done here, further strengthens this hierarchy, so that Higgs and Z^0 exchange contributions largely determine the SI and SD cross sections, respectively.

The curves in Figs. 29 show a noticeable negative slope even away from this threshold. In case of the SI cross section, this is due to the reduction of the mass of the heavier neutral CP–even Higgs boson with decreasing M_X, which goes along with the reduction of the weak–scale gaugino masses (although for fixed m_0 the ratio $m_A/m_{\tilde{\chi}_1^0}$ slightly increases with decreasing M_X [18]). Note also that decreasing $m_{\tilde{\chi}_1^0}$ requires a simultaneous, if slower, decrease of μ, since otherwise the higgsino–component of $\tilde{\chi}_1^0$ would become too small, yielding too small an annihilation cross section. This decrease of both weak–scale gaugino masses and of μ with decreasing M_X implies that the higgsino components of the LSP become more different in magnitude; note that they become identical in size for $|\mu| \gg M_Z$. This in turn enhances the $\tilde{\chi}_1^0 \tilde{\chi}_1^0 Z^0$ coupling, which is proportional to the difference of the squares of these components [2, 3].

Figs. 30 show results analogous to those in Fig. 29, except that now the gaugino mass parameter $M_{1/2}$ has been varied along with M_X such that the LSP mass is kept

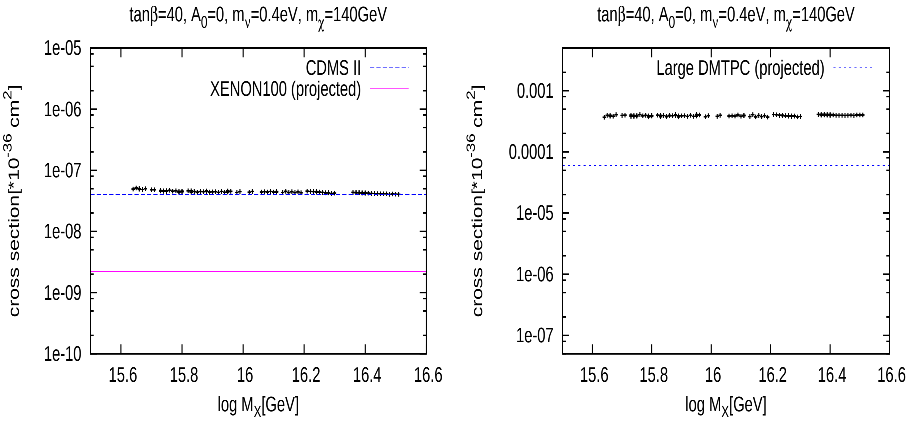

Figure 30: As Fig. 29, except that $M_{1/2}$ has also been varied along with M_X, such that the mass of the lightest neutralino is kept fixed at 140 GeV.

fixed. This required taking larger values of $M_{1/2}$ for smaller M_X. As expected from our previous discussion, the effect of reducing M_X is now quite small. The spin–independent cross section (left frame) increases by $\sim 20\%$ as M_X is reduced to its minimal value. This can be explained as follows. Since now $m_{\tilde{\chi}_1^0}$ is kept fixed, we also have to keep μ essentially fixed in order to maintain the correct relic density. This requires reducing m_0 when M_X is reduced. This in turn leads to a reduction of m_A, which over–compensates the increase of m_A that would result if M_X were reduced for fixed m_0 and fixed LSP mass. This implies a similar reduction for the mass of the heavier CP–even neutral Higgs boson whose exchange plays a prominent role in this cross section. However, it is not clear whether this variation is significant given astrophysical and likely experimental uncertainties. The variation of the spin–dependent cross section is even smaller.

Fig. 31 shows the same cross sections for smaller (heaviest) neutrino mass, $m_\nu = 0.2$ eV, as well as larger gaugino mass, $M_{1/2} = 1$TeV. Recall that the smaller m_ν requires a larger Yukawa coupling Y_N, which, among other things, reduces the weak–scale $\tilde{\tau}$ masses. This allows to satisfy the relic density constraint (247) for two distinct choices of m_0. We continue to call the choice with $m_0^2 \gg M_{1/2}^2$, and resulting sizable higgsino component of the LSP, the "focus point" [89], even though the $SO(10)$ model does not show "focusing" behavior of any Higgs soft breaking mass [18]. In the "co-annihilation" region the relic density is largely determined by $\tilde{\chi}_1^0 - \tilde{\tau}_1$ co–annihilation [78] in both mSUGRA and the $SO(10)$ model.

For the focus point, we find the SI cross section to be almost independent of M_X. Note that $m_{\tilde{\chi}_1^0}$ is now well above m_t in the entire range of M_X shown. Moreover, m_A increases with decreasing m_ν [18]; the decrease of m_A with decreasing M_X is therefore less pronounced than in Fig. 29. Finally, reducing the LSP mass increases the annihilation cross

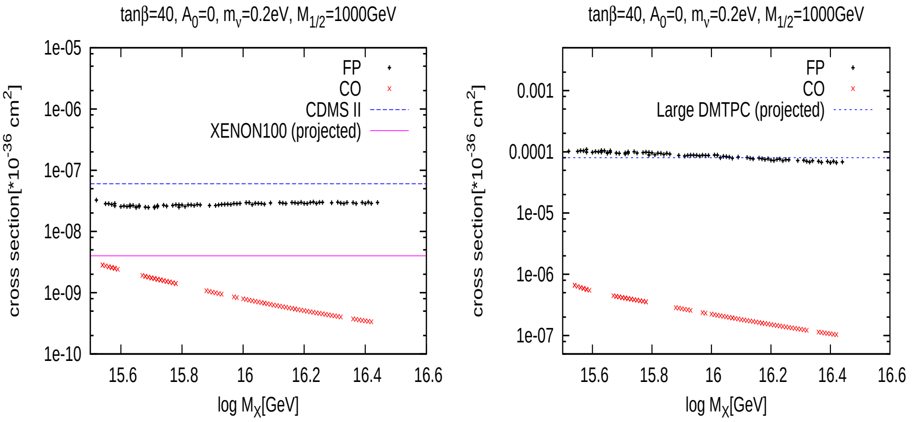

Figure 31: Dependence of the SI (a) and SD (b) neutralino–proton scattering cross section on M_X, for $m_\nu = 0.2$ eV. We chose two points that represent the "focus point" ("FP") region (black) and the "co–annihilation" ("CO") (red) region. The neutralino mass varies between 220 GeV and 390 GeV at the smallest and largest M_X, respectively. The experimental constrains are taken for $m_\chi = 220$ GeV, and scale essentially like $m_{\tilde{\chi}_1^0}$.

section, which scales like $m_{\tilde{\chi}_1^0}^{-2}$ away from thresholds. In compensation, gaugino–higgsino mixing has to be reduced. This reduces the LSP couplings to neutral Higgs bosons, offsetting the effect of the reduction of m_A as far as the SI cross section is concerned. In the SD case, we again observe a slight increase of the cross section with decreasing M_X, as in Fig. 29 away from the $t\bar{t}$ threshold. Note also that, in spite of the increased LSP mass, the "focus point" scenario remains easily testable by near–future direct search experiments, at least via the SI cross section.

On the other hand, for the co–annihilation point, both the SI and SD cross sections increase by one order of magnitude when M_X is reduced to its smallest allowed value. Here the Dark Matter relic density is mainly determined by the mass difference between the LSP and the lightest stau, which does not strongly depend on μ. Instead, the correct relic density is obtained through the direct effect of m_0 on $m_{\tilde{\tau}_1}$. Due to the strong (exponential) dependence of the relic density on the $\tilde{\chi}_1^0 - \tilde{\tau}_1$ mass splitting, only relatively minor adjustments of m_0 are required, which do not lead to significant changes of μ. In contrast, the additional Yukawa couplings in the $SO(10)$ model reduce $|\mu|$ all over the parameter space. Therefore, in the co–annihilation region the larger higgsino component of $\tilde{\chi}_1^0$ gives rise to larger scattering amplitudes, in particular via the Higgs– and Z^0–exchange diagrams that dominate the SI and SD cross sections, respectively. The SI cross section is enhanced in addition by the decreasing m_A. As a result, at the smallest value of M_X this cross section even approaches the XENON100 sensitivity.

In order to understand the strong dependence of these cross sections on M_X, one has

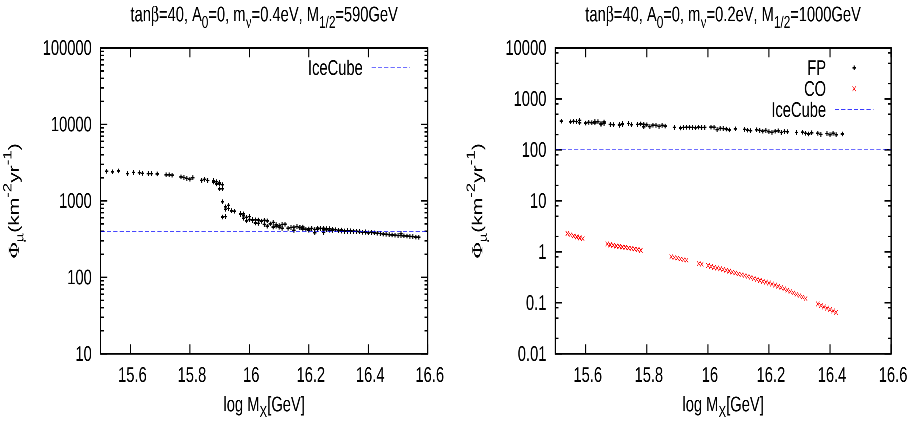

Figure 32: Neutrino–induced muon flux from neutralino annihilation in the Sun as a function of M_X for (a) $m_\nu = 0.4$ eV; (b) $m_\nu = 0.2$ eV. The IceCUBE sensitivity limits are for the smallest LSP mass in the respective frames; in the relevant range of masses, the sensitivity limit scales roughly $\propto 1/m_{\tilde{\chi}_1^0}$.

to keep in mind that reducing M_X increases the effect of the new Yukawa coupling Y_N in two ways. First, reducing M_X reduces the intermediate scales M_R and M_C even more, i.e. $\ln(M_X/M_C)$ and $\ln(M_X/M_R)$ increase when M_X is decreased. This increases the energy range where this coupling is effective in the RGE. Secondly, the reduction in M_R has to be compensated by an increase of Y_N in order to keep the very large Majorana neutrino mass in the seesaw expression (24) constant.

In Fig. 32 we plot the resulting muon flux as function of M_X, and compare it to the "best case" sensitivity of IceCUBE [90], using the input parameters of Fig. 29 (left frame) and Fig. 31 (right). Note that the overall neutrino flux is essentially fixed by the capture rate. The neutralinos interact with nuclei in the Sun mostly via Higgs and Z^0 exchange. The capture rate is thus again sensitive to the higgsino components of the mostly bino–like neutralinos. It also depends on the mass of the neutralinos: the heavier the LSP, the less likely it is to lose enough energy in the interaction to become gravitationally bound to the Sun. The predicted muon flux therefore increases faster with decreasing M_X than the cross sections shown in Figs. 29 and 31 do.

The muon flux also depends on the (mean) neutrino energy, since the neutrino charged current cross section increases with energy. Annihilation into pairs of $W^\pm$ or Z^0 bosons leads to the hardest neutrino spectra, and hence to the largest signals. Annihilation into $t\bar{t}$ gives a somewhat softer spectrum, since some of the energy is taken away by the $b-$quarks. This enhances the effect of the $t\bar{t}$ threshold visible in the left frame: to the left of this threshold, neutralinos predominantly annihilate directly into massive gauge bosons, while to the right of the threshold, annihilation into $t\bar{t}$ dominates.

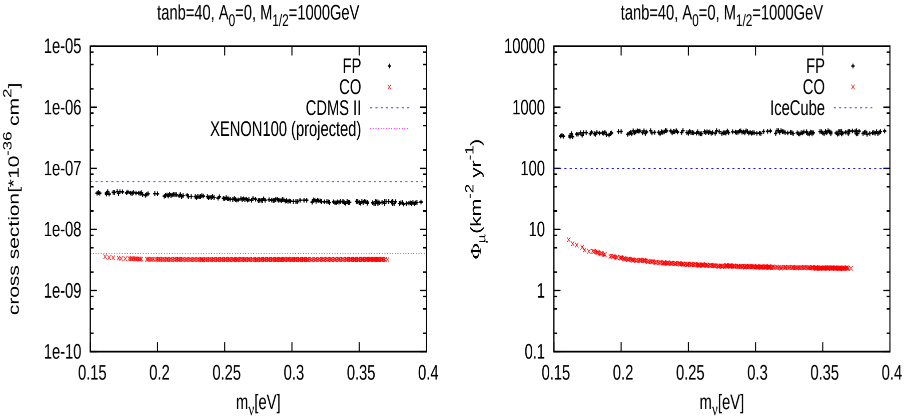

Figure 33: (a) SI neutralino–proton scattering cross section and (b) neutrino–induced muon flux from neutralino annihilation in the Sun, as function of m_ν.

Of course, the neutrino energy also scales with the mass of the annihilating neutralinos. Indeed, the sensitivity limit on the muon flux decreases with increasing LSP mass for $m_{\tilde{\chi}_1^0} \lesssim 500$ GeV [90]. However, in the muon flux itself this effect is compensated by the reduction of the neutralino flux impinging on the Sun, which scales like $1/m_{\tilde{\chi}_1^0}$. Nevertheless, this effect keeps the expected flux in the "focus point" region well above the sensitivity limit even for the larger value of $M_{1/2}$ chosen in the right frame. However, the flux in the co–annihilation region remains well below the IceCUBE sensitivity even for the smallest possible value of M_X.

In Fig. 33, we show the SI proton–neutralino cross section as well as the neutrino–induced muon flux as function of m_ν, for $M_X = 10^{15.5}$ GeV. We see that in the FP region, the cross section slightly increases with decreasing m_ν. Recall that decreasing m_ν, i.e. increasing the coupling Y_N, reduces μ. In order to keep the relic density fixed one has to increase μ again by decreasing m_0, which in turn leads to a decrease of the Higgs boson masses; this overcompensates the increase of m_A with decreasing m_ν if all soft breaking parameters are kept fixed. The reduced Higgs boson masses increase the scattering cross section. However, it also increases the importance of the $A-$exchange contribution to the $\tilde{\chi}_1^0$ annihilation cross section at rest. For $\tan\beta \gg 1$, $A-$exchange mostly leads to $b\bar{b}$ final states, which produce very soft neutrinos. This effect over–compensates the (small) increase in the neutralino capture cross section, leading to a (very slight) decrease of the muon flux with decreasing m_ν in the FP region.

In the co–annihilation region, increasing the Yukawa coupling Y_N reduces $m_{\tilde{\tau}_R}$ as well as μ. The two effects tend to cancel, but a net reduction of $m_{\tilde{\tau}_1}$ results. This has to be compensated by increasing m_0 in order to keep the relic density in the desired range. This, as well as the effect of Y_N in the RGE, increases m_A. The increase of m_A and the decrease

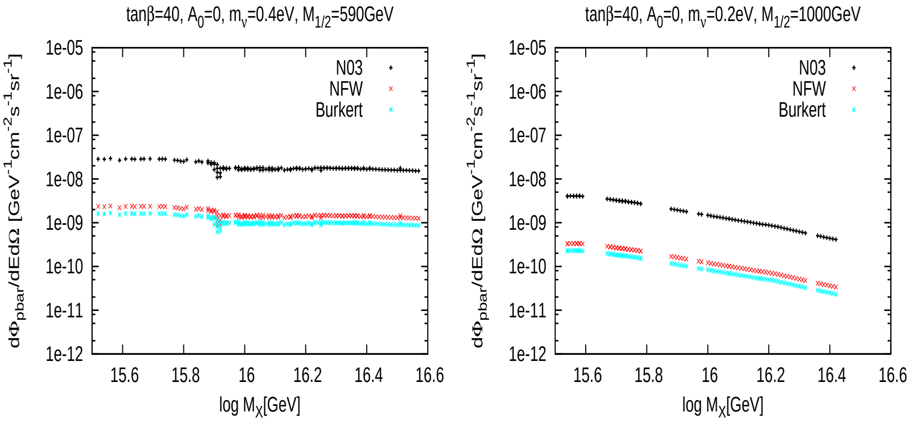

Figure 34: Antiproton differential flux for different halo models for (a) $m_\nu = 0.4$ eV ("focus-point") and (b) $m_\nu = 0.2$ eV ("co-annihilation").

of μ essentially cancel in the SI cross section. However, increasing m_A also reduces the importance of neutralino annihilation to $b\bar{b}$. This increases the average neutrino energy, which explains the slight increase of the muon flux with decreasing m_ν.

We have also computed the near–Earth flux of antiprotons due to the annihilation of relic neutralinos in the halo of our galaxy. As well known, the flux depends sensitively on several poorly known astrophysical quantities. One of these is the density of Dark Matter, which is reasonably well known "locally", but not near the center of the galaxy, where it is largest. Note that, unlike positrons, antiprotons can diffuse from the galactic center to Earth. We illustrate this uncertainty by comparing three different halo models. The "N03" profile has been derived [91] starting from a profile extrapolated from $N-$body simulations [92], assuming that baryon infall compresses the Dark Matter distribution near the galactic center adiabatically. In the opposite extreme, one can assume that baryon infall heats the dark halo, leading [91] to a profile similar to the (phenomenologically apparently quite successful) "Burkert" profile [93]. Finally, the "NFW" profile [94] lies between these extremes.

Fig. 34 shows the dependence of the antiproton flux on M_X. Antiprotons are produced in the Galactic halo due to the hadronization of antiquarks produced in neutralino Dark Matter annihilation. As a result, the typical $\bar{p}$ energy is well below $m_{\tilde{\chi}_1^0}$. We show their differential flux at a kinetic energy 20 GeV, where the signal–to–background ratio is expected to be optimal [95]. We illustrate the dependence on the halo model using the three profiles discussed above.

The left frame of Fig. 34 is for the "focus point" region, with small Y_N and relatively small $M_{1/2}$. In this case the relic density is determined by $\tilde{\chi}_1^0$ annihilation with itself, and is dominated by annihilation from the $S-$wave, which is the only contribution relevant for the $\bar{p}$ flux. As a result, the $\tilde{\chi}_1^0$ annihilation cross section remains essentially constant in the left frame. However, we saw in Fig. 29, where the same parameters were used, that $m_{\tilde{\chi}_1^0}$ decreases by nearly a factor of two as M_X is decreased. This increases the $\tilde{\chi}_1^0$ annihilation rate, computed as the product of flux and cross section, by almost a factor of four. However, decreasing $m_{\tilde{\chi}_1^0}$ also makes it increasingly more difficult to produce antiprotons at 20 GeV. As a result, the $\bar{p}$ flux near Earth only increases very slightly as M_X is decreased.

The right frame shows results for a point in the co–annihilation region, with larger $M_{1/2}$ and smaller m_ν. Here the relic density is essentially determined by $\tilde{\tau}_1 - \tilde{\chi}_1^0$ co–annihilation. The annihilation cross section increases significantly with decreasing M_X, due to the decrease of (almost) all weak–scale sparticle and Higgs boson masses. Moreover, $m_{\tilde{\chi}_1^0}$ now remains so high that getting 20 GeV antiprotons is not difficult. As a result, the rate increases by about an order of magnitude as M_X is reduced to its lower bound.

This seems impressive, but is still smaller than the difference in the predictions based on the N03 and Burkert profiles. Additional systematic uncertainties come from the propagation of the antiprotons; here we have used `DarkSUSY` default parameters. Note finally that the $\bar{p}$ flux that can be inferred from the $\bar{p}/p$ ratio measured by the PAMELA satellite [96] and the well–known [5] proton flux is about $2 \cdot 10^{-7}$ GeV^{-1}cm^{-2}s^{-1}sr^{-1}, well above even the most optimistic prediction in Fig. 34. Given that the prediction for the background also has sizable uncertainties, we conclude that the observation of cosmic antiprotons is not a very promising test of the models discussed here.

Prospects for direct and indirect DM search in the $SO(10)$ model with the smallest allowed M_X are summarized in Fig. 35, for two different values of m_ν. The regions of parameter space that give a neutrino–induced muon flux from $\tilde{\chi}_1^0$ annihilation in the Sun above the IceCUBE sensitivity limit are depicted as light blue. The regions where the spin–independent neutralino–proton cross section exceeds the CDMS–II bound are shown in magenta. Note that we always assume fixed local neutralino density when deriving these bounds, independent of the predicted value of $\Omega_{\tilde{\chi}_1^0} h^2$. We also show the region excluded by the electroweak symmetry breaking (EWSB) condition or by too light sfermions (grey) as well as that excluded by the LEP limits [5] on the masses of Higgs bosons and charginos (scarlet). The black points are where the Dark Matter relic density satisfies Eq. (247).

We find that, as in mSUGRA [97], the region of high m_0, where $\tilde{\chi}_1^0$ has a sizable higgsino component, will soon be covered by direct searches and also by the neutrino indirect search. Recall from Figs. 33 that the region of parameter space to be probed by XENON100 is much larger than that probed by IceCUBE. Compared to mSUGRA, for given $M_{1/2}$, A_0 and $\tan\beta$ this region occurs at significantly lower values of m_0; this is true in particular for small m_ν, i.e. sizable Yukawa coupling Y_N (right frame). Moreover, in

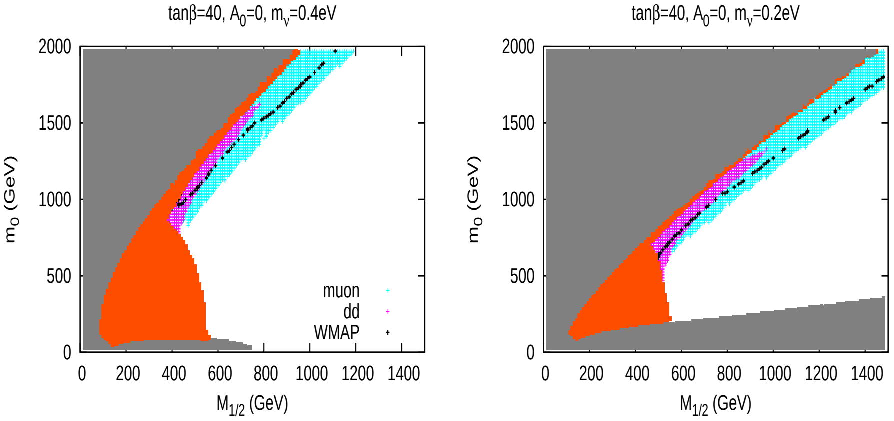

Figure 35: Regions in the $(M_{1/2}, m_0)$ plane for (a) $m_\nu = 0.4$ eV; (b) $m_\nu = 0.2$ eV. The grey area is excluded by the EWSB condition or by too light sfermions, and the scarlet area is excluded by the LEP limits on Higgs and chargino masses. The black points give us the correct Dark Matter relic density. The light blue region can be tested by searching for muon neutrinos originating from $\tilde{\chi}_1^0$ annihilation in the Sun, while in the magenta region, the $\tilde{\chi}_1^0 p$ scattering cross section exceeds the CDMS–II bound. The dependence of the detectability on the WIMP mass is taken into account, but we assume a fixed local WIMP density.

this region neutralino Dark Matter remains detectable out to much larger values of $M_{1/2}$ than in mSUGRA, since the ratio $m_{\tilde{\chi}_1^0}/M_{1/2}$ is nearly two times smaller in our scenario than in mSUGRA.

The co–annihilation region is difficult to see in Figs. 35, since it is very narrow. It extends to $M_{1/2} \simeq 750$ (1400) GeV for $m_\nu = 0.4$ (0.2) eV. Unfortunately this region will not be tested by near–future Dark Matter search experiments. However, we saw in Fig. 31 that the $\tilde{\chi}_1^0 p$ scattering cross section exceeds that in mSUGRA by about an order of magnitude. Much of this region will therefore be testable by ton–scale direct Dark Matter detection experiments.

4 Summary and Conclusion

In this thesis, we have studied the collider signatures as well as the relic density and detectability of Dark Matter in well-motivated models beyond the minimal supersymmetric Standard Model.

In Chap. 2, we first discussed the collider signals from SUGRA–GUT model, by investigating an SUSY–SO(10) model with two intermediate scales in detail, in comparison to those from the mSUGRA. The model remains sufficiently similar to mSUGRA that the overall search prospects were essentially the same, so we focused on ways to distinguish the model from mSUGRA. We chose two benchmark points, and showed that events containing hard jets and two (or more) charged leptons can be used to discriminate the mSUGRA and the SO(10) model.

On the other hand, the phenomenology of $N = 1/N = 2$ hybrid model was charateristically distinct. In Sec. 2.4.2, we analyzed the production and the decay of the color–octet scalar, a component of the $N = 2$ gauge hypermultiplet. It led to spectacular signatures such as multi–jet final states with high sphericity and large missing transverse momentum, or four top quarks at the LHC. The novel gauginos in $N = 2$ hypermultiplets were combined with the MSSM gauginos and formed Dirac gauginos. In electroweak sector, as a consequence, three charginos and three (Dirac) neutralinos appeared in the Dirac limit. In Sec. 2.4.3, we have shown that the Majorana or Dirac nature of neutralinos can be distinguished in the sfermion pair production and/or the charginos/neutralinos pair production in the hadron collider as well as in the linear collider. The electroweak adjoint scalars mix with the Higgs fields, and gave us three neutral pseudoscalar, four neutral scalar, and three pairly-charged states. The $U(1)_Y$ scalar state can be produced in pp collisions, and the charged isovector states in e^+e^- collisions. Also, the $\gamma\gamma$ collision offer production channels for all neutral adjoint states.

In Sec. 3.1, we calcuated the Dark Matter relic density. We considered the one–loop corrections to the WIMP annihilation cross section, due to the exchange of a relatively light boson between WIMPs. Then in Sec. 3.2, we discussed the direct and indirect Dark Matter search experiments, taking the neutralino Dark Matter in the SO(10) model in Sec. 2.3.2 as an example. We have shown that in the cosmologically allowed region with large scalar mass parameter m_0 in the model, the direct detection as well as the indirect detection of Dark Matter through neutrinos should be possible for the next generation of detectors.

The LHC finally has begun to operate, albeit yet with the smaller center of mass energy than planned. The PLANCK satellite [15] will image the Cosmic Background Radiation anisotrpies with a very high sensitivity and angular resolution. Furthermore, there are a number of astrophysical experiments under the ground (e.g. IceCUBE [90], DAMA/LIBRA [99], CDMS [17], EDELWEISS [14], KIMS [98], and many others) and in the sky (e.g. PAMELA [96], Fermi-LAT satellites [100], ATIC Balloon [101]). By combining all the information, we will hopefully be able to pin down the physics at the Grand Unified scale and higher.

A Parametrizations of the thermal averages

The thermal average of the correction to the $S-$wave annihilation cross section is given by

$$\begin{aligned} \langle \delta\sigma_S v\rangle &= \frac{x^{3/2}}{2\pi^{1/2}}\int_0^\infty v^2\left(\frac{g^2}{2\pi^2 v}I_S(v)(\sigma_{0,S}v)\right)\mathrm{e}^{-xv^2/4} \\ &= \frac{g^2x^{3/2}}{4\pi^{5/2}}\cdot\mathscr{A}\cdot\int_0^\infty v^2\left(\frac{I_S(v)}{v}\right)\mathrm{e}^{-xv^2/4}\,. \end{aligned} \tag{A.1}$$

$\mathscr{A}$ has been defined via the non–relativistic expansion of σv in Eq. (218). The $v-$dependence of I_S can be read off in Eq. (236):

$$I_S(v)\simeq\begin{cases}\frac{2\pi v\sqrt{u^2+v^2}}{u^2+2v^2}, & v\leq\frac{u}{2.4}\\ \frac{\pi^2/2}{1+\frac{u}{\pi v}+\frac{u^2}{\pi^2v^2}}, & v>\frac{u}{2.4}\end{cases}\,. \tag{A.2}$$

Here we have introduced the quantity $u=2\mu/m_\chi$. We showed in Sec. 3.1.2 that the integral in Eq. (A.1) is a function of the variable $z=u\sqrt{x}$. We find the following fitting function for the "thermally averaged" (I_S/v), defined as the integral in the last line of Eq. (A.1):

$$\langle\frac{I_S}{v}\rangle_{\rm fit}=\frac{1}{x}\left(\frac{1}{a_Sz^2+b_Sz+c_S}+d_S\right), \tag{A.3}$$

with

$$a_S=0.000593;\;\; b_S=0.03417;\;\; c_S=0.1015;\;\; d_S=0.1182. \tag{A.4}$$

For the $P-$wave,

$$\begin{aligned} \langle \delta\sigma_P v\rangle &= \frac{x^{3/2}}{2\pi^{1/2}}\int_0^\infty v^2\left(\frac{g^2}{2\pi^2 v}I_P(v)(\sigma_{0,P}v)\right)\mathrm{e}^{-xv^2/4} \\ &= \frac{g^2x^{3/2}}{4\pi^{5/2}}\cdot\mathscr{B}\cdot\int_0^\infty v^2\left(v^2\cdot\frac{I_P(v)}{v}\right)\mathrm{e}^{-xv^2/4}, \end{aligned} \tag{A.5}$$

with

$$I_P(v)\simeq\begin{cases}\frac{2\pi v\left(u^2+2.3v^2\right)}{3(u^2+v^2)^{3/2}}, & v\leq\frac{u}{2.1}\\ \frac{\pi^2/2}{1+\frac{3u}{\pi v}+\frac{u^2}{\pi v^2}}, & v>\frac{u}{2.1}\end{cases}\,. \tag{A.6}$$

As above, we find a fitting function for the "thermally averaged" (vI_P):

$$\langle vI_P\rangle_{\rm fit}=\frac{16}{x^2}\left(\mathrm{e}^{-a_Pz-b_P}+\frac{1}{c_Pz+d_P}\right), \tag{A.7}$$

with

$$a_P=0.318;\;\; b_P=0.1226; c_P=0.3309; d_P=0.6306. \tag{A.8}$$

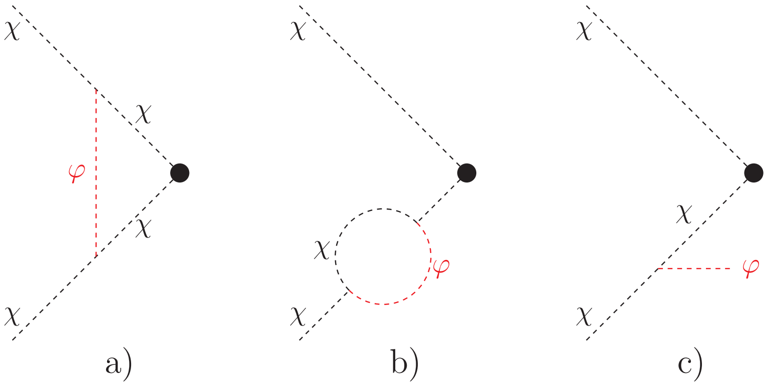

Figure 36: Feynman diagrams describing full initial state radiative corrections: vertex correction (a), wave function renormalization (b) and real emission (c); wave function renormalization of, and emission off, the upper leg also has to be included. The WIMP χ and the exchanged boson φ are denoted by black and red dashed lines, respectively, while the blob denotes the $\chi\chi$ annihilation vertex, which is independent of the χ momenta.

B Comparison to a full one-loop calculation

In this Appendix we compare our approximate treatment of corrections due to φ exchange with a full one–loop calculation. We do this in the framework of a purely scalar theory, where the exact vertex correction is UV finite. As we remarked in Sec. 3.1.2, our formalism will not capture corrections associated with the renormalization of the coupling(s) relevant for WIMP annihilation, so chosing an example with UV–finite vertex correction greatly simplifies the comparison to the full one–loop calculation.

The Feynman diagrams describing exact one–loop corrections associated with the initial state are shown in Fig. 36. Here the blob describes the (tree–level) χ annihilation process; this could e.g. be a quartic vertex involving two lighter scalars, or a trilinear vertex coupling to the $s-$channel propagator of another scalar particle. For the purpose of our calculation we only need to know that the rest of the diagram described by the blob is independent of the loop momentum. We describe the $\varphi\chi\chi$ vertex by the (dimensionful) coupling κ.

Let us begin by computing the vertex correction; recall that this is the only diagram that contributes in the approximate treatment of Sec. 3.1.2. It gives:

$$\frac{A_{\text{vertex}}}{A_0} = i\kappa^2 \int \frac{d^4q}{(2\pi)^4} \frac{1}{(P+q)^2 - m_\chi^2} \frac{1}{(P-q)^2 - m_\chi^2} \frac{1}{(p-q)^2 - \mu^2} \,. \tag{B.9}$$

Here A_0 is the tree–level matrix element described by the blob in Fig. 36. Recall that $P = (p_1 + p_2)/2, \ p = (p_1 - p_2)/2$, where $p_{1,2}$ are the 4–momenta of the incoming WIMPs,

μ is the mass of φ, and κ is the $\chi\chi\varphi$ coupling.

The loop integral in Eq. (B.9) can be computed straightforwardly using Feynman parameters, giving

$$\frac{A_{\text{vertex}}}{A_0} = -\frac{\kappa^2}{16\pi^2} C_0(s, m_\chi^2, m_\chi, m_\chi, \mu^2)\,. \tag{B.10}$$

Here C_0 is the scalar Passarino–Veltman three–point function in the convention of [86].

The loop integral in Eq. (B.9) can also be evaluated directly, following the steps of Sec. 3.1.2 but without making any approximations in the propagators. We first perform the energy (q_0) integrals by contour integration, by summing over the residues of all poles in the lower half plane. In general, there are three such poles:

$$\begin{aligned} q_0^{\text{pole 1}} &= \omega - P_0\,; \\ q_0^{\text{pole 2}} &= \omega + P_0\,; \\ q_0^{\text{pole 3}} &= \sqrt{(\vec{p} - \vec{q})^2 + \mu^2}\,, \end{aligned} \tag{B.11}$$

where $\omega = \sqrt{\vec{q}^{\,2} + m_\chi^2}$ as in Eq. (228). Only the first pole has a residue that diverges in the limit $\vec{p}, \vec{q} \to 0$. The third pole comes from the energy dependence of the φ propagator, which has been ignored in the approximate treatment of Sec. 3.1.2. The angular integrals can also be performed straightforwardly. After some algebra, we arrive at:

$$\begin{aligned} \frac{A_{\text{vertex}}}{A_0} &= \frac{\kappa^2}{16\pi^2}\frac{1}{4P_0|\vec{p}|}\int_0^\infty |\vec{q}|d|\vec{q}| \left[\frac{1}{\omega(\omega - P_0)} \ln\frac{(|\vec{p}| + |\vec{q}|)^2 + \mu^2 - (\omega - P_0)^2}{(|\vec{p}| - |\vec{q}|)^2 + \mu^2 - (\omega - P_0)^2}\right. \\ &- \frac{1}{\omega(\omega + P_0)} \ln\frac{(|\vec{p}| + |\vec{q}|)^2 + \mu^2 - (\omega + P_0)^2}{(|\vec{p}| - |\vec{q}|)^2 + \mu^2 - (\omega + P_0)^2} \\ &+ \left.\frac{1}{\omega_\varphi^2}\left(\ln\frac{\mu^2 + 2|\vec{p}||\vec{q}| - 2P_0\omega_\varphi}{\mu^2 - 2|\vec{p}||\vec{q}| - 2P_0\omega_\varphi} - \ln\frac{\mu^2 + 2|\vec{p}||\vec{q}| + 2P_0\omega_\varphi}{\mu^2 - 2|\vec{p}||\vec{q}| + 2P_0\omega_\varphi}\right)\right]\,. \end{aligned} \tag{B.12}$$

In the last line, we have introduced $\omega_\varphi = \sqrt{\vec{q}^{\,2} + \mu^2}$.

It is easy to see that the first term reduces to our expression (230) if we use the non–relativistic expansion for ω, which includes dropping the terms $(\omega - P_0)^2$ in the argument of the logarithm. However, for large $|\vec{q}|$ these latter terms are important. They imply that the logarithm approaches the constant value $2|\vec{p}|/P_0$ in the limit $|\vec{q}| \to \infty$, rather than vanishing as in Eq. (230). As a result, the first line of the right–hand side of Eq. (B.12) by itself is logarithmically UV–divergent. The second line contributes the same UV divergence again; only after adding the contribution in the third line we obtain a UV–finite result. This third line comes from the third pole in Eq. (B.11), which does not exist if one drops the energy dependence of the φ propagator, as in Sec. 3.1.2.. This proves our statement in Sec. 3.1.2. that omission of the energy dependence of the φ propagator necessitates the use of a non–relativistic expansion in the argument of the loop integral.

While the third line in Eq. (B.12) is necessary to obtain a UV–finite result, it introduces a new problem: for $\mu \to 0$ it becomes IR–divergent! In the limit $\mu^2 \ll m_\chi^2$, $|\vec{p}| \ll P_0$ the last line of Eq. (B.12) simplifies to

$$\frac{16P_0|\vec{p}||\vec{q}|}{\sqrt{\vec{q}^2+\mu^2}}\frac{1}{\mu^4-4P_0^2\left(\vec{q}^2+\mu^2\right)}\,.$$

The $d|\vec{q}|$ integration will then lead to a *negative* term $\propto \ln\frac{|\vec{q}|_{\max}}{\mu}$. As noted earlier, the UV divergence for $|\vec{q}|_{\max}\to\infty$ precisely cancels those from the first two terms in Eq. (B.12). The resulting term $\propto \ln\frac{m_\chi}{\mu}$ in the exact vertex correction is IR–divergent for $\mu\to 0$. This term becomes significant for small μ, especially if the velocity v is not too small. This explains our statement in Sec. 3.1.2. that our approximation does *not* describe the exact vertex correction very well for small μ.

However, the IR divergence does not exist in the *full* one–loop calculation. We have to add wave function renormalization (Fig. 36b) as well as real emission diagrams (Fig. 36c) in order to obtain an IR–finite result for $\mu\to 0$. This implies that adding these additional contributions should also remove all terms $\propto \ln\frac{m_\chi}{\mu}$ in the complete one–loop corrected cross section. Using on–shell renormalization for χ, the wave function renormalization constant Z_χ is finite:[21]

$$Z_\chi = \frac{\kappa^2}{16\pi^2}B_0'(m_\chi^2, m_\chi, \mu)\,, \tag{B.13}$$

where B_0' is the derivative of the scalar Passarino–Veltman two–point function with respect to its first argument. Adding this negative contribution *doubles* the IR–divergence for $\mu\to 0$.

Finally, we have to treat the real φ emission diagram of Fig. 36c, plus the contribution where φ is emitted off the other χ line. Writing the 4–momentum of the emitted φ as $k=(k_0,\vec{k})$, we have

$$\frac{|A_{\text{real em.}}|^2}{|A_0|^2} = \kappa^2\left|\frac{2\left(\mu^2-2k_0P_0\right)}{\left(\mu^2-2k_0P_0\right)^2-4\left(\vec{k}\cdot\vec{p}\right)^2}\right|^2\,. \tag{B.14}$$

Performing the angular integrations of the φ phase space, this gives

$$\begin{aligned}\frac{\sigma_{\text{real em.}}}{\sigma_0} &= \frac{\kappa^2}{2\pi^2}\int_\mu^{k_{0,\max}} dk_0\left[\frac{|\vec{k}|}{\left(2P_0k_0-\mu^2\right)^2-4\vec{k}^2\vec{p}^2}\right.\\ &\qquad\left.+\frac{1}{4|\vec{p}|\left(2P_0k_0-\mu^2\right)}\ln\frac{2k_0P_0-\mu^2+2|\vec{k}||\vec{p}|}{2k_0P_0-\mu^2-2|\vec{k}||\vec{p}|}\right]\,,\end{aligned} \tag{B.15}$$

where $|\vec{k}|=\sqrt{k_0^2-\mu^2}$ and $k_{0,\max}=P_0+\mu^2/(4P_0)$. In the limit $\mu\to 0$ this also produces a logarithmic IR divergence, this time with positive sign, which (not surprisingly) cancels the sum of the IR divergent terms from the vertex correction and wave function renormalization.

---

[21] Diagram 36b also gives a logarithmically divergent contribution to m_χ. This is simply removed by the mass counterterm in on–shell renormalization.

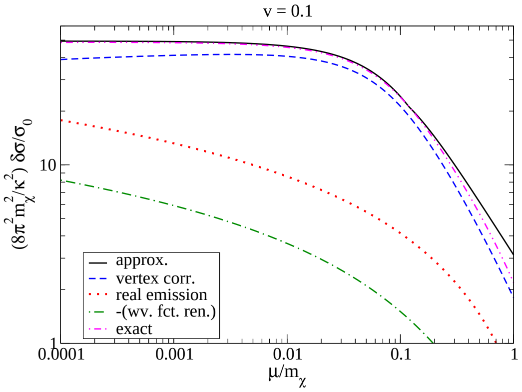

Figure 37: Normalized higher order contributions to the χ annihilation cross section for relative initial state velocity $v = 0.1$. The solid (black) curve shows our approximation of Sec. 3.1.2, given by I_S/v. The dashed (blue), dotted (red) and dot–dashed (green) curves show exact contributions from vertex corrections, real emission diagrams, and wave function renormalization, respectively; the latter has to be multiplied with -1. The dash–doubledotted (magenta) curve shows the sum of these three contribution, i.e. the exact one–loop correction; it nearly coincides with the black curve for $\mu/m_\chi \leq 0.2$.

Fig. 37 shows that the sum of the vertex correction, wave function renormalization and real emission contributions very closely matches our approximate result of Sec. 3.1.2 for $\mu \lesssim 0.5 m_\chi$. In fact, the difference is always of order $\kappa^2/(8\pi^2 m_\chi^2)$, without any potentially large factors like $1/v$ or $\ln(m_\chi/\mu)$. We checked that this remains true at least for all $v \lesssim 0.5$ relevant for the calculation of the relic density.[22] It is not surprising that our approximate treatment does not treat such “generic” higher order contributions correctly. However, our approximation does closely resemble the exact result whenever the latter is large. This is all we aspired to, and in most cases all we need when calculating DM relic densities, even if PLANCK data reduce the uncertainty of the observed value to the percent level.

---

[22] Our approximation might fail badly when the annihilating WIMPs become ultra–relativistic, but this is of no concern in the present context.

References

[1] H. P. Nilles, Phys. Rept. **110** (1984) 1; H. E. Haber and G. L. Kane, Phys. Rept. **117** (1985) 75.

[2] M. Drees, R. Godbole and P. Roy, *Theory and phenomenology of sparticles: An account of four-dimensional N=1 supersymmetry in high energy physics*, Hackensack, USA: World Scientific (2004);

[3] H. Baer and X. Tata, *Weak scale supersymmetry: From superfields to scattering events*, Cambridge, UK University Press (2006).

[4] P. Fayet, Nucl. Phys. B **113** (1976) 135; L. Álvarez-Gaumé and S. F. Hassan, Fortsch. Phys. **45** (1997) 159 [arXiv:hep-th/9701069].

[5] C. Amsler et al. (Particle Data Group), Phys. Lett. B667, 1 (2008)

[6] Y. Fukuda *et al.* [Super-Kamiokande Collaboration], Phys. Rev. Lett. **81** (1998) 1562 [arXiv:hep-ex/9807003].

[7] For a review, see G. Bertone, D. Hooper and J. Silk, Phys. Rept. **405** (2005) 279 [arXiv:hep-ph/0404175].

[8] R. Haag, J. T. Lopuszanski and M. Sohnius, Nucl. Phys. B **88** (1975) 257.

[9] J. Terning, *Modern Supersymmetry*, Oxford, Clarendon Press (2006)

[10] P. J. Fox, A. E. Nelson and N. Weiner, JHEP **0208** (2002) 035 [arXiv:hep-ph/0206096].

[11] J. C. Pati and A. Salam, Phys. Rev. D. **10** (1974) 275.

[12] D. Clowe, M. Bradac, A. H. Gonzalez, M. Markevitch, S. W. Randall, C. Jones and D. Zaritsky, Astrophys. J. **648** (2006) L109 [arXiv:astro-ph/0608407].

[13] WMAP Collab., E. Komatsu et al., Astrophys. J. Suppl. **180** (2009) 330, arXiv:0803.0547 [astro-ph].

[14] E. Armengaud *et al.*, Phys. Lett. B **687** (2010) 294 [arXiv:0912.0805 [astro-ph.CO]].

[15] Planck Science Team, G. Efstathiou et al., “PLANCK: The Scientific Programme”, http://www.rssd.esa.int/SA/PLANCK/docs/Bluebook-ESA-SCI(2005)1_V2.pdf

[16] For a review, see G. Bertone, D. Hooper and J. Silk, Phys. Rept. **405** (2005) 279, [arXiv:hep-ph/0404175].

[17] Z. Ahmed *et al.* [The CDMS-II Collaboration], arXiv:0912.3592 [astro-ph.CO].

[18] M. Drees and J. M. Kim, JHEP **0812** (2008) 095 [arXiv:0810.1875 [hep-ph]].

[19] S. Y. Choi, M. Drees, J. Kalinowski, J. M. Kim, E. Popenda and P. M. Zerwas, Phys. Lett. B **672** (2009) 246 [arXiv:0812.3586 [hep-ph]].

[20] M. Drees, J. M. Kim and K. I. Nagao, arXiv:0911.3795 [hep-ph].

[21] S. Bertolini, F. Borzumati and A. Masiero, Phys. Lett. **B192** (1987) 437, and Nucl. Phys. **B294** (1987) 321.

[22] E. Barberio *et al.* [Heavy Flavor Averaging Group], arXiv:0808.1297 [hep-ex].

[23] F. Borzumati, C. Greub, T. Hurth and D. Wyler, Phys. Rev. D. **62** (2000) 075005.

[24] L.L. Everett, G.L. Kane, S. Rigolin, L.-T. Wang and T.T. Wang, JHEP **0201** (2002) 022.

[25] K.-i. Okumura and L. Roszkowski, Phys. Rev. Lett. **92** (2004) 161801.

[26] J.P. Miller, E. de Rafael, and B.L. Roberts, Rept. Prog. Phys. **70** (2007) 795.

[27] B.C. Allanach, A. Djouadi, J.L. Kneur, W. Porod and P. Slavich, JHEP **0409** (2004) 044; S. Heinemeyer, W. Hollik and G. Weiglein, Phys. Rept. **425** (2006) 265.

[28] I. Hinchliffe, F. E. Paige, M. D. Shapiro, J. Soderqvist and W. Yao, Phys. Rev. D **55** (1997) 5520 [arXiv:hep-ph/9610544].

[29] G. Aad *et al.* [The ATLAS Collaboration], arXiv:0901.0512 [hep-ex].

[30] B.C. Allanach, Comput. Phys. Commun. **143** (2002) 305-331.

[31] G. Bélanger, F. Boudjema, A. Pukhov and A. Semenov, Comput. Phys. Commun. **149** (2002) 103, [arXiv:hep-ph/0112278], and Comput. Phys. Commun. **174** (2006) 577, [arXiv:hep-ph/0405253].

[32] H. Fritzsch and P. Minkowski, Ann. Phys. **93** (1975) 193; M.S. Chanowitz, J. Ellis and M.K. Gaillard, Nucl. Phys. **B129** (1977) 506.

[33] P. Minkowski, Phys. Lett. B **67** (1977) 421

[34] C. S. Aulakh, B. Bajc, A. Melfo, A. Rasin and G. Senjanovic, Nucl. Phys. **B597** (2001) 89, [arXiv:hep-ph/0004031].

[35] See e.g. M. Davier, arXiv:1001.2243 [hep–ph]; T. Teubner, K. Hagiwara, R. Liao, A.D. Martin and D. Nomura, arXiv:1001.5401 [hep–ph]; and references therein.

[36] M. Drees and M.M. Nojiri, Phys. Rev. **D47** (1993) 376, [arXiv:hep-ph/9207234].

[37] M. M. Nojiri, Phys. Rev. D **51** (1995) 6281, [arXiv:hep-ph/9412374].

[38] B.K. Bullock, K. Hagiwara and A.D. Martin, Nucl. Phys. **B395** (1993) 499.

[39] R. M. Godbole, M. Guchait and D. P. Roy, Phys. Lett. **B618** (2005) 193, [arXiv:hep-ph/0411306].

[40] M. Guchait and D. P. Roy, Phys. Lett. **B541** (2002) 356, hep–ph/0205015.

[41] F. del Aguila and L. Ametller, Phys. Lett. **B261** (1991) 326; H. Baer, C.-h. Chen, F. Paige and X. Tata, Phys. Rev. **D49** (1994) 3283, hep–ph/9311248.

[42] H. Baer, C.-h. Chen, F. Paige and X. Tata, Phys. Rev. **D50** (1994) 4508, hep–ph/9404212.

[43] T. Sjöstrand, S. Mrenna and P. Skands, JHEP **0605** (2006) 026, hep–ph/0603175.

[44] M. Drees and M.M. Nojiri, Nucl. Phys. **B369** (1992) 54.

[45] F. E. Paige, S. D. Protopopescu, H. Baer and X. Tata, [arXiv:hep-ph/0312045].

[46] CMS Collab., A. De Roeck *et al.*, *CMS Physics Technical Design Report*, Vol. II, Sec. 11.3; see http://cdsweb.cern.ch/record/942733/files/lhcc-2006-021.pdf

[47] K. Benakli and M. D. Goodsell, Nucl. Phys. B **830** (2010) 315 [arXiv:0909.0017 [hep-ph]].

[48] S.Y. Choi, M. Drees, A. Freitas and P.M. Zerwas, Phy. Rev. D **78** (2008) 095007 [arXiv:0808.2410 [hep-ph]].

[49] W. Beenakker, R. Höpker, M. Spira and P. M. Zerwas, Nucl. Phys. B **492** (1997) 51 [arXiv:hep-ph/9610490].

[50] S. Dawson, E. Eichten and C. Quigg, Phys. Rev. D **31** (1985) 1581.

[51] J.F. Gunion and H.E. Haber, Nucl. Phys. **B278** (1986) 449.

[52] G. Passarino and M. Veltman, Nucl. Phys. **B160** (1979) 151.

[53] J. Pumplin, D. R. Stump, J. Huston, H. L. Lai, P. M. Nadolsky and W. K. Tung, JHEP **0207** (2002) 012 [arXiv:hep-ph/0201195].

[54] J. A. Aguilar-Saavedra *et al.*, Eur. Phys. J. C **46** (2006) 43 [arXiv:hep-ph/0511344].

[55] S. Y. Choi, H. E. Haber, J. Kalinowski and P. M. Zerwas, Nucl. Phys. B **778** (2007) 85 [arXiv:hep-ph/0612218].

[56] I. Antoniadis, J. R. Ellis and G. K. Leontaris, Phys. Lett. B **399** (1997) 92 [arXiv:hep-ph/9701292]; G. D. Kribs, E. Poppitz and N. Weiner, arXiv:0712.2039 [hep-ph].

[57] G. Belanger, K. Benakli, M. Goodsell, C. Moura and A. Pukhov, JCAP **0908** (2009) 027 [arXiv:0905.1043 [hep-ph]].

[58] I. Antoniadis, K. Benakli, A. Delgado and M. Quiros, Adv. Stud. Theor. Phys. **2** (2008) 645 [arXiv:hep-ph/0610265].

[59] A. Freitas, A. von Manteuffel and P. M. Zerwas, Eur. Phys. J. C **34** (2004) 487 [arXiv:hep-ph/0310182]; Addendum, Eur. Phys. J. C **40** (2005) 435 [arXiv:hep-ph/0408341].

[60] M. M. Muhlleitner and P. M. Zerwas, Acta Phys. Polon. B **37** (2006) 1021 [arXiv:hep-ph/0511339].

[61] D. M. Asner, J. B. Gronberg and J. F. Gunion, Phys. Rev. D **67** (2003) 035009 [arXiv:hep-ph/0110320].

[62] J. Ellis, T. Falk,and K. A. Olive, Phys. Lett. B **444** (1998), 367

[63] R. Iengo, JHEP **0905** (2009) 024, arXiv:0902.0688 [hep-ph].

[64] C. Itzykson and J.–B. Zuber, *Quantum Field Theory*, McGraw–Hill (1985).

[65] See e.g. L.D. Landau and E.M. Lifshitz, *Quantum Mechanics*, Pergamon Press (1977).

[66] S. Cassel, arXiv:0903.5307 [hep-ph].

[67] See e.g. E.W. Kolb and M.S. Turner, *The Early Universe*, Westview Press (1994).

[68] K. Griest and D. Seckel, Phys. Rev. **D43** (1991) 3191.

[69] N. Baro, F. Boudjema, and A. Semenov, Phys. Lett. **B660** (2008) 550, arXiv:0710.1821 [hep-ph].

[70] M. Cirelli, A. Strumia and M. Tamburini, Nucl. Phys. **B787** (2007) 152, arXiv:0706.4071 [hep-ph]; J. March-Russell, S.M. West, D. Cumberbatch and D. Hooper, JHEP **0807** (2008) 058, arXiv:0801.3440 [hep-ph]; N. Arkani-Hamed, D.P. Finkbeiner, T.R. Slatyer and N. Weiner, Phys. Rev. **D79** (2009) 015014, arXiv:0810.0713 [hep-ph]; J. March-Russell and S.M. West, Phys. Lett. **B676** (2009) 133, arXiv:0812.0559 [astro-ph].

[71] J. Zavala, M. Vogelsberger and S.D.M. White, arXiv:0910.5221 [astro-ph.CO].

[72] J. Hisano, K. Kohri and M.M. Nojiri, Phys. Lett. **B505** (2001), 169, hep-ph/0011216; S. Hofmann, D.J. Schwarz and H. Stoecker, Phys. Rev. **D64** (2001) 083507, astro-ph/0104173.

[73] C.P. Burgess, M. Pospelov and T. ter Veldhuis, Nucl. Phys. **B619**, (2001) 709, hep-ph/0011335.

[74] H. Davoudiasl, R. Kitano, T. Li and H. Murayama, Phys. Lett. **B609** (2005) 117, hep-ph/0405097.

[75] E. Ma, Phys. Rev. **D73** (2006) 077301, hep-ph/0601225; R. Barbieri, L.J. Hall and V.S. Rychkov, Phys. Rev. **D74** (2006) 015007, hep-ph/0603188; L. Lopez Honorez, E. Nezri, J.F. Oliver and M.H.G. Tytgat, JCAP **0702** (2007) 028, hep-ph/0612275.

[76] Y.G. Kim, K.Y. Lee and S. Shin, JHEP **0805** (2008) 100 arXiv:0803.2932 [hep-ph].

[77] G. Jungman, M. Kamionkowski and K. Griest, Phys. Rept. **267** (1996) 195, hep-ph/9506380.

[78] J.R. Ellis, T. Falk and K.A. Olive, Phys. Lett. **B444** (1998) 367 (1998), hep-ph/9810360; J.R. Ellis, T. Falk, K.A. Olive and M. Srednicki, Astropart. Phys. **13** (2000) 181, Erratum-ibid. **15** (2001) 413, hep-ph/9905481; M.E. Gomez, G. Lazarides and C. Pallis, Phys. Rev. **D61** (2000) 123512, hep-ph/9907261; C. Boehm, A. Djouadi and M. Drees, Phys. Rev. **D62** (2000) 035012, hep-ph/9911496; J.R. Ellis, K.A. Olive and Y. Santoso, Astropart. Phys. **18** (2003) 395, hep-ph/0112113.

[79] T.R. Slatyer, arXiv:0910.5713 [hep-ph].

[80] J. Edsjö and P. Gondolo, Phys. Rev. **D56** (1997) 1879, hep-ph/9704361.

[81] N. Arkani-Hamed, A. Delgado and G.F. Giudice, Nucl. Phys. **B741** (2006) 108, hep-ph/0601041.

[82] S. Mizuta and M. Yamaguchi, Phys. Lett. B298, 120 (1993).

[83] N. Baro, F. Boudjema, G. Chalons and S. Hao, Phys. Rev. **D81** (2010) 015005, arXiv:0910.3293 [hep-ph].

[84] W. de Boer, C. Sander, V. Zhukov, A. V. Gladyshew, and D. I. Kazakov, Astron. Astrophys. **444**:51 (2005), arXiv:astro-ph/0508617

[85] A. Freitas, Phys. Lett. **B652** (2007) 280, arXiv:0705.4027 [hep-ph]; B. Herrmann and M. Klasen, Phys. Rev. **D76** (2007) 117704, arXiv:0709.0043 [hep-ph]; B. Herrmann, M. Klasen and K. Kovarik, Phys. Rev. **D79**,(2009) 061701, arXiv:0901.0481

[hep-ph]; B. Herrmann, M. Klasen and K. Kovarik, Phys. Rev. **D80** (2009) 085025, arXiv:0907.0030 [hep-ph].

[86] W. Beenakker, S.C. van der Marck and W. Hollik, Nucl. Phys. **B365** (1991) 24.

[87] P. Gondolo, J. Edsjo, P. Ullio, L. Bergström, M. Schelke and E. A. Baltz, JCAP **0407** (2004) 008, arXiv:astro-ph/0406204; P. Gondolo, J. Edsjö, P. Ullio, L. Bergström, M. Schelke, E.A. Baltz, T. Bringmann and G. Duda, http://www.physto.se/ edsjo/darksusy

[88] R. Gaitskell and J. Filippini, http://dmtools.berkeley.edu/limitplots/

[89] J.L. Feng, K.T. Matchev and T. Moroi, Phys. Rev. **D61** (2000) 075005, hep–ph/9909334; J.L. Feng, K.T. Matchev and F. Wilczek, Phys. Lett. **B482** (2000) 388, hep–ph/0004043.

[90] IceCUBE Collab., arXiv:0711.0353 [astro–ph].

[91] J. Edsjo, M. Schelke and P. Ullio, JCAP **0409** (2004) 004, astro–ph/0405414.

[92] J. F. Navarro *et al.*, Mon. Not. Roy. Astron. Soc. **349** (2004) 1039, astro–ph/0311231.

[93] A. Burkert, Astrophys. J. **447** (1995) L25.

[94] J.F. Navarro, C.S. Frenk and S.D.M. White, Astrophys. J. **462** (1996) 563, and Astrophys. J. **490** (1997) 493 .

[95] S. Profumo and P. Ullio, JCAP **0407** (2004) 006, hep–ph/0406018.

[96] PAMELA Collab., O. Adriani et al., Phys. Rev. Lett. **102** (2009) 051101, arXiv:0810.4994 [astro–ph].

[97] H. Baer, A. Belyaev, T. Krupovnickas and J. O'Farrill, JCAP **0408** (2004) 005, hep–ph/0405210.

[98] H. S. Lee *et al.* [KIMS Collaboration], Phys. Rev. Lett. **99** (2007) 091301 [arXiv:0704.0423 [astro-ph]].

[99] R. Bernabei *et al.*, arXiv:1002.1028 [astro-ph.GA].

[100] A. A. Abdo *et al.* [The Fermi LAT Collaboration], Phys. Rev. Lett. **102** (2009) 181101 [arXiv:0905.0025 [astro-ph.HE]].

[101] J. Chang *et al.*, Nature **456** (2008) 362.